8-2016

Particle Transport Phenomena in Non-Newtonian Microfluidics

Xinyu Lu
Clemson University

PARTICLE TRANSPORT PHENOMENA IN NON-NEWTONIAN MICROFLUIDICS

A Dissertation
Presented to
the Graduate School of
Clemson University

In Partial Fulfillment
of the Requirements for the Degree
Doctor of Philosophy
Mechanical Engineering

---

by
Xinyu Lu
August 2016

Accepted by:
Dr. Xiangchun Xuan, Committee Chair
Dr. Donald Beasley
Dr. Richard Figliola
Dr. Chenning Tong

ABSTRACT

In the past two decades, microfluidic devices have become attractive platforms for many chemical and biomedical applications due to their enhanced efficiency and accuracy at a reduced cost. Many of the fluids encountered in these applications exhibit non-Newtonian behaviors. However, the majority of current particle transport studies have been limited in Newtonian fluids only. Very little work has been done on particle transport in non-Newtonian fluids. This dissertation presents experimental and numerical studies of particle transport phenomena in both electric field- and pressure-driven flows in non-Newtonian fluids through microchannels.

In the first part, electrokinetic transport phenomena are investigated in viscoelastic polymer solutions though a constricted microchannel. The first experimental study of particle electrophoresis shows an oscillatory particle motion in the constriction region. This oscillatory motion is affected by the electric field magnitude, particle size and fluid elasticity (i.e., polymer concentration). Then the viscoelastic effect on electrokinetic particle focusing is presented via the study of particle charge effect. The particle focusing trend observed is opposite to that in a Newtonian fluid when the electric field varies. Particle aggregation phenomena are also found at high electric fields. These phenomena are speculated to be a consequence of the fluid viscoelasticity effects. Inspired by the interesting electrokinetic particle transport phenomena, the flow visualization study in the viscoelastic fluid is conducted by using small fluorescent particles as trackers. It is showed that the small particle trajectories, which represent the electroosmotic flow streamlines, are significantly different from those in the Newtonian

fluid at the upstream of the microchannel constriction due to the viscoelastic instability. The 2D numerical result of Oldroyd-B model obtains a smaller flow rate than the Newtonian one, but fails to predict the deflected particle trajectories via Lagrangian particle tracking method.

In the second part, comprehensive studies are performed for particle transport in pressure driven flows through straight rectangular microchannels. A continuous size-based separation is achieved via elasto-inertial pinched flow fractionation (eiPFF). The separation is found to be affected by the flow rate, polymer concentration and channel aspect ratio significantly. Then elasto-inertial particle focusing is studied, which also demonstrates a sheath-free particle separation. An interesting trend has been observed that the particle size (blockage ratio) plays a less significant role on the particle equilibrium position with the increase of channel aspect ratio. Shear-thinning effect is studied in Polyvinylpyrrolidone (PAA) solutions of varied glycerol concentrations in a near-slit channel, which has been demonstrated to inhibit the elastic lift and deflect particles towards the walls. The 2D numerical studies of the particle motion via Oldroyd-B and Giesekus models are qualitatively consistent with our experimental observations of the viscoelastic and shear thinning effects on the elasto-inertial particle focusing. Moreover, shape-based particle separations are demonstrated via both eiPFF and the elasto-inertial lift in sheath-free flows. The rotational motion of non-spherical particles in the viscoelastic fluid is speculated to affect the elasto-inertial lift and lead to different migrations of particles with varied shapes.

DEDICATION

To my best friend and loving wife Wei

ACKNOWLEDGMENTS

First, I would like to thank my advisor Dr. Xiangchun Xuan for investing in my professional growth and providing me with incredible teaching and research opportunities throughout my time at Clemson. I would like to express my sincere gratitude to him for his broad foresight, patient guidance, and unwavering support on my research which paved the way for my academic career.

I would also like to thank my committee members, Dr. Donald Beasley, Dr. Richard Figliola, and Dr. Chenning Tong for giving up their precious time to be a part of my committee. I am gracious for the constant support and constructive advice I have received on their behalf during my graduate studies.

I would like to thank Dr. Shizhi Qian, Dr. Benjamin Mauroy, and Dr. Sang W. Joo for their instruction and advice on the numerical simulation work of this dissertation. I would like to thank my colleagues Saurin Patel, Akshay Kale, John DuBose, Jian Zeng, Junjie Zhu, Yilong Zhou and Di Li for being supportive during the past years. I would like to thank my friends in Clemson for creating a cheerful atmosphere which made my years at the graduate school enjoyable. I would like to thank my father and mother for their love and support throughout my entire life. I am forever indebted to them and much of this work is a reflection of the values they installed in me. Finally, I would like to thank my wife, Wei Xiong, for her patience and support while I pursued my education. I am and will always be indebted to her.

TABLE OF CONTENTS

Page

Table of Contents (Continued)

Page

Table of Contents (Continued)

Page

Table of Contents (Continued)

Page

LIST OF TABLES

LIST OF FIGURES

List of Figures (Continued)

Figure Page

List of Figures (Continued)

Figure Page

List of Figures (Continued)

Figure Page

List of Figures (Continued)

Figure Page

List of Figures (Continued)

Figure Page

List of Figures (Continued)

Figure Page

List of Figures (Continued)

Figure Page

CHAPTER VIII

List of Figures (Continued)

Figure Page

List of Figures (Continued)

Figure Page

NOMENCLATURE

$\mathbf{u}_{EO}$	electroosmotic velocity
ε	relative permittivity
ε_0	vacuum permittivity
$\mathbf{E}$	electric field
$\mu,\ \eta$	fluid dynamic viscosity
ζ	zeta potential
ζ_w	zeta potential of channel wall
ζ_p	zeta potential of particle
$\mathbf{u}_{EP}$	electrophoretic velocity
$\mathbf{u}_{EK}$	electrokinetic velocity
$\mathbf{F}_{DEP}$	dielectrophoretic force
d	particle diameter
r_p	particle radius
f_{CM}	Clausius-Mossotti (CM) factor
σ_p	electric conductivity of particle
σ_f	electric conductivity of solution
$\mathbf{F}_{iL}$	inertial lift force
ρ	fluid density
V_m	maximum fluid velocity
$\mathbf{u}_p$	particle velocity

w	channel width
h	channel height
$\mathbf{N}_1$	first normal stress difference
$\mathbf{N}_2$	second normal stress difference
$\mathbf{F}_{eL}$	elastic lift force
c^*	overlap concentration of polymer solution
M_w	molecular weight
λ_Z	Zimm relaxation time
λ_{eff}, λ_e	effective relaxation time
μ_{EK}	electrokinetic mobility
$\dot{\gamma}$	shear rate
Wi	Weissenberg number
Re	Reynolds number
EL	Elasticity number
Φ	electric potential
$\mathbf{D}$	rate-of-deformation tensor
$\boldsymbol{\tau}$	extra stress tensor
$\mathbf{c}$	conformation tensor
$\mathbf{s}$	log conformation tensor
μ_s	solvent viscosity
μ_p	polymer viscosity
η_0	zero-shear viscosity

D_h	hydraulic diameter
Q	volumetric flow rate
α	flow rate ratio
AR	channel aspect ratio
β	blockage ratio
m_p	mass of particle
I_p	inertia of particle
$\mathrm{T_{orbit}}$	orbit period

CHAPTER ONE

INTRODUCTION

1.1 Aims and motivation

The field of microfluidics has been rapidly developed and widely used for many biomedical, chemical, environmental and food industry applications during last decades.[1,2] Particle (synthetic or biological) transport is one of the most fundamental and significant phenomena in microfluidic devices, including the focusing, trapping, sorting, and separation of particles. As a matter of fact, many of the fluids used in the microfluidic devices are complex, such as polymeric solutions and bodily fluids (e.g., blood, saliva and DNA solutions).[3-5] These solutions usually have molecules with extremely high molecular weights dissolved in the solvent, where the molecular chains can display a tremendous number of configurations and be altered by stretch and distortion.[6] As a consequence, the fluids exhibit strong non-Newtonian behaviors such as shear thinning and viscoelasticity. The shear thinning demonstrates the phenomenon that the fluid viscosity decreases with the increase of shear strain; the viscoelasticity demonstrates that the fluid exhibits both viscous and elastic characteristics when undergoing deformation.

To date, however, particle transport has been little studied in non-Newtonian fluids. In electric field-driven flow, the only experimental studies have been limited to electroosmosis.[7,8] Particle transport phenomenon has never been explored experimentally. In pressure-driven flow, a few particle manipulation studies based on elasto-inertial effect have been reported,[9,10] but a comprehensive understanding of the elasto-inertial particle

focusing and separation is still lacking. There are two significant motivations for studying the particle transport in non-Newtonian fluids. First, it is important and fundamental to understand how the non-Newtonian rheological properties influence the particle motions in microfluidics. Then, the non-Newtonian rheological properties may be able to help us achieve particle manipulation functions that cannot be reached in Newtonian fluids.

Therefore, this dissertation is dedicated to exploring the non-Newtonian rheological effects on particle motion in both electric field- and pressure-driven flows through microchannels. We focus on the fundamentals of experimental behaviors of particle transport in non-Newtonian fluids. Then numerical simulations of different constitutive equations are conducted to support and explain some of the experimental observations. The electrokinetic transport phenomena are studied in a constricted microchannel, where high strains can be introduced near the constriction to generate viscoelasticity. The particle transport in pressure driven flows are studied in straight rectangular microchannels to eliminate other phenomena such as dean flow[11] and lid-driven cavity flow[12]. The non-Newtonian rheological properties of synthetic polymer solutions are stable and well-studied, such as polyethylene oxide (PEO), polyacrylamide (PAA) and Polyvinylpyrrolidone (PVP) solutions. Thus we use them as the flow medium. Our expectations for electric field-driven flow are that the particle motions in non-Newtonian fluids, which have never been reported in previous experiments, are different from those in Newtonian fluids. Our expectations for pressure-driven flow are that the particle lateral motions in non-Newtonian fluids, which have been demonstrated to be different from those in Newtonian fluids, can be affected and manipulated by a variety of

characteristics, such as particle size, particle shape, flow rate, channel geometry, fluid elasticity, and polymer type. And these controllable particle migration behaviors can be used in particle separations. The objective of this dissertation is to obtain a fundamental knowledge of the particle transport phenomena in non-Newtonian microfluidics and to provide a useful guidance for future design of microfluidic devices.

1.2 Background

There are two widely used pumping methods, electric field-driven flow and pressure-driven flow. The electric field-driven flow is easy to control and integrate. Its unique plug-like flow profile provides a uniform particle velocity, which is beneficial for particle manipulation. The pressure-driven flow is the most traditional method. Both flow/pressure control and high throughput can be easily fulfilled. Resulting from the non-uniform velocity of the flow, the inertial hydrodynamic force can be used for particle manipulation. The basic concepts and research backgrounds of both electric field- and pressure-driven flows are introduced in this section.

1.2.1 Electrokinetic Phenomena

When a solid substrate is immerged into an aqueous medium, electric charges (usually negative) develop on the surface spontaneously due to several mechanisms, such as ionization of surface groups and adsorption of ions.[13] In order to neutralize them, the free counter-ions in the solution are attracted to the charged surface and free co-ions are repelled from the charged surface. As a response to the balance between Coulomb force and the thermal Brownian motion, the ions keep their structure of distribution, which is

described as the electric double layer (EDL). The first layer of EDL is the surface charge on the substrate and the second layer is composed of attracted ions on the liquid side, which can be further divided into stern layer of immobilized ions and diffuse layer of free to move ions. The zeta potential, ζ, is defined as the potential at the interface between the Stern layer and the diffuse layer. Typically, the dimension of the EDL is on the order of several nanometers, which is much smaller than that of the microchannel.

Electroosmosis (EO) is the motion of the bulk fluid induced by an applied electric field which drives the migration of excess counter-ions within the EDL. The non-charged liquid molecules are dragged by the moving ions due to viscous effects. Because the EDL is usually much smaller than the channel dimension, the bulk flow outside the EDL has a uniform velocity. Therefore, a plug like bulk flow is formed as shown in Fig. 1. Under the condition of uniform surface charge and fluid properties, low Reynolds number, and zero pressure differences between inlets and outlets, the streamlines in electrokinetic flows are equivalent to the electric field lines due to the similarity between electroosmotic flow and electric fields.[14] With the condition that the EDL is much smaller than the channel width, the bulk fluid velocity can be describe by the Smoluchowski slip velocity,

$$\mathbf{u}_{EO} = -\varepsilon\varepsilon_0\zeta_w\mathbf{E}/\mu \qquad (1)$$

where ε and ε_0 are the relative and vacuum permittivity, ζ_w is the zeta potential of the channel wall, μ is the fluid dynamic viscosity, and $\mathbf{E}$ is the electric field.

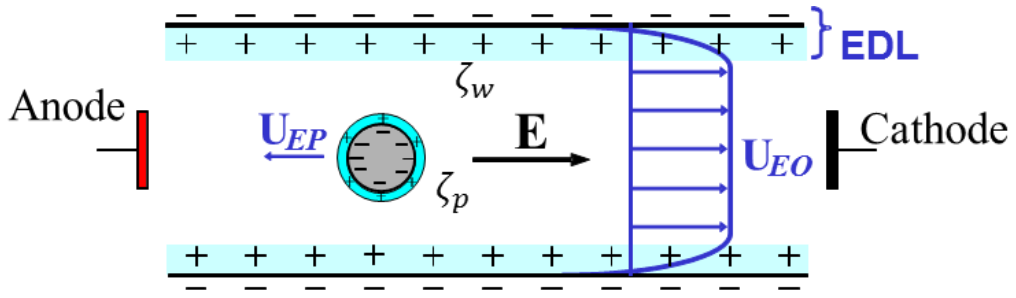

Fig. 1.1. Electroosmosis and Electrophoresis in a straight channel under a DC electric field.

Electrophoresis (EP) is the motion of a non-zero charged particle initiated by an applied electric field in an aqueous medium. Similar to the channel walls, EDL is also generated around particles. With the electrostatic surface charge, zeta potential of particle ζ_p, the electrophoretic velocity is given by

$$\mathbf{u}_{EP} = \varepsilon\varepsilon_0\zeta_p\mathbf{E}/\mu \tag{2}$$

As Fig. 1 shows, the EO and EP usually have opposite directions due to the same sign of zeta potentials of the wall and particle, respectively. When subjected to a uniform electric field, the particle motion is a combination of EO and EP, which is called electrokinetic motion and defined as

$$\mathbf{u}_{EK} = \varepsilon\varepsilon_0(\zeta_p - \zeta_w)\mathbf{E}/\mu \tag{3}$$

Dielectrophoresis (DEP) is the motion of a polarizable particle in a polarizable electrolyte solution under a non-uniform electric field, where the particle motion is able to cross fluid streamlines. The direction of the DEP force is determined by the relative magnitude of the particle and medium polarizabilities. When the particle is less polarizable than the medium, the translation of the particle is towards the low electric

field region which is called negative DEP. When the particle is more polarizable than the medium, the translation of the particle is towards the high electric field region, which is called positive DEP. The DEP force induced on a spherical particle in a DC electric field is given by[15]

$$\mathbf{F}_{DEP} = (1/2)\pi\varepsilon\varepsilon_0 d^3 f_{CM}\,(\mathbf{E}\cdot\boldsymbol{\nabla}\mathbf{E}) \tag{4}$$

where d is the particle diameter and f_{CM} is the Clausius-Mossotti (CM) factor. In DC or low-frequency AC (<100 kHz) fields, the CM factor can be calculated by

$$f_{CM} = \frac{\sigma_p - \sigma_f}{\sigma_p + 2\sigma_f} \tag{5}$$

where σ_p and σ_f are the electric conductivities of the particle and solution, respectively. Because the Reynolds number is typically small in electrokinetic flows, the DEP velocity is calculated by balancing the DEP force with Stokes' drag,

$$\mathbf{U}_{DEP} = \frac{\varepsilon\varepsilon_0 d^2 f_{CM}}{6\mu}\,(\mathbf{E}\cdot\boldsymbol{\nabla}\mathbf{E}) \tag{6}$$

A variety of electrokinetic particle manipulation studies have been reported in Newtonian fluids. The electrophoretic separation technique has been demonstrated by the mobility differences of different samples.[16-19] But the long analysis time is always the major concern of the batch-wised method. In contrast, the dielectrophoretic technique has become a powerful tool for particle focusing and separation because it is a continuous method and is less time consuming. Traditionally, the electric field gradient, which is the source of DEP, is created by imbedded electrodes.[20-23] The electrode-based DEP (eDEP) technique can reorient the particles near the electrode according to the magnitude and frequency of the applied AC electric field and achieve focusing or separation functions.

However, the fabrication complexity is one of its main disadvantages. An alternative method to initiate the electric field gradient is through the insulating channel geometries, which is called insulator-based DEP (iDEP). Particle manipulations can be achieved in different channel geometries, such as converging-diverging channels,[24] curve channels,[25,26] and channels with hurdles[27] and posts[28]. As compared with eDEP, iDEP is able to pump the solution and manipulate the suspended particles under a DC electric field simultaneously. However, no experimental studies have been reported on electrokinetic particle motion in non-Newtonian fluids.

1.2.2 Particle motion in pressure driven flow

Because of the small dimensions of microchannels, the majority of flows in microfluidic devices can be considered as laminar flows. The hydrodynamic forces of particles in laminar flow can be classified as two groups, drag and lift forces. The drag force acts on the particle opposite to the relative motion with respect to a surrounding fluid, which affects the translation of the particle in both electric field- and pressure-driven flows. The lift force acts on the particle perpendicular to the flow direction, leading to a cross-streamline migration. The inertial particle migration was firstly experimentally demonstrated by Segre and Silberberg[29] for particles flowing through circular pipes. As a result from the inertial effect, the lifts on particle migration in general can be described as two different types of forces, i.e., wall lift and shear gradient lift forces.[30] Fig. 2 (a) depicts the lift forces experienced by a particle in the half cross-section of a straight channel. The background color indicates the shear rate distribution

(the redder color indicating the higher magnitude), which is calculated by a 3D numerical model in COMSOL. When the particle is close to a channel wall, the wall lift pushes the particles away from the wall. The magnitude of this lift force decreases with the growing distance between the particle and channel wall. The shear gradient lift force drives particles towards high shear rate regions, i.e., the channel walls. Taken together, the inertial lift $\mathbf{F}_{iL}$ for near-wall particles has been demonstrated to follow[31]

$$\mathbf{F}_{iL} \sim \rho V_m^2 d^6 / w^4 \tag{7}$$

where V_m is the maximum fluid velocity and w is the channel width. Particles tend to migrate to several equilibrium positions as a result of the balance of the two lift components. The inertial lift force has been used for particle manipulation, such as focusing,[32,33] ordering,[34,35] and separation[36-38].

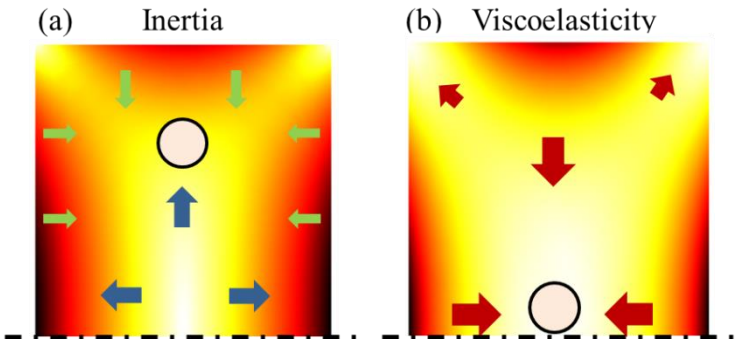

Fig. 1.2. Schematic illustration of the inertial lift forces (a) and viscoelastic lift force (b) in the half cross-section of a straight channel. In the inertial case, the background color indicates the shear rate distribution (the redder color indicating the higher magnitude). The green arrows indicate the wall lift force, and the blue arrows indicate the shear gradient lift force. In the viscoelastic case, the background color indicates the first normal stress difference distribution (the redder indicating the higher magnitude), and the red arrows represent the viscoelastic lift force.

In non-Newtonian fluids, the viscoelastic and shear thinning effects also contribute to the particle migration. For viscoelastic fluid, the particle migration results from the non-uniform normal stress differences.[39] In a straight rectangular channel, $\boldsymbol{\tau}_{11}$, $\boldsymbol{\tau}_{22}$, and $\boldsymbol{\tau}_{33}$ are the normal stresses in the translational direction, velocity gradient direction and rotational direction respectively. The first normal stress difference $\mathbf{N}_1$ is defined as $\boldsymbol{\tau}_{11}$ - $\boldsymbol{\tau}_{22}$ and the second normal stress difference $\mathbf{N}_2$ is defined as $\boldsymbol{\tau}_{22} - \boldsymbol{\tau}_{33}$. Generally $\mathbf{N}_1$ is much larger than $\mathbf{N}_2$ in viscoelastic fluids with a constant shear viscosity.[40] In Fig. 2 (b), the distribution of $\mathbf{N}_1$ is calculated based on a widely used non-Newtonian constitutive model, Oldroyd-B model, by COMSOL. The elastic lift force $\mathbf{F}_{eL}$ is given by,[41,42]

$$\mathbf{F}_{eL} \sim d^3 \nabla \mathbf{N}_1 \tag{8}$$

which drives the particle towards low first normal stress difference regions, i.e., the channel corner and the center regions. In contrast, the shear thinning effect is found to suppress the viscoelastic lift and push particles away from the center region.[43]

A very small number of works have paid attention to the viscoelastic particle transport phenomena. Particle focusing was achieved by the combined viscoelastic and inertial effects, which eliminate the viscoelastic equilibrium positions at corners.[44,45] Particle separations were demonstrated in very few recent studies. Yang et al.[9] successfully separated fresh red blood cells from rigid ones and particles in viscoelastic fluid based on deformability. Nam et al.[10] and Kang et al.[44] showed size-based particle separations from a sheath flow-focused particle mixture solution near the walls. But a

comprehensive understanding of the viscoelastic particle focusing and separation in straight rectangular channels is still lacking.

1.3 Overview of dissertation

This dissertation consists of nine chapters and is organized as follows. The first chapter is an introduction. The next three chapters focus on the electric field-driven particle and fluid motions. Chapter 2 presents the experimental work of an unexpected particle oscillation in viscoelastic fluids through a microchannel constriction for particles that move along with the fluid flow. Several parameters are tested in the experiment to further explore this oscillatory motion, such as the electric field magnitude, particle size and fluid elasticity. Then the particle charge effect is studied for particles that move against the fluid flow in Chapter 3, in which different transport phenomena are expected between Newtonian and non-Newtonian fluids. For a better understanding of the electrokinetic particle transport in viscoelastic fluids, Chapter 4 studies the viscoelastic effect on electroosmosis experimentally and numerically in the constricted channel by tracking small fluorescent particles. The flow field may be affected by the viscoelastic effect, which may contribute to the significantly different particle motions between Newtonian and non-Newtonian fluids as stated in the preceding two chapters. The following four chapters study the particle transport in pressure driven flows. The particle size effect is first studied in Chapter 5 by focusing all particles via sheath flow to let them start from the same lateral position. A continuous size-based separation is achieved that we call elasto-inertial pinched flow fractionation (eiPFF). This separation is found to be

affected by the flow rate, polymer concentration and channel aspect ratio significantly. Inspired by them, it is more intriguing to study the lateral motions of particles that are initially distributed everywhere in the cross-section. And in turn it is also favorable to understand the mechanism of the eiPFF. Thus, Chapter 6 presents the experimental and numerical explorations of the elasto-inertial effect on particle equilibrium positions and focusing in the sheath-free flow through rectangular microchannels. The predictions with the Oldroyd-B and Giesekus models are compared qualitatively with the experimental observations of the viscoelastic and shear thinning effects on particle motion in slit-like microchannels. Moreover, another important characteristic, particle shape, also draws our interests and is studied in the experiments of the following two chapters. The elasto-inertial focusing is found to be a strong function of particle shape due to perhaps the rotational motion of non-spherical particles in viscoelastic fluids. Chapter 7 presents the shape-based separation via the eiPFF technique. In a more general condition without sheath flow, Chapter 8 demonstrates the sheath-free shape-based separation of in viscoelastic fluids. In chapter 9, we summarize the key contributions of this dissertation and propose the future work.

As the studies in chapters 2, 3, 5, 7, and 8 have all been published, the exact copies of the journal articles are used in this dissertation. Those in chapters 4 and 6 are also written in the format of journal publications and will be submitted for review in the near future.

References

[1] P. S. Dittrich, A. Manz, Nature Reviews Drug Discovery **5**(3), 210-8 (2006).

[2] H. A. Stone, A. D. Stroock, A. Ajdari, Annu Rev Fluid Mech **36**, 381-411 (2004).

[3] C. J. Pipe, G. H. McKinley, Mech. Res. Commun. **36**, 110−120 (2009).

[4] C. L. Berli, Electrophoresis **34**, 622−630 (2013).

[5] C. Zhao, C. Yang, Adv. Colloid Interface Sci. **201**, 94−108 (2013).

[6] R. B. Bird, R. C. Armstrong, O. Hassager, Dynamics of Polymeric liquids, vol.1 (1977).

[7] R. M. Bryce and M. R. Freeman, Phys. Rev. E **81**, 036328 (2010).

[8] R. M. Bryce and M. R. Freeman, Lab Chip **10**, 1436-1441 (2010).

[9] S. Yang, S. S. Lee, S. W. Ahn, K. Kang, W. Shim, G. Lee, K. Hyune, J. M. Kim, Soft Matter **8**, 5011−5019 (2012).

[10] J. Nam, H. Lim, D. Kim, H. Jung, S. Shin, Lab Chip **12**, 1347−1354 (2012).

[11] D.J. Lee, H. Brenner, J.R. Youn, and Y.S. Song, Scientific reports **3** (2013).

[12] P. Pakdel and G. H. McKinley, Physics of Fluids (1994-present), **10**(5), 1058-1070 (1998).

[13] R. J. Hunter, Zeta potential in colloid science: principles and applications, Academic Press London, vol. 125, (1981).

[14] J. G. Santiago, Analytical Chemistry **73**(10), 2353-2365 (2001).

[15] H. Morgan, N. G. Green, AC electrokinetic: colloids and nanoparticles, Research Studies Press (2002).

[16] D. J. Harrison, K. Fluri, K. Seiler, Z. Fan, C. S. Effenhauser, and A. Manz, SCIENCE-NEW YORK THEN WASHINGTON- **261**, 895-895 (1993).

[17] A. T. Woolley and R. A. Mathies, Analytical chemistry **67**(20), 3676-3680 (1995).

[18] D. E. Raymond, A. Manz and H. M. Widmer, Analytical Chemistry **66**(18), 2858-2865 (1994).

[19] L. Kremser, D. Blaas and E. Kenndler, Electrophoresis **25**(14), 2282–91 (2004).

[20] P. R. Gascoyne and J. Vykoukal, Electrophoresis **23**, 1973–83 (2002).

[21] V. H. Perez-Gonzalez , V. Ho, L. Kulinsky, M. Madou and S. O. Martinez-Chapa, Lab Chip **13**, 4642–52 (2013).

[22] R. Pethig, Biomicrofluidics **4**, 022811 (2010).

[23] Z. R. Gagnon, Electrophoresis **32**, 2466–87 (2011).

[24] J. Zhu, X. Xuan, Electrophoresis **30**, 2668-2675 (2009).

[25] J. DuBose, J. Zhu, S. Patel, X. Lu, N. Tupper, J. M. Stonaker, and X. Xuan, Journal of Micromechanics and Microengineering **24**, 115018 (2014).

[26] J. DuBose, X. Lu, S. Patel, S. Qian, S. Joo, X. Xuan, Biomicrofluidics **8**, 014101 (2014).

[27] B. G. Hawkins, A. E. Smith, Y. A. Syed and B. J. Kirby, Anal. Chem. **79**, 7291–300 (2007).

[28] R. C. Gallo-Villanueva, N. M. Jesús-Pérez, J. I. Martínez-López, A. Pacheco and B. H. Lapizco-Encinas, Microfluid. Nanofluid. **10**, 1305–15 (2011).

[29] G. Segre and A. Silberberg, J. Fluid Mech. 14 (1962).

[30] J. P. Matas, J. F. Morris, and E. Guazzelli, Oil & gas science and technology **59**(1), 59-70 (2004).

[31] D. D. Carlo, J. F. Edd, K. J. Humphry, H. A. Stone, and M.Toner, Phys. Rev. Lett. **102**, 094503, (2009).

[32] B. Chun and A. J. C. Ladd, Physics of Fluids (1994-present) **18**(3), 031704 (2006).

[33] J. Zhou and I. Papautsky, Lab on a Chip **13**(6), 1121-1132 (2013).

[34] S. C. Hur, H. T. K. Tse, and D. Di Carlo, Lab on a Chip **10**(3), 274-280 (2010).

[35] D. D. Carlo, D. Irimia, R. G. Tompkins, and M. Toner, Proceedings of the National Academy of Sciences **104**(48), 18892-18897 (2007).

[36] J. Hansson, J. M. Karlsson, T. Haraldsson, H. Brismar, W. van der Wijngaart, and A. Russom, Lab on a Chip, **12**(22), 4644-4650 (2012).

[37] J. Zhou, P.V. Giridhar, S. Kasper, and I. Papautsky, Lab on a Chip **13**(10), 1919-1929 (2013).

[38] X. Lu and X. Xuan, Analytical chemistry **87**(8), 4560-4565 (2015).

[39] B. P. Ho and L. G. Leal, Journal of Fluid Mechanics **76**(4), 783-799 (1976).

[40] J. A. Pathak, D. Ross, and K. B. Migler, Physics of Fluids (1994-present) **16**(11), 4028-4034 (2004).

[41] M. A. Tehrani, Journal of Rheology (1978-present) **40**(6), 1057-77 (1996).

[42] S. Yang, J. Y. Kim, S. J. Lee, S. S. Lee, and J. M. Kim, Lab on a Chip **11**(2), 266-273 (2011).

[43] G. Li, G. H. McKinley, and A. M. Ardekani, Journal of Fluid Mechanics **785**,486-505 (2015).

[44] K. Kang, S.S. Lee, K. Hyun, S.J. Lee, and J.M. Kim, Nature communications, 4 (2013).

[45] E. J. Lim, T. J. Ober, J. F. Edd, S. P. Desai, D. Neal, K. W. Bong, P. S. Doyle, G. H. McKinley, and M. Toner, Nature communications **5** (2014).

CHAPTER TWO

AN UNEXPECTED PARTICLE OSCILLATION FOR ELECTROPHORESIS IN VISCOELASTIC FLUIDS THROUGH A MICROCHANNEL CONSTRICTION

Abstract

Electrophoresis plays an important role in many applications, which, however, has so far been extensively studied in Newtonian fluids only. This work presents the first experimental investigation of particle electrophoresis in viscoelastic polyethylene oxide (PEO) solutions through a microchannel constriction under pure DC electric fields. An oscillatory particle motion is observed in the constriction region, which is distinctly different from the particle behavior in a polymer-free Newtonian fluid. This stream-wise particle oscillation continues until a sufficient number of particles form a chain to pass through the constriction completely. It is speculated that such an unexpected particle oscillating phenomenon is a consequence of the competition between electrokinetic force and viscoelastic force induced in the constriction. The electric field magnitude, particle size, and PEO concentration are all found to positively affect this viscoelasticity-related particle oscillation due to their respective influences on the two forces.

2.1 Introduction

Electrophoresis plays an important role in many applications such as capillary electrophoresis and electrokinetic micro/nanofluidics etc.[1] It is the motion of a charged particle with respect to a suspending fluid under the application of an electric field. The fluid can be either infinite for which particle electrophoresis resembles particle

sedimentation in a stationary fluid, or confined in a channel where particle electrophoresis is almost always accompanied by fluid electroosmosis.[2] While particle electrophoresis in both cases has been extensively investigated in the past, the majority of these studies concern only Newtonian fluids.[3] Due to the shear-rate-independent viscosity of these fluids, electrophoresis and electroosmosis are both a linear function of the applied electric field and the surface charge (or zeta potential) of the particle/channel.[4] However, many of the fluids used in capillary electrophoresis and microfluidic devices are polymer solutions[5-8] and biofluids[9-12] which are complex. They often possess a shear-rate-dependent viscosity and may even exhibit elastic or plastic effects.[13-16] Consequently, electrophoresis in and electroosmosis of these non-Newtonian fluids could be significantly different from those with Newtonian fluids.[17-19]

A number of theoretical (including numerical) studies have been recently reported on electroosmosis of non-Newtonian fluids whose rheology is characterized by various constitutive equations, including the power-law,[20-30] Phan-Thien-Tanner (PTT),[31-36] Carreau,[37-39] Oldroyd-B (including Upper-Convected Maxwell, UCM[34])[40] models and others.[41-43] Nonlinear relations are obtained for the electroosmotic velocity as a function of the electric field and zeta potential. Also, the electrophoretic motion of particles in non-Newtonian fluids has been numerically predicted by Hsu and co-workers with a Carreau model.[44-51] The fluid shear-thinning effect is found to increase the particle mobility significantly as compared to that in a Newtonian fluid. Recently, Khair et al.[52] presented a theoretical scheme to calculate the electrophoretic motion of particles of any shape in fluids with a shear-rate-dependent viscosity. They demonstrated a shape and size

dependence of particle electrophoresis due to the non-Newtonian rheology, which is markedly different from that in Newtonian fluids.[53]

To date, however, very little experimental work has been done on electroosmosis of and electrophoresis in non-Newtonian fluids. Chang and Tsao[54] observed a significant drag reduction in electroosmotic flow of polymer solutions, which increases with the ratio of the polymer size to the electric double layer thickness. Bryce and Freeman[55] demonstrated that the flow velocity of standard electroosmotic pumping is sufficient to excite extensional instabilities in dilute polymer solutions through a 2:1 microchannel constriction. Interestingly, they found later that these instabilities actually reduce the fluid mixing relative to that in polymer-free fluids.[56] Inspired by the work from Bryce and Freeman,[55,56] we conducted an experimental study of particle electrophoresis in viscoelastic polymer solutions through a microchannel constriction. An unexpected particle oscillation was observed, which was found to vary with the applied electric field, particle size, and polymer concentration. This article presents these experimental results along with our attempted explanation of the particle oscillating phenomenon.

2.2 Experiment

2.2.1 Preparation of non-Newtonian fluids and particle suspensions

Non-Newtonian fluids were prepared by dissolving Poly(ethylene oxide) (PEO) powder (average molecular weight is 4×10^6 Da, Sigma-Aldrich USA) into 1 mM phosphate buffer. Four concentrations of PEO were used in our experiment, 50 ppm (i.e., dissolving 50 mg of PEO powder into 1 litre of buffer), 100 ppm, 200 ppm, 500 ppm,

which are all lower than its overlap concentration, c^* = 547 ppm, as calculated from the expression of Graessley.[57] The last quantity was obtained from $c^* = 0.77/[\eta]$, where $[\eta] = 0.072M_w^{0.65}$ is the intrinsic viscosity given by the Mark-Houwink relation with $M_w = 4\times10^6$ g/mol being the molecular weight of PEO.[80] The shear viscosities of the four prepared PEO solutions (with no particles or surfactants being added) were measured in a Couette geometry by a rheometer (ARES LS/M, TA instruments) and found to be 1.1 mPa·s, 1.2 mPa·s, 1.4 mPa·s and 2.0 mPa·s, respectively, with a negligible variation over the range of shear rate from 50 s^{-1} to 1,000 s^{-1}. Therefore, each of these PEO solutions can be viewed as a Boger fluid,[58] which has viscoelasticity but negligible shear-thinning/thickening effects. This treatment is consistent with that in the recent work from Rodd et al.[59] The relaxation time of the PEO polymer was calculated to be λ_Z = 1.07 ms according to Zimm theory.[60] The effective relaxation time[61] of the PEO solutions was estimated using $\lambda_{eff} = 18\lambda_Z (c/c^*)$, which gives 4.07 ms, 6.39 ms, 10.01 ms, and 18.17 ms, for the prepared four concentrations. The pure buffer with no addition of the PEO polymer was used as the Newtonian fluid in our experiments for comparison. A summary of these solution properties is given in Table 1.

Table 1. Solution properties

Fluid property (at 20 °C)	Pure buffer	PEO in pure buffer (concentration c)			
		50 ppm	100 ppm	200 ppm	500 ppm
Density (g/cm^3)	0.998	0.998	0.998	0.998	0.998
Zero-shear viscosity (mPa·s)	1.0	1.1	1.2	1.4	2.0
Overlap concentration c^* (ppm)		547	547	547	547
Concentration ratio c/c^*		0.091	0.183	0.366	0.914
Zimm relaxation time, λ_Z (ms)		1.07	1.07	1.07	1.07
Effective relaxation time, λ_{eff} (ms)		4.07	6.39	10.01	18.17

The particle suspensions were prepared by re-suspending polystyrene spheres of 3 μm, 5 μm, and 10 μm in diameter (Sigma-Aldrich USA), respectively, into the PEO solution(s) at a final concentration of 10^6–10^7 particles per milliliter. A small amount of Tween 20 (0.5% in volume ratio, Fisher Scientific) was added to the suspensions for the purpose of suppressing the particle adhesions to microchannel walls and other particles. For comparison, 10 μm particles were also re-suspended in the pure buffer with Tween 20 being added. Polystyrene particles have a density of 1.05 g/cm^3, which is slightly larger than that of the suspending media. They are non-conducting in bulk, but exhibit surface conductance due to the spontaneous occurrence of electric double layer.[1,2] Their "effective" electric conductivity was estimated to be much smaller than that of the PEO solution (about 200 μS/cm) for all sizes of particles used in our experiments. Hence, they all experience negative dielectrophoresis under the gradients of DC electric fields.[3,4]

2.2.2 Microchannel fabrication

The microchannel was fabricated by the standard soft lithography technique using liquid polydimethylsiloxane (PDMS). Briefly, a negative photo mask was made by printing the channel layout, which was drawn in AutoCAD®, onto a transparent thin film at a resolution of 10,000 dpi (CAD/Art Services). A 40-μm thick SU-8-25 photoresist (MicroChem) was coated onto a clean glass slide using a spin coater (WS-400B-6npp/lite, Laurell Technologies), which started at 500 rpm for 10 s and ramped by 300 rpm/s to the terminal spin speed of 1000 rpm with a dwelling of 20 s. After a two-step soft bake (65 °C for 4 min and 95 °C for 8 min) in a hot plate (HP30A, Torrey Pines

Scientific), the photoresist film was exposed through the photo mask to a 365 nm UV light (ABM Inc., San Jose, CA) for 30 seconds. It then underwent a two-step hard bake (65 °C for 2 min and 95 °C for 4 min) before being submerged into a SU-8 developer solution (MicroChem) for 10 min. Following a brief rinse with isopropyl alcohol (Fisher Scientific) and another two-step hard bake (65 °C for 1 min and 95 °C for 5 min), a positive replica of photoresist was left on the glass slide, which served as the mold of the microchannel (i.e., the so-called master) for reuses.

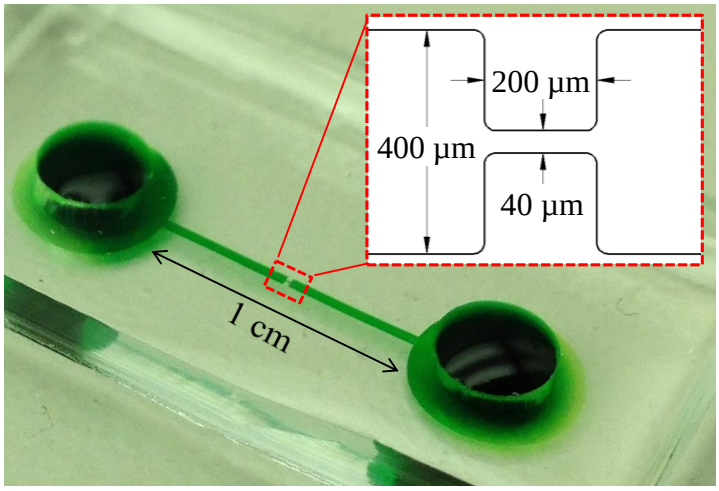

FIG. 1. Picture of the 10:1:10 contraction-expansion microchannel (filled with green food dye for clarity) used in experiments. The inset indicates the dimensions of the constriction.

The microchannel mold was placed in a Petri dish and then covered by liquid PDMS, a mixture of Sylgard 184 and the curing agent at a 10:1 ratio in weight. After degassing in a vacuum oven (13-262-280A, Fisher Scientific) for 15 minutes, the Petri dish was placed into a gravity convection oven (13-246-506GA, Fisher Scientific) at 70 °C for 3-4 hours. The cured PDMS that enclosed the entire microchannel was cut using a scalpel and peeled off from the master. Two through holes of 5 mm in diameter each

were made as reservoirs in the pre-defined circles at microchannel ends using a metal punch. Immediately following a plasma treating for 1 min (PDC-32G, Harrick Scientific), the channel side of the PDMS slab was irreversibly bonded to a clean glass slide. A drop of the working solution (with no particles suspended) was loaded into one of the reservoirs, which was found to fill the entire microchannel automatically by capillary force and used to maintain the channel walls hydrophilic. A picture of the fabricated PDMS/glass microchannel is shown in FIG. 1. It is 400 μm wide and 1 cm long with a uniform depth of 40 μm. It has a 40 μm wide constriction in the middle with a length of 200 μm.

2.2.3 Experimental technique

The electrokinetic motion of particles in the microchannel was induced by applying a DC electric field across the channel, which was supplied by a function generator (33220A, Agilent Technologies) in conjunction with a high-voltage amplifier (609E-6, Trek). The electric field was kept no more than 500 V/cm in order to minimize Joule heating effects.[62,63] The pressure-driven motion of particles was eliminated by balancing the liquid heights in the end reservoirs prior to each test. Particle motions were visualized through an inverted microscope (Nikon Eclipse TE2000U, Nikon Instruments) with a CCD camera (Nikon DS-Qi1Mc) at a rate of 15 frames per second. The obtained digital images were post-processed using the Nikon imaging software (NIS-Elements AR 2.30). Particle velocity was determined through dividing the particle travelling distance by the corresponding time interval. The error in reading the pixel number of the particle

center was around 1 μm, and the error in the measured particle velocity was estimated to be around 30 μm/s. Particle streak images were obtained by superimposing a sequence of around 150 images.

2.3 Results and discussion

2.3.1 Comparison of particle electrophoresis in Newtonian and non-Newtonian fluids

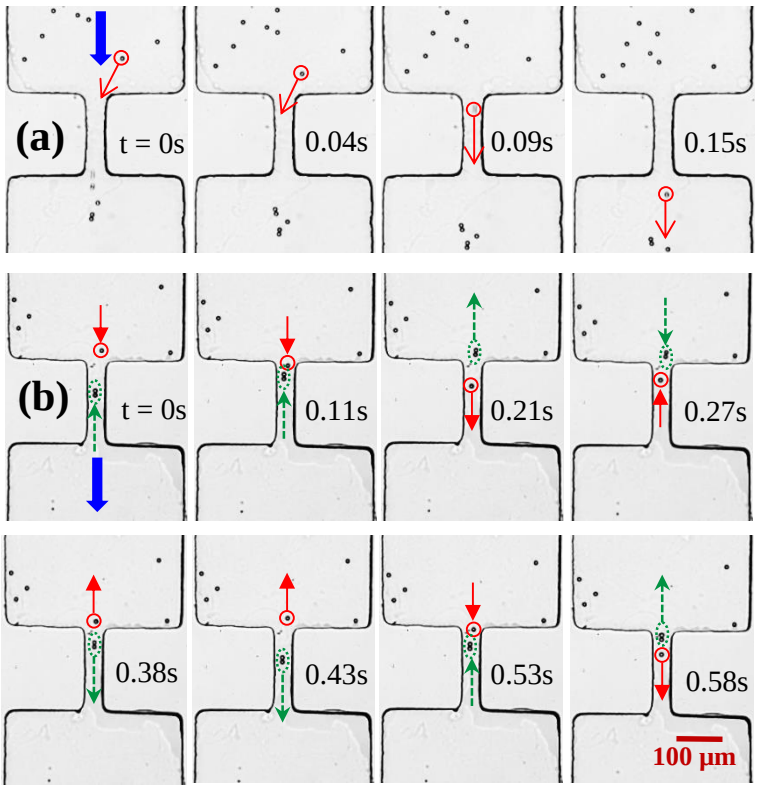

FIG. 2. Sequential images demonstrating the difference of 10 μm particle electrophoresis in (a) (enhanced) Newtonian (1mM buffer) and (b) (enhanced) non-Newtonian (500 ppm PEO in 1 mM buffer) fluids through the microchannel constriction under an average DC electric field of 200 V/cm. The particles under track are highlighted by a circle (for singles) or an ellipse (for doubles) for a better illustration, where the thin arrows indicate the particle moving directions at the time instants labeled on the images. The block arrows indicate the overall moving directions of the fluids and particles in the channel.

FIG. 2 compares the electrophoretic motions of single 10 μm-diameter particles in (a) Newtonian (1 mM buffer) and (b) non-Newtonian (500 ppm PEO in 1 mM buffer) fluids through the microchannel constriction. The average DC electric field across the channel length is 200 V/cm, and particles move from top to bottom in all images for both cases. The suspending fluid also moves from top to bottom in each case, indicating that the channel wall has a higher zeta potential (negative value) than the particle. In the Newtonian fluid, the tracked particle (highlighted by a circle) passes through the constriction quickly as seen from the sequence of images in FIG. 2(a) (enhanced). In contrast, the highlighted single particle in the PEO solution can reach only a half way through the constriction, before it is bounced back toward the entrance of the constriction as demonstrated by the sequential images in FIG. 2(b) (enhanced). Interestingly, this reversing particle overshoots the constriction entrance and then re-enters the constriction to start an oscillation. Moreover, this oscillatory motion seems to be three-dimensional because the particle appears clear and blurred (i.e., in and out of the focal plane) periodically. Since the same amount of Tween 20 was added to both the pure buffer and the PEO solution, we believe the observed difference in particle electrophoresis through the constriction results entirely from the PEO polymer. We have also conducted a quick test of particle electrophoresis in a buffer/glycerol solution and found no oscillating particles in the constriction. Therefore, the increase in solution viscosity alone cannot produce the observed anomalous particle motion.

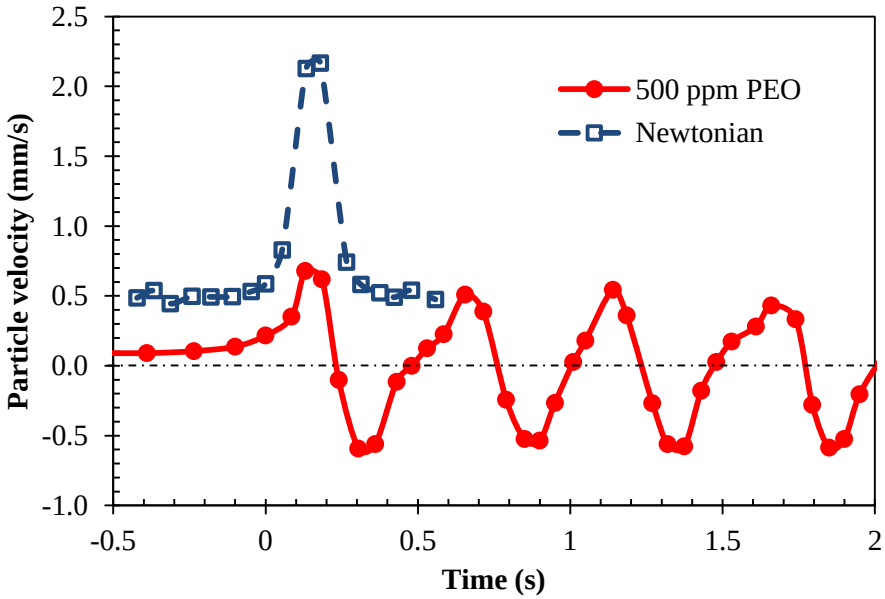

FIG. 3. Comparison of the transient axial velocities of the single particles tracked in the Newtonian and non-Newtonian fluids (see FIG. 2) through the microchannel constriction. Note that the times greater than 0 s correspond to those labeled in FIG. 2 for each fluid. The dashed-dotted line indicates a zero particle velocity.

These distinguished particle electrophoresis behaviors in the two types of suspending fluids can be better identified in FIG. 3, where the transient axial velocities of the two tracked particles in FIG. 2 are compared against time. The time instants greater than 0 s correspond exactly to those labeled on the images of FIG. 2. The time instants smaller than 0 s are included to compare the particle velocities in the two fluids distant from the constriction. The particle in the Newtonian fluid moves at an axial velocity of about 490 μm/s before approaching the constriction, which is more than 5 times larger than that of 85 μm/s for the particle in the non-Newtonian fluid. The Reynolds number based on the particle velocity was thus estimated to be around 0.04 and 3.4×10^{-3} in these two fluids. In the constriction region, the particle in the Newtonian fluid experiences an

apparent acceleration followed by a nearly symmetric deceleration, which is consistent with our earlier study.[64] In contrast, the particle in the non-Newtonian fluid undergoes an oscillation with an approximate period of 0.5 s and a maximum speed of about 550 μm/s in both the forward and the backward directions. Using this particle velocity, V_p, we estimated the Weissenberg number ($De = 2\lambda_{eff}V_p/w$ with λ_{eff} and w being the effective relaxation time, see Table 1, and constriction width, respectively) or equivalently the Deborah number inside the constriction to be around 0.5.

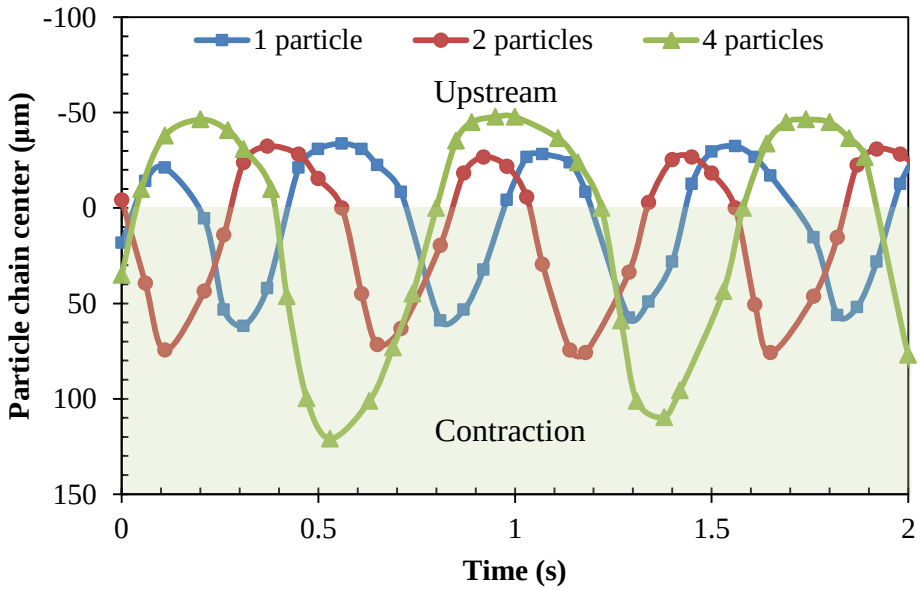

FIG. 4. Tracked center position vs. time for oscillating 10 μm particle chains with various lengths (i.e., the number of particles in the chain) in 500 ppm PEO solution through the microchannel constriction. The average DC electric field is 200 V/cm across the channel length. The shaded zone represents the span of the constriction from 0 to 200 μm.

Single particles in the PEO solution oscillate in the microchannel constriction and are unable to pass through. They can easily get attached to each other forming a particle chain; for example, FIG. 2(b) shows an oscillating two-particle chain (highlighted by a

dashed ellipse) in the constriction. The particle chain still oscillates inside the constriction until its length (i.e., the number of particles in the chain) exceeds a certain threshold value. This threshold appears to be a function of electric field and particle size etc., which will be revisited in the parametric study below (see Section C). The oscillating patterns of particle chains with various lengths are demonstrated in FIG. 4 in the form of their center position vs. time. The oscillating amplitude increases with the number of particles in the chain, and so longer chains tend to move through the constriction with a larger probability. We observed that 10 μm particles can escape from the constriction when a chain of more than 3 particles is formed in 500 ppm PEO solution under the 200 V/cm DC electric field. In addition, the oscillating frequency is found to decrease when the length of the particle chain increases.

2.3.2 Attempted explanation of the observed particle oscillation in the non-Newtonian fluid

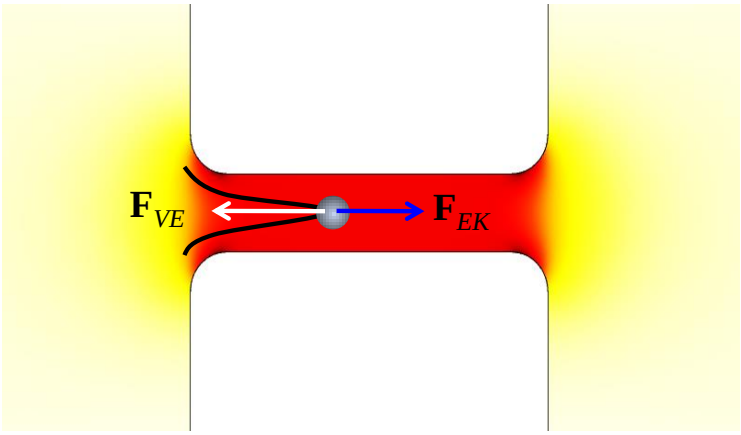

FIG. 5. Schematic illustration of the speculated mechanism for particle oscillation in electrophoresis through a microchannel constriction with a viscoelastic fluid. The background color indicates the electric field contour (the darker the larger magnitude).

Anomalous particle motion has been reported in particle sedimentation or rise (e.g., drops and bubbles that are lighter than the fluid) through still viscoelastic fluids,[65-68] which is attributed to either the evolution of a negative wake downstream of the particle,[69-73] or the formation and breakup of flow-induced structures due to the stress-induced instability.[74-78] The precise mechanism for the particle oscillating phenomenon observed in the PEO solution through the microchannel constriction is currently unknown and deserves intensive future investigations. We speculate that it may be explained using the competition of two forces present in the constriction region as schematically shown in FIG. 5. One is the driving force for the observed electrokinetic particle motion in the microchannel, $\mathbf{F}_{EK}$, which is a combination of fluid electroosmosis, particle electrophoresis and dielectrophoresis, and varies with position in the constriction region.[64] Note that the dielectrophoretic component becomes negligible inside the constriction due to the locally uniform electric field[64]). The other force occurs in the constriction region due to fluid viscoelastic effects (e.g., the flow-induced structures[76-78]), $\mathbf{F}_{VE}$, which resists the fluid shape change (both fluid squeezing and stretching) and hence acts to impede the electrokinetic particle motion. In the Newtonian fluid, $\mathbf{F}_{VE} = 0$ and so $\mathbf{F}_{EK}$ dominates the particle motion, leading to acceleration and deceleration at the entrance and exit of the constriction. In the non-Newtonian fluid, $\mathbf{F}_{VE}$ increases due to the stretch of PEO polymers around the particle when the particle moves along the constriction. Once $\mathbf{F}_{VE}$ exceeds $\mathbf{F}_{EK}$, the particle motion is reversed and the particle is bounced back towards the constriction entrance. With $\mathbf{F}_{VE}$ being decreased during the

particle's reverse, $\mathbf{F}_{EK}$ will regain the control of the particle motion and drives the particle into the constriction again. This oscillatory motion continues till a sufficiently long chain of particles is formed, for which $\mathbf{F}_{VE}$ is unable to overcome $\mathbf{F}_{VE}$ in the constriction. As both forces depend on the applied electric field, particle size, and PEO concentration (affect both the rheology of the fluid and the wall/particle zeta potentials[79]), we will investigate their effects on particle oscillation in the following section.

2.3.3 Parametric study of particle oscillation in non-Newtonian fluids

1. Electric field effect

FIG. 6(a) shows the snapshot (top) and superimposed (bottom) images of 10 μm particle electrophoresis in 500 ppm PEO solution through the microchannel constriction under the DC electric fields of 100 V/cm (left column), 200 V/cm (middle column), and 400 V/cm (right column), respectively. Particles are uniformly distributed at the upstream of the constriction with a velocity being roughly proportional to the electric field magnitude, which indicates from another angle a shear-rate independent viscosity of the PEO solution. Particles oscillate in the constriction under all electric fields. The oscillating frequency of single particles increases with electric field while the oscillating amplitude goes to the opposite. This implies that the viscoelastic effect grows more quickly than the electrokinetic effect (see FIG. 5). As a result, the length threshold of particle chain for passing through the constriction increases at a higher electric field. For example, single particles may escape from the constriction after a few periods of oscillation at 100 V/cm. In contrast, a chain of more than five particles must be formed at

400 V/cm in order for them to travel to the downstream of the constriction. For comparison, FIG. 6(b) shows the images of 10 μm particle electrophoresis in the Newtonian fluid through the constriction, which exhibit an enhanced particle focusing performance with the increase of electric field due to the induced negative dielectrophoresis in the constriction region.[64]

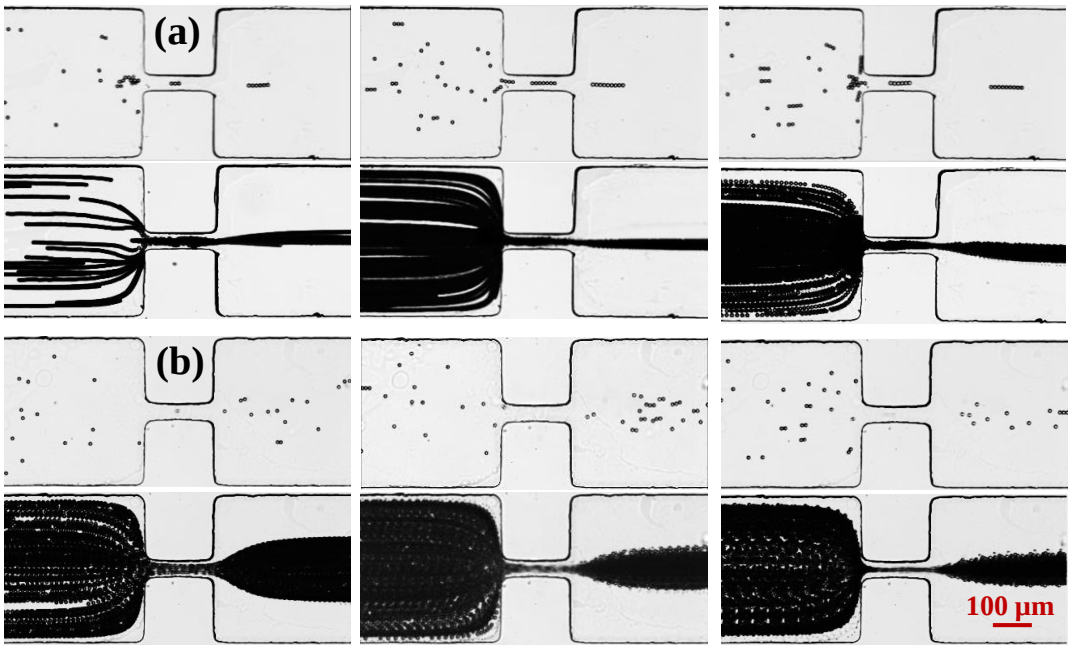

FIG. 6. Snapshot (top) and superimposed (bottom) images illustrating the effects of DC field magnitude on 10 μm particle electrophoresis in (a) non-Newtonian (500 ppm PEO in 1 mM buffer) and (b) Newtonian (1 mM buffer) fluids through the microchannel constriction: 100 V/cm (left column), 200 V/cm (middle column) and 400 V/cm (right column). The fluid flow and particle moving directions are from left to right in all images.

2. PEO concentration effect

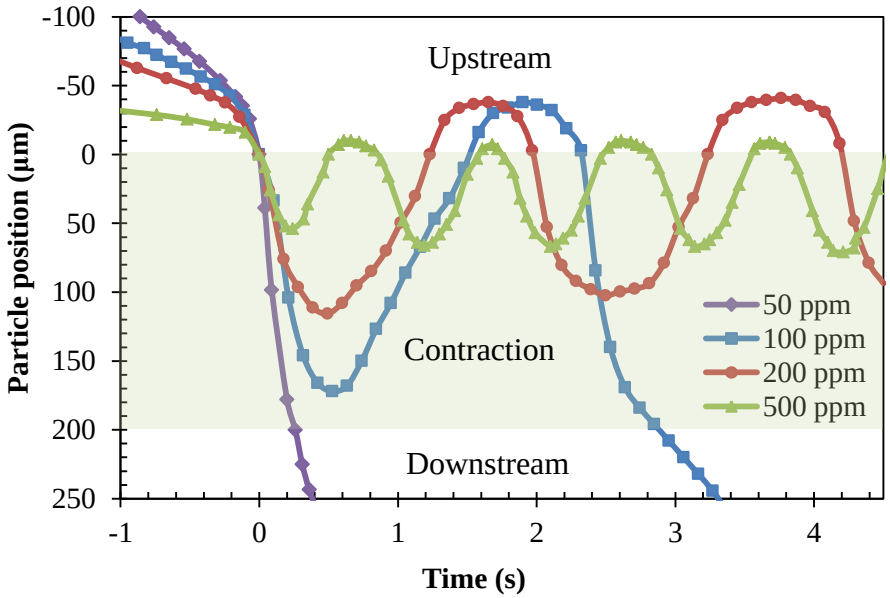

FIG. 7. Effects of PEO concentration (50, 100, 200 and 500 ppm) on the oscillation of single 10 μm particles in the microchannel constriction under 100 V/cm DC electric field. The shaded zone represents the span of the constriction from 0 to 200 μm.

FIG. 7 shows the effects of PEO concentration on the oscillation of single 10 μm particles in the microchannel constriction under a 100 V/cm DC field. The variation of particle position before time 0 (at which the tracked particle enters into the constriction) indicates that particle velocity decreases with the increase of PEO concentration. In 50 ppm PEO solution, the particle exhibits a similar behavior to that in the Newtonian fluid, and passes through the constriction without any complication. When the PEO concentration increases to 100 ppm, weak oscillatory motions are observed where some particles pass in a short chain while others can do so in singles after few oscillations in the constriction. For example, the tracked single particle in 100 ppm PEO solution in FIG. 7 escaped from the constriction after one oscillation only. With the further increase of PEO concentration to 200 ppm and 500 ppm, particle oscillations become robust and

stable with an increased frequency while a reduced amplitude as seen from FIG. 7. Moreover, longer chains must be formed in order for the particles to move through the constriction. These observations are apparently a consequence of the enhanced viscoelastic effects with the increasing PEO concentration.

3. Particle size effect

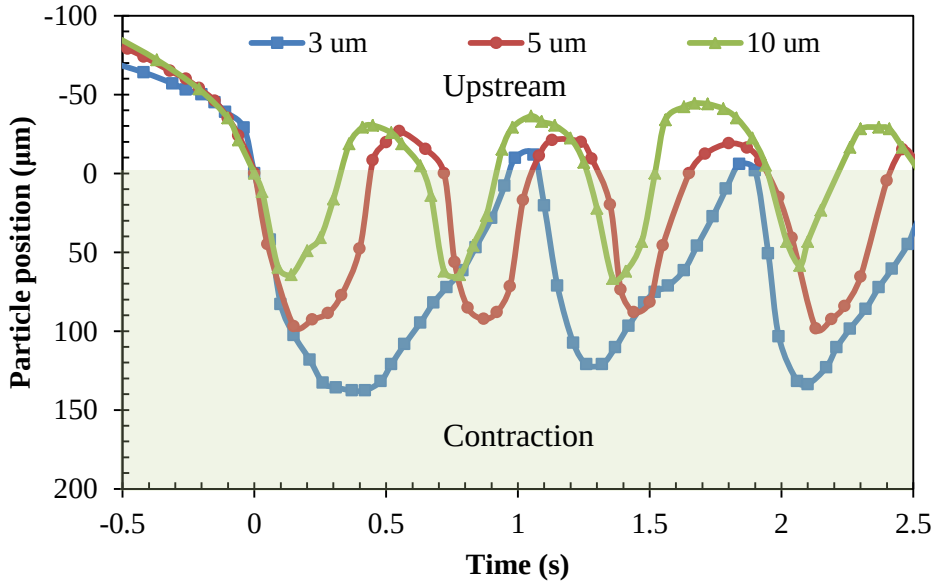

FIG. 8. Effects of particle size (3, 5 and 10 μm in diameter) on the oscillation of single particles in 200 ppm PEO solution in the microchannel constriction under a 200 V/cm DC electric field. The shaded zone represents the span of the constriction from 0 to 200 μm.

FIG. 8 compares the oscillation of single particles of 3 μm, 5 μm, and 10 μm in diameter in 200 ppm PEO solution in the microchannel constriction under a DC electric field of 200 V/cm. These particles move at a similar velocity before the constriction as seen from the nearly overlapping profiles of particle position vs. time in the range of –0.5

s to 0 s. They all undertake oscillations in the constriction. However, larger particles oscillate faster (i.e., with a higher oscillating frequency) with a smaller amplitude. Moreover, analogous to the effects of electric field (see FIG. 6) and PEO concentration (see FIG. 7) that we presented above, larger particles need to form a longer chain in order to pass through the constriction under the same electric field. Therefore, the viscoelastic force (see FIG. 5) increases with particle size because larger particles cause greater distortions to the suspending viscoelastic fluid than smaller ones do. This also implies that particles with a size smaller than a threshold value may not exhibit the oscillating phenomenon any more, which will be studied in our future work.

2.4 Conclusions

We have conducted an experimental study of the DC electrophoretic motion of particles in viscoelastic PEO solutions through a microchannel constriction. In distinct contrast with the particle electrophoresis in a polymer-free Newtonian fluid, particles in a dilute PEO solution are found to bounce backward halfway in the constriction and bounced again towards downstream at the constriction entrance. Such a stream-wise oscillatory particle motion continues and remains inside the constriction until a sufficient number of particles are attached to form a chain for them to escape. The exact mechanism behind this oscillating phenomenon is currently unclear to us, which is speculated to arise from the competition of a viscoelastic force that is induced in the constriction due to, for example, the flow-induced structures[76-78] and an electrokinetic force. We have also examined the effects of the electric field magnitude, particle size and PEO concentration

on the particle oscillation. The increase of either of these parameters can make it more difficult for particles to pass through the constriction. Our future work will find out how the geometry of the constriction may affect the particle electrophoresis in non-Newtonian fluids.

Acknowledgements

This work was supported in part by NSF under grants CBET-0853873 (Xuan) and DMS-1319078 (Qian), and by National Research Foundation of Korea under grant 2011-0014246 (Joo).

References

[1] D. Li, Electrokinetics in microfluidics, Elsevier Academic Press, Burlington, MA (2004).

[2] H. C., Chang and L. Y. Yeo, Electrokinetically Driven Microfluidics and Nanofluidics, Cambridge University Press, New York (2010).

[3] S. Qian and Y. Ai Electrokinetic Particle Transport in Micro/Nanofluidics: Direct Numerical Simulation Analysis, CRC Press (2012).

[4] B. J. Kirby, Micro- and Nanoscale Fluid Mechanics: Transport in Microfluidic Devices, Cambridge University Press (2010).

[5] A. Groisman, M. Enzelberger, and S. Quake, Science **300**, 955–958 (2003).

[6] Y. C. Lam,H. Y. Gan, N. T. Nguyen, and H. Lie, Biomicrofluidics **3**, 014106 (2009).

[7] K. E. Jensen, P. Szabo, F. Okkels, and M. A. Alves, Biomicrofluidics **6**, 044112 (2012).

[8] D. L. Lee, H. Brenner, J. R. Youn, Y. S. Song, Scientific Reports **3**, article number 3258. DOI: 10.1038/srep03258 (2013).

[9] O. L. Hemmingera, P. E. Boukany, S. Q. Wang, and L.J. Lee, J. Non-Newton. Fluid Mech. **165**, 1613-1624 (2010).

[10] P. C. Sousa, F. T. Pinho, M. S. N. Oliveira, and M. A. Alves, Biomicrofluidics **5**, 014108 (2011).

[11] K. Kang, S. S. Lee, K. Hyun, S. J. Lee, and J. M. Kim, Nature Communicat. **4**, article number 2567. doi:10.1038/ncomms3567 (2013).

[12] Y. J. Kang and S. J. Lee, Biomicrofluidics **7**, 054122 (2013).

[13] R. B. Bird, R. C. Armstrong, O. Hassager, Dynamics of Polymeric liquids, vol.1 (1977).

[14] C. J. Pipe and G. H. McKinley, Mech. Research Communicat. **36**, 110-120 (2009).

[15] X. Hu, P. E. Boukany, O. L. Hemminger, L. J. Lee, Macromol. Mater. Eng. **296**, 308-320 (2011).

[16] A. Karimi, S. Yazdi, and A. M. Ardekani, Biomicrofluidics **7**, 021501 (2013).

[17] M. S. N. Oliveira, M. A. Alves, and F. T. Pinho, Transport and Mixing in Laminar Flows: From Microfluidics to Oceanic Currents, 1st Edition. Ed. R. Grigoriev, Wiley-VCH (2012).

[18] C. L. A. Berli, Electrophoresis **34**, 622-630 (2013).

[19] C. Zhao and C. Yang, Adv. Colloid. Interf. Sci. **201-202**, 94-108 (2013).

[20] S. Das and S. Chakraborty, Analytica Chim. Acta **559**, 15-24 (2006).

[21] S. Chakraborty, Analytica Chim. Acta **605**, 175-184 (2007).

[22] C. L. A. Berli and M. L. Olivares, J. Colloid Interf. Sci **320**, 582-589 (2008).

[23] C. Zhao, E. Zholkovskij, J. H. Masliyah, and C. Yang, J. Colloid Interf. Sci **326**, 503-510 (2008).

[24] G. H. Tang, X. F. Li, Y. L. He, and W. Q. Tao, J. Non-Newtonian Fluid Mech. **157**, 133-137 (2009).

[25] M. L. Olivares, L. Vera-Candioti, and C. L. A. Berli, Electrophoresis **30**, 921-929 (2009).

[26] C. Zhao and C. Yang, Electrophoresis **31**, 973-979 (2010).

[27] M. Hadigol, R. Nosrati, and M. Raisee, Colloid Surf. A **374**, 142-153 (2011).

[28] A. Babaie, A. Sadeghi, and M. H. Saidi, J. Non-Newtonian Fluid Mech. **185-186**, 49-57 (2012).

[29] Y. J. Chang, P. W. Yang, and H. F. Huang, J. Non-Newtonian Fluid Mech. **194**, 32-41 (2013).

[30] C. Zhao and C. Yang, Electrophoresis **34**, 662-667 (2013).

[31] A. M. Afonso, M.A. Alves, and F.T. Pinho, J. Non-Newtonian Fluid Mech. **159**, 50-63 (2009).

[32] S. Dhinakaran, A. M. Afonso, M. A. Alves, and F.T. Pinho, J. Colloid Interf. Sci **344**, 513-520 (2010).

[33] J. J. Sousa, A. M. Afonso, F. T. Pinho, and M. A. Alves, Microfluid. Nanofluid. **10**, 107-122 (2011).

[34] A. M. Afonso, F.T. Pinho, and M. A. Alves, J. Non-Newtonian Fluid Mech. **179-180**, 55-68 (2012).

[35] W. Choi, S. Woo Joo, and G. Lim, J. Non-Newtonian Fluid Mech. **187-188**, 1-7 (2012).

[36] A. M. Afonso, M. A. Alves, and F. T. Pinho, J. Colloid Interf. Sci **395**, 277-286 (2013).

[37] W. B. Zimmerman, J. M. Rees, and T. J. Craven, Microfluid. Nanofluid. **2**, 481-492 (2006).

[38] T. J. Craven, J. M. Rees, and W. B. Zimmerman, Microfluid. Nanofluid. **9**, 559-571 (2010).

[39] C. Zhao and C. Yang, Biomicrofluidics **5**, 014110 (2011).

[40] C. Zhao and C. Yang, Appl. Math. Comput. **211**, 502-509 (2011).

[41] H. M. Park and W. M. Lee, J. Colloid Interf. Sci **317**, 631-636 (2008).

[42] Q. Liu, Y. Jian, and L. Yang, J. Non-Newtonian Fluid Mech. **166**, 478-486 (2011).

[43] C. O. Ng, J. Non-Newtonian Fluid Mech. **198**, 1-9 (2013).

[44] E. Lee, Y. F. Huang, and J. P. Hsu, J. Colloid Interface Sci. **258**, 283-288 (2003).

[45] E. Lee, C. S. Tsai, J. Hsu, and C. J. Chen, Langmuir **20**, 7952-7959 (2004).

[46] E. Lee, C. T. Chen, and J. P. Hsu, J. Colloid Interface Sci. **282**, 857-864 (2005).

[47] J. P. Hsu, L. H. Yeh, and M. H. Ku, Colloid Polym. Sci. **284**, 886-892 (2006).

[48] J. P. Hsu and L. H. Yeh, Langmuir **23**, 8637-8646 (2007).

[49] J. P. Hsu, L. H. Yeh, and S. J. Yeh, J. Phys. Chem. B **111**, 12351-12631 (2007).

[50] L. H. Yeh and J. P. Hsu, Microfluid. Nanofluid. **7**, 383-392 (2009).

[51] J. P. Hsu, C. Y. Chen, L. H. Yeh, and S. Tseng, Colloid Surface B **69**, 8-14 (2009).

[52] A. S. Khair, D. E. Posluszny, and L. M. Walker, Phys. Rev. E **85**, 016320 (2012).

[53] F. A. Morrison, J. Colloid Interface Sci. **34**, 210-214 (1970).

[54] F. M. Chang and H. K. Tsao, Appl. Phys Lett. **90**, 194105, 2007.

[55] R. M. Bryce and M. R. Freeman, Phys. Rev. E **81**, 036328 (2010).

[56] R. M. Bryce and M. R. Freeman, Lab Chip **10**, 1436-1441 (2010).

[57] W.W. Graessley, Polymer **21**, 258–262 (1980).

[58] D. F. James, Annu. Rev. Fluid Mech. **41**, 129-42 (2009).

[59] L. E. Rodd, J. J. Cooper-White, D. V. Boger, G. H. McKinley, J. Non-Newtonian Fluid Mech. **143**, 170-191 (2007).

[60] M. Rubinstein and R. H. Colby, Polymer Physics, Oxford University Press Inc. (2003).

[61] V. Tirtaatmadja, G. H. Mckinley, and J. J. Cooper-White, Phys. Fluid. **19**, 043101 (2006).

[62] J. Zhu, S. Sridharan, G. Hu, and X. Xuan, J. Micromech. Microeng. **22**, 075011 (2012).

[63] A. Kale, S. Patel, G. Hu, and X. Xuan, Electrophoresis **34**, 674-683 (2013).

[64] J. Zhu and X. Xuan, Electrophoresis **30**, 2668-2675 (2009).

[65] G. H. McKinley, Transport Processes in Bubbles, Drops & Particles, chapter 14, 2nd Ed. Ed. R. Chhabra, D. De Kee, Taylor & Francis (2001).

[66] L. E. Becker, G. H. McKinley, H. K. Rasmussen, and O. Hassager, J. Rheol. **38**, 377-403 (1994).

[67] C. Bodart, and M. J. Crochet, J. Non-Newton. Fluid Mech. **54**, 303-329 (1994).

[68] W.M. Jones, A.H. Price, and K. Walters, J. Non-Newton. Fluid Mech. **53**, 175-196 (1994).

[69] M J. King and N. D. Waters, J. Phys. D **5**, 141-150 (1972).

[70] R. Zheng and N. Phan-Thien, Rheol. Acta **31**, 323-332 (1992).

[71] M. B. Bush, J. Non-Newtonian Fluid Mech. **55**, 229-247 (1994).

[72] M. T. Arigo and G. H. Mckinley, J. Rheol. **41**, 103-128 (1997).

[73] M. T. Arigo and G. H. Mckinley, Rheol. Acta **37**, 307-327 (1998).

[74] S. Chen and J. P. Rothstein, J. Non-Newtonian Fluid Mech. **116**, 205-234 (2004).

[75] S. von Kann, J. H. Snoeijer, and D. van der Meer, Phys. Rev. E **87**, 042301 (2013).

[76] A. M. Mollinger, E. C. Cornelissen, and B. H. A. A. van den Brule, J. Non-Newtonian Fluid Mech. **86**, 389-393 (1999).

[77] N. Kumar, S. Majumdar, A. Sood, R. Govindarajan, S. Ramaswamy, and A. K. Sood, Soft Matt. **8**, 4310-4313 (2012).

[78] A. Jayaraman and A. Belmonte, Phys. Rev. E **67**, 065301(R) (2003).

[79] J. Horvath and V. Dolnik, Electrophoresis **22**, 644-655 (2001).

[80] L. E. Rodd, T. P. Scott, D. V. Boger, J. J. Cooper-White, and G. H. McKinley, J. Non-Newtonian Fluid Mech. **129**, 1–22 (2005).

CHAPTER THREE

VISCOELASTIC EFFECTS ON ELECTROKINETIC PARTICLE FOCUSING IN A CONSTRICTED MICROCHANNEL

Abstract

Focusing suspended particles in a fluid into a single file is often necessary prior to continuous-flow detection, analysis and separation. Electrokinetic particle focusing has been demonstrated in constricted microchannels by the use of the constriction-induced dielectrophoresis. However, previous studies on this subject have been limited to Newtonian fluids only. We report in this paper an experimental investigation of the viscoelastic effects on electrokinetic particle focusing in non-Newtonian polyethylene oxide (PEO) solutions through a constricted microchannel. The width of the focused particle stream is found NOT to decrease with the increasing DC electric field, which is different from that in Newtonian fluids. Moreover, particle aggregations are observed at relatively high electric fields to first form inside the constriction. They can then either move forward and exit the constriction in an explosive mode or roll back to the constriction entrance for further accumulations. These unexpected phenomena are distinct from the findings in our earlier paper (Lu et al. *Biomicrofluidics* 2014, 8, 021802), where particles are observed to oscillate inside the constriction and not to pass through until a chain of sufficient length is formed. They are speculated to be a consequence of the fluid viscoelasticity effects.

3.1 Introduction

Focusing suspended particles in a fluid into a single file is often important and necessary in order to continuously detect, analyze and sort them for numerous applications.[1,2] Sheath flow focusing is the most routine particle focusing method in microfluidic devices because it uses sheath fluids to pinch the particulate solution and works effectively for particles of essentially any size.[3,4] However, a precise control of the flow rate and a large consumption of the sheath fluid are the drawbacks of this method. In contrast, sheathless focusing of particles relies on a force field to act directly on the suspended particles and move them laterally for alignment, which is often flexible in control and simple in operation. So far a variety of forces have been demonstrated to focus particles in microfluidic devices, which can be either externally imposed like acoustic,[5] electric,[6] magnetic[7] and optical[8] forces etc. or internally induced like inertial[9], viscoelastic[10-13], hydrodynamic[14] and dielectrophoretic[15] forces. However, these methods often suffer from low effectiveness when working with small particles due to the strong size-dependence of nearly, if not all, every force field.[1,2]

Electrokinetic flow is an efficient means to transport fluids and particles in microfluidic devices under DC electric fields due to its excellent scalability and easy connection.[16,17] It has been exploited to drive both the particulate and sheath solutions in sheath flow focusing of particles.[18,19] It has also been demonstrated to pump the particulate solution while simultaneously manipulating the suspended particles into equilibrium position(s) for a sheathless focusing. The latter function is achieved primarily through the use of a geometry-induced dielectrophoretic motion, which is the translation of particles (either charged or neutral) in response to electric field gradients.[19] Such an

insulator-based dielectrophoretic focusing of particles has been demonstrated in both constricted[20,21] and curved[22,23] microchannels. However, all these studies have been limited to Newtonian fluids only, in which fluid electroosmosis and particle electrophoresis are simply a linear function of the applied DC electric field. As many of the fluids used in capillary electrophoresis and microfluidic devices, such as polymer solutions and bodily fluids, are complex,[24-32] it is important from the aspects of both fundamentals and applications to study how electrokinetic particle focusing may be affected by the fluid non-Newtonian effects.

While a number of theoretical studies have been reported on, for example, the shear thinning/thickening and viscoelastic effects on fluid electroosmosis and particle electrophoresis in non-Newtonian fluids,[33-45] much less has been done through experimental investigation and validation. In a recent study from Chang and Tsao[46] a significant drag reduction was observed in electroosmotic flow of polymer solutions. This was attributed to the polymer depletion in the electric double layer, and the drag reduction was found to increase with the ratio of the polymer size to the electric double layer thickness. In a more recent study Bryce and Freeman[47] observed an extensional instability in the electroosmotic flow of dilute polymer solutions through a microchannel constriction, which, however, was found later by the same group to actually reduce the fluid mixing as compared to that in polymer-free fluids.[48]

Very recently we have conducted an experimental study of electrokinetic particle motion in polyethylene oxide (PEO) solutions through a microchannel constriction.[49] No apparent electrokinetic focusing of particles was observed, which is distinctly different

from what has been previously demonstrated in Newtonian fluids.[20,21] Instead, an unexpected particle oscillation occurred in the constriction, which continued until a particle chain of sufficient length was formed. This phenomenon is found to persist for particles of different sizes as long as they move along with the electric field. It also holds true when the applied DC electric field or the PEO concentration is varied. However, as we will present in this experimental work, particles that move against the electric field in PEO solutions do not experience such oscillations in a constricted microchannel. They can be electrokinetically focused with a different trend from that in Newtonian fluids when the electric field is increased. Moreover, particle aggregations can be formed inside the constriction with subsequent interesting behaviors.

3.2 Experiment

3.2.1 Preparation of non-Newtonian fluids and particle suspensions

Non-Newtonian fluids were prepared by dissolving PEO powder (Sigma-Aldrich USA, average molecular weight M_w = 4×10^6 Da) into 1 mM phosphate buffer at concentrations of 50 ppm (i.e., dissolving 50 mg PEO powder into 1 litre buffer), 100 ppm, 200 ppm, and 500 ppm, respectively. It is important to note that PEO solutions at similar concentrations have been frequently used in the literature to study the viscoelasticity effects on hydrodynamic fluid flows[50-52] and particle motions[53-55] in microchannels. The concentration we used are all lower than the overlapping concentration (c^* = 547 ppm[49]) of the PEO, indicating that all four prepared solutions are in the dilute regime. The shear viscosities of these solutions were measured in a Couette

geometry (ARES LS/M, TA instruments) at room temperature. Nearly constant values of 1.1 mPa·s, 1.2 mPa·s, 1.4 mPa·s and 2.0 mPa·s, respectively, were obtained for the four PEO concentrations in the range of shear rate from 50 s^{-1} to 1,000 s^{-1}. The relaxation times of these solutions were estimated to be 4.07 ms, 6.39 ms, 10.01 ms, and 18.17 ms, respectively. The detailed process for calculating these values and the list of other properties of the PEO solutions can be referred to Lu et al.[45]

The non-Newtonian particle suspensions were made by re-suspending polystyrene spheres of 3.1 μm, 4.8 μm, and 9.9 μm in diameter (Thermo Scientific) in the PEO solution(s) to a final concentration of about 10^6 particles per milliliter. To illustrate the viscoelastic effects, 9.9 μm particles were also re-suspended in the base fluid of the PEO solutions, i.e., 1 mM pure buffer, which is a Newtonian fluid, for a direct comparison. A small amount of Tween 20 (0.5% in volume ratio, Fisher Scientific) was added to both the Newtonian and non-Newtonian particle suspensions for the purpose of suppressing particle-wall and particle-particle adhesions. The effective electric conductivity, σ_p, of particles was calculated from $\sigma_p = 4\sigma_s/d$ with σ_s = 1 nS being the particle's surface conductance and d the particle diameter.[56] It was found to be 12.90, 8.33 and 4.04 μS/cm for 3.1, 4.8 and 9.9 μm-diameter particles, respectively. Because these conductivity values are all much smaller than that of the suspending fluid (approximately 200 μS/cm), negative DEP are expected to occur under the application of DC electric fields in both the Newtonian and non-Newtonian fluids.

3.2.2 Experimental setup

The standard soft lithography method is used in the fabrication of microchannels, as detailed by Lu et al.[49] The polydimethylsiloxane (PDMS) microchannel is sealed from bottom by a regular glass slide, through which Joule heating can be dissipated relatively easily to avoid significant temperature rises in the particle suspensions.[57] The 40 μm-deep microchannel is overall 1 cm long and 400 μm wide with a constriction of 200 μm length and 40 μm width in the middle. The electrokinetic fluid and particle motions in the microchannel were driven by DC electric fields, supplied by a DC power supply (Glassman High Voltage Inc., High Bridge) through the end-channel reservoirs. The electric field magnitude was kept no more than 500 V/cm in order to minimize Joule heating effects in the constriction region.[58] Pressure-driven fluid and particle motions were eliminated by balancing the liquid heights in the inlet and outlet reservoirs prior to each test. Particle transport in the microchannel constriction was visualized and recorded through an inverted microscope (Nikon Eclipse TE2000U, Nikon Instruments) with a CCD camera (Nikon DS-Qi1Mc) at a rate of 15 frames per second. The videos and images obtained were post-processed using the Nikon imaging software (NIS-Elements AR 2.3). Particle streak images were obtained by superimposing a sequence of 600 images.

3.2.3 Measurement of electrokinetic particle mobility

The electrokinetic velocity of particles, $\mathbf{U}_{EK}$, in a microchannel is the vector addition of electroosmotic fluid velocity, $\mathbf{U}_{EO}$, and electrophoretic particle velocity, $\mathbf{U}_{EP}$,

$$\mathbf{U}_{EK} = \mathbf{U}_{EO} + \mathbf{U}_{EP} = \frac{\varepsilon\left(\zeta_p - \zeta_w\right)}{\eta}\mathbf{E} \tag{1}$$

where ε is the dielectric permittivity of the suspending fluid, ζ_p is the zeta potential of the particle, ζ_w is the zeta potential of the channel wall due to the spontaneous formation of electric double layer at the fluid-wall interface, η is the fluid dynamic viscosity, and **E** is the applied DC electric field. It was determined from the measured particle travelling distance over a time interval in the microchannel. The measuring region is distant from the channel entrance and the constriction so that the local electric field and particle velocity both remain constant. The electrokinetic mobility of particles, μ_{EK}, was calculated from the electrokinetic velocity divided by the local DC electric field (numerically computed in COMSOL, Burlington, MA),

$$\mu_{EK} = \frac{\varepsilon\left(\zeta_p - \zeta_w\right)}{\eta} \tag{2}$$

which is apparently a function of the physicochemical properties of the tested fluid-particle-channel system. In our experiments, particles travel from the cathode to the anode in both the Newtonian and non-Newtonian solutions, i.e., $\mu_{EK} < 0$, which indicates the dominance of particle electrophoresis over fluid electroosmosis. This is because the electroosmotic fluid motion is nearly always from the anode to the cathode, i.e., $\zeta_w < 0$[16,17,30] and hence $\zeta_p < \zeta_w < 0$ or $|\zeta_p| > |\zeta_w|$.

The observed direction of the electrokinetic motion of particles from Thermo Scientific in the current work is contrary to that of the particles from Sigma Aldrich used in our previous paper.[49] Therefore, fluid electroosmosis should dominate over particle

electrophoresis in the latter case, leading to $\zeta_w < \zeta_p < 0$ or $|\zeta_w| > |\zeta_p|$ based on a similar analysis to the above. While both types of particles are made of polystyrene as per the product manuals, only the particles from Thermo Scientific are fluorescently dyed. This may be responsible for the observed difference in particle zeta potential, ζ_p, between the two types of particles. The electrokinetic particle mobility is found to be nearly independent of the particle size in all the solutions tested in this work. However, the addition of PEO into the buffer solution increases the particle mobility, which is also different from those particles used in our previous paper.[49] Specifically, the measured particle mobility is 2.6×10^{-8} $m^2/(V\cdot s)$ in the 500 ppm PEO solution, and found to decrease by less than 10% when the PEO concentration is varied from 500 ppm to 50 ppm. In contrast, the electrokinetic particle mobility is only 1.3×10^{-8} $m^2/(V\cdot s)$ in the Newtonian buffer solution. Since the viscosity of the 500 ppm PEO solution is nearly twice that of the Newtonian buffer, the wall zeta potential, ζ_w, in the former is anticipated to be significantly smaller from Eq. (2). This can be attributed to the suppression of electroosmotic flows as a result of the coating of neutral PEO polymers onto the channel walls.[59] It is important to note that electrophoresis may also be suppressed by the PEO coating on particle surfaces, which requires a detailed study of the PEO effects on wall and particle zeta potentials.

3.3 Results and discussion

3.3.1 Comparison of electrokinetic particle focusing in Newtonian and non-Newtonian fluids

FIG. 1 compares in the form of superimposed images the electrokinetic focusing of 9.9 μm-diameter particles in Newtonian (a, 1 mM buffer) and non-Newtonian (b, 200 ppm PEO in 1 mM buffer) fluids through the microchannel constriction. The applied DC electric field increases from 100 V/cm to 400 V/cm for the images from left to right. At 100 V/cm particles exit the constriction in a narrower stream in both fluids. This focusing effect is attributed to the constriction-induced DEP that has been demonstrated in previous studies with Newtonian fluids.[60] As the electric field increases from 100 V/cm to 300 V/cm, the particle stream width in the pure buffer becomes thinner after the constriction (see FIG. 1(a)), indicating an enhanced electrokinetic focusing. This observation is consistent with previous studies[20,21,60] and occurs due to the greater increase in dielectrophoretic motion than in electrokinetic motion at larger electric fields. Such a decrease in the focused particle stream width also agrees reasonably with the predictions of a Lagrangian tracking method-based numerical model in COMSOL (data not shown). In the PEO solution, however, the electrokinetic particle focusing turns out NOT to increase with the applied electric field. As measured directly from the top edge of the images (i.e., where particles travel out of the images) in FIG. 1(b), the focused particle stream width (note the wider particle stream, the worse focusing) actually increases from 176 μm to 216 μm and 240 μm when the electric field is increased from 100 V/cm to 300 V/cm. Moreover, the particles at the edges of the focused streams are scattered, which seems not to be a strong function of the applied electric field. This dispersion phenomenon is not obvious for particles in the Newtonian buffer (see FIG. 1(a)).

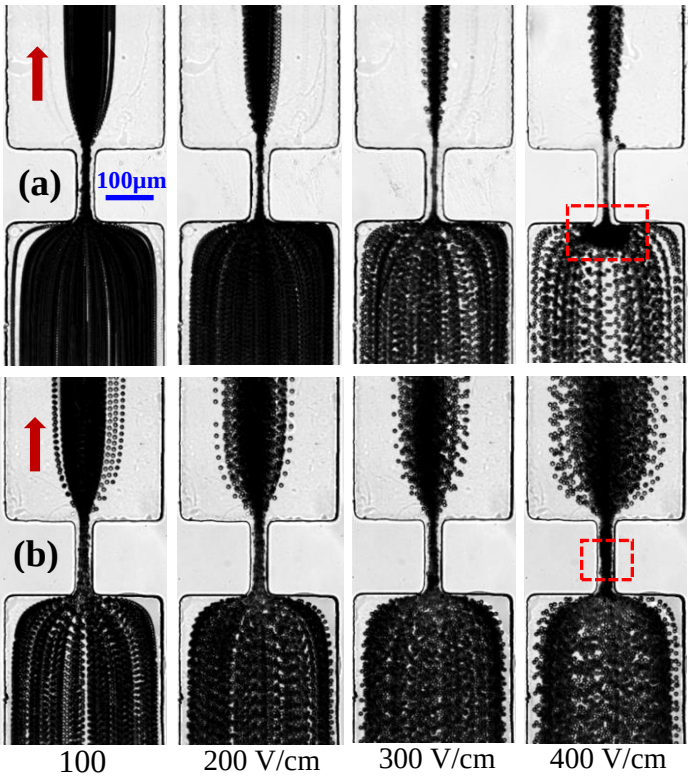

FIG. 1. Superimposed images illustrating the effects of fluid viscoelasticity on electrokinetic focusing of 9.9 μm particles in a constricted microchannel under various DC electric fields: (a) Newtonian fluid (1 mM buffer); (b) non-Newtonian fluid (200 ppm PEO in 1 mM buffer). The block arrows indicate the particle moving direction, which is from bottom to top in all images and against the electric field direction. The two dashed boxes on the right-most images highlight the regions in which the particle trapping is initiated. A clear demonstration of the observed particle trapping phenomenon in the PEO solution is presented as snapshot images in FIG. 2. Note that the widths of the focused particle streams referred to in the text (see also FIG. 3 and FIG. 4) were all measured directly from the top edge of the images where particles travel out.

To further verify the trend of this reduced particle focusing with electric field, we also studied the electrokinetic motion of similar sized particles from other companies in the same PEO solution: one is the 9.9 μm-diameter particle from Duke Scientific, and the other is the 10.14 μm-diameter particle from Bangs Laboratories. Each type of these particles moved from the cathode to the anode though at a dissimilar electrokinetic

mobility from the particles in FIG. 1(b). We observed a similar trend of weakened electrokinetic particle focusing with an increase in electric field for both particles (data not shown). Thus, the viscoelasticity of the PEO solution is believed to be a factor contributing to this phenomenon. We speculate that fluid viscoelasticity draws disturbances to electrokinetic particle motion in the constriction region due to the shear-induced electroosmotic fluid instability that has been recently demonstrated experimentally[47,48] and numerically.[61] Such a de-focusing effect increases more quickly with electric field than the constriction-induced dielectrophoretic force does, and consequently the electrokinetic particle focusing gets worse at higher electric fields. In addition, it is important to note that the reported particle oscillations and formation of particle chains in our previous paper[49] are absent from the constriction in this work for all the three types of particles under test. This change appears to be associated with the direction of the electrokinetic particle motion, which may be due to the dominant particle electrophoresis over fluid electroosmosis in this work as analyzed earlier.

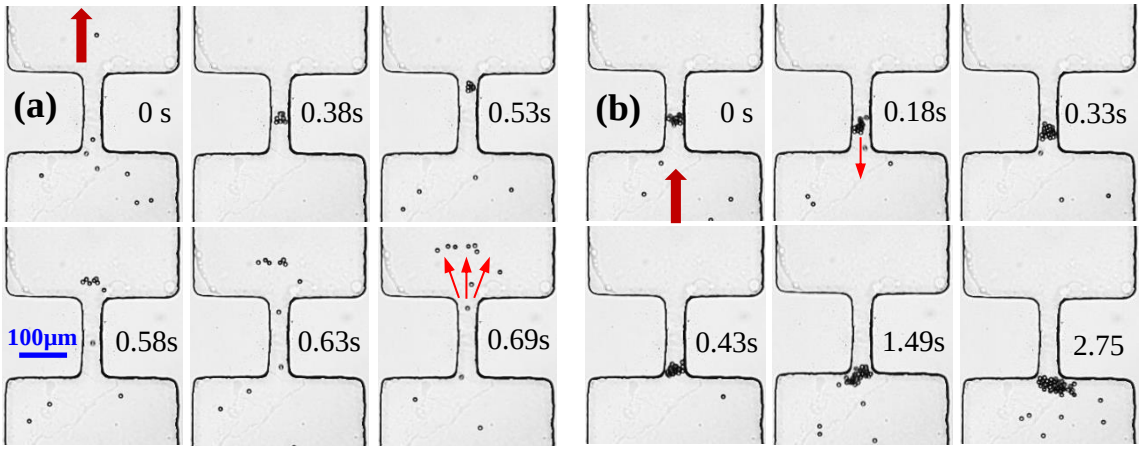

FIG. 2. Sequential images (with the relative time instants labeled) illustrating the forward ejection (a) and backward rolling (b) of 9.9 μm-diameter particle aggregations in a non-Newtonian (200 ppm PEO) fluid through the microchannel constriction. The applied DC

electric field is 400 V/cm. The block arrow indicates the overall particle moving direction in the microchannel, which is from bottom to top in all images and against the electric field direction (from top to bottom). The thin arrows indicate the moving directions of the particle clusters that are formed first inside the constriction (Multimedia view).

When the DC electric field applied was further increased to 400 V/cm, particles in the Newtonian fluid started being trapped at the constriction entrance (highlighted by a dashed box on the right-most image in FIG. 1(a)). This happens because the constriction-induced DEP becomes strong enough to counterbalance the electrokinetic motion in the streamline direction. However, particles cannot be fully trapped until an even higher electric field is applied because of the influence of the trapped particles on the local electric field gradients.[62] In contrast, electrokinetic particle trapping also occurs in the 200 ppm PEO solution at 400 V/cm but initiates inside the constriction (see the dashed-box highlighted region on the right-most image in FIG. 1(b)), and proceed in either a forward or a backward direction. As viewed from the first two images in FIG. 2(a) (Multimedia view), an aggregation of particles can be formed first inside the constriction, which was not observed in our previous work for particles moving in the electric-field direction.[49] More interestingly, the particle cluster can then either move forward, albeit slower than single particles, and exit the constriction in an explosive mode, as illustrated by the sequential images (see the thin arrows for the moving direction of the particle cluster) in FIG. 2(a). Or alternatively, the particle cluster can roll back to the constriction entrance, where it grows continuously bigger and bigger with additional particles trapped. This process is demonstrated by the image sequence in FIG. 2(b) (Multimedia view), where, as seen from the labeled time instants, the backward-moving speed of the particle

cluster within the constriction is comparable to the forward-moving speed of the particle cluster in FIG. 2(a). The formation and subsequent movement of particle aggregations in the constriction are speculated to be a consequence of the combined effects of viscoelastic instability[47,48] and particle-particle interactions.[63] The exact mechanisms behind the observed phenomena in FIG. 1 and FIG. 2 are, however, currently unclear to us, for which a systematic study (especially theoretical) of the electroosmotic flow field and the fluid-particle-electric field interactions will be needed.

3.3.2 PEO concentration effect

FIG. 3 shows the effects of PEO concentration on the stream width of electrokinetically focused 9.9 μm particles in the microchannel constriction. The applied DC electric field is varied from 100 V/cm to 400 V/cm. The superimposed particle images in all tested PEO solutions (except for 200 ppm which is shown in FIG. 1) are presented in FIG. 4. The focused particle stream widths in all tested PEO solutions (including 50, 100, 200 and 500 ppm) are larger than that in the Newtonian fluid. This is mainly because the electrokinetic particle mobility in the latter is only approximately half of that in a PEO solution. Moreover, the constriction-induced particle DEP is smaller in a PEO solution due to its greater viscosity than the Newtonian buffer. Interestingly particles in 50 ppm PEO solution behave similar to those in the Newtonian fluid (see FIG. 1(a)), and achieve an enhanced electrokinetic focusing (i.e., a decreased particle stream width) at a greater electric field. This indicates a relatively weak viscoelastic effect at a PEO concentration of 50 ppm, which is consistent with the observation in our

previous study.[49] In contrast, the focused particle stream widths in all other tested PEO solutions expand with the increase of electric field. Moreover, a higher PEO concentration yields a weaker electrokinetic particle focusing. These phenomena are all supposed to result from the stronger viscoelastic effects when the PEO concentration is increased. Interestingly, the opposite trends of particle focusing vs. electric field in 50 and 100 ppm PEO solutions imply that there exists a critical PEO concentration at which particle focusing is insensitive to electric field. This may occur due to the balance of viscoelastic disturbances and dielectrophoretic focusing at the constriction, which will be studied in more details in the future. In addition, it is found that particle aggregations are not formed inside the constriction in 50 ppm PEO solution even at very high electric fields. However, they can easily occur at 400 V/cm (indicated by unfilled symbols in FIG. 3) in all other tested PEO solutions with similar behaviors to those illustrated in FIG. 2.

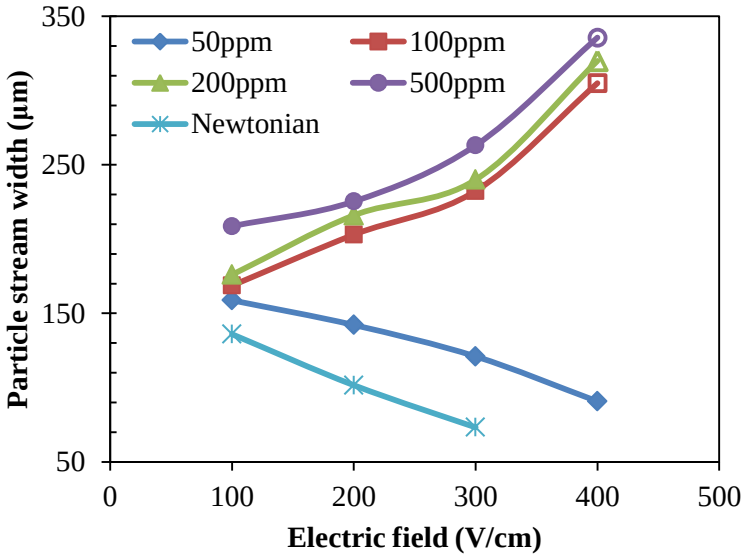

FIG. 3. Effects of PEO concentration (0, 50, 100, 200 and 500 ppm) on the stream width of electrokinetically focused 9.9 μm particles in the microchannel constriction at different DC electric fields. Error bars are included for only the data in the 500 ppm PEO solution for a better view, which are determined from the reading error in identifying the edges of the focused particle stream. The unfilled symbols represent the points at which particle aggregation was observed inside the constriction. The particle stream widths of these points are each measured from the superimposed images prior to the occurring of particle aggregation.

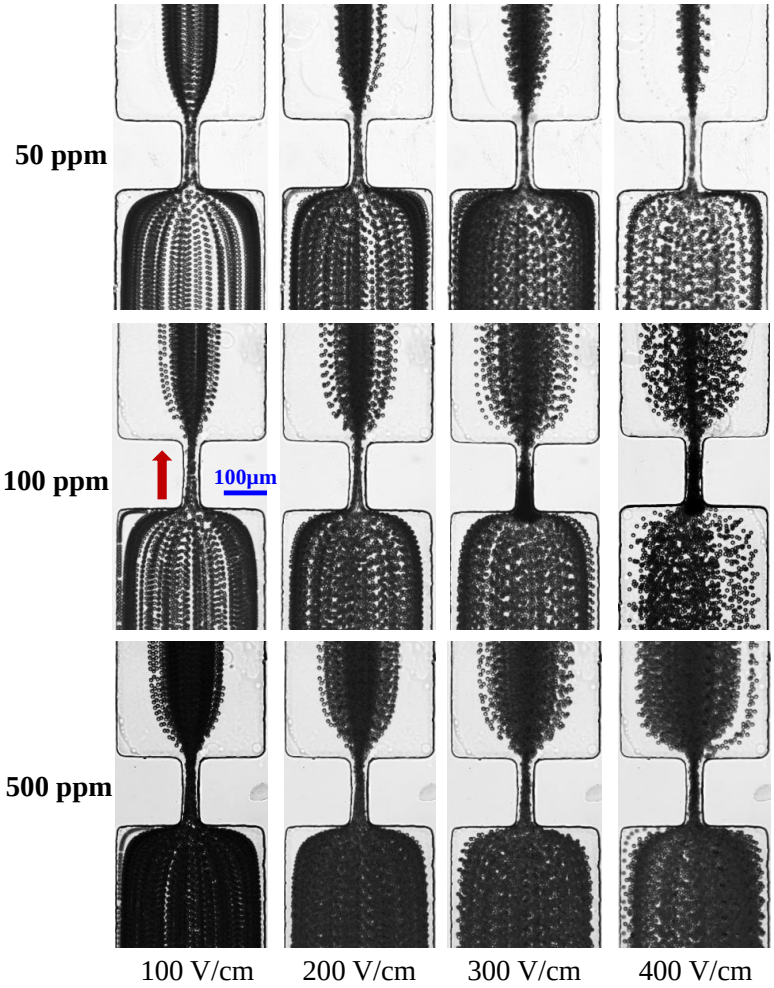

FIG. 4. Superimposed images illustrating the electrokinetic focusing of 10 μm-diameter particles in PEO solutions of various concentrations (0 and 200 ppm are referred to Fig. 1) under four different DC electric fields. The block arrow indicates the particle moving direction in all images.

3.3.3 Particle size effect

To examine whether particle size contributes to the peculiar electrokinetic focusing phenomena in non-Newtonian fluids explained above, we also studied the electrokinetic motions of 3.1 μm and 4.8 μm particles in 200 ppm PEO solution in the constricted microchannel under various DC electric fields. The superimposed particle images are presented in FIG. 5. The experimentally measured stream widths of these particles at different electric fields are presented in FIG. 6 along with the ones for 9.9 μm particles (see also FIG. 1(b)). The general trend that the electrokinetic focusing deteriorates with the increase of electric field persists for the two smaller particles. The extent of variation in the focused particle stream width with electric field, however, turns out to be dependent on particle size. At low electric fields (e.g., 100 V/cm), larger particles achieve, as expected, a better focusing than smaller ones because the former experience a stronger DEP while viscoelastic effects are still relatively weak. At high electric fields (e.g., 300 V/cm), the relationship among the three focused particle stream widths becomes complicated, as seen from FIG. 6. This is likely because viscoelastic effects are a complex function of both electric field and particle size, which requires further studies. In addition, similar forward and backward motions of particle clusters (see FIG. 2) are also observed within the constriction for both 3.1 μm and 4.8 μm particles but under an increased electric field of around 500 V/cm.

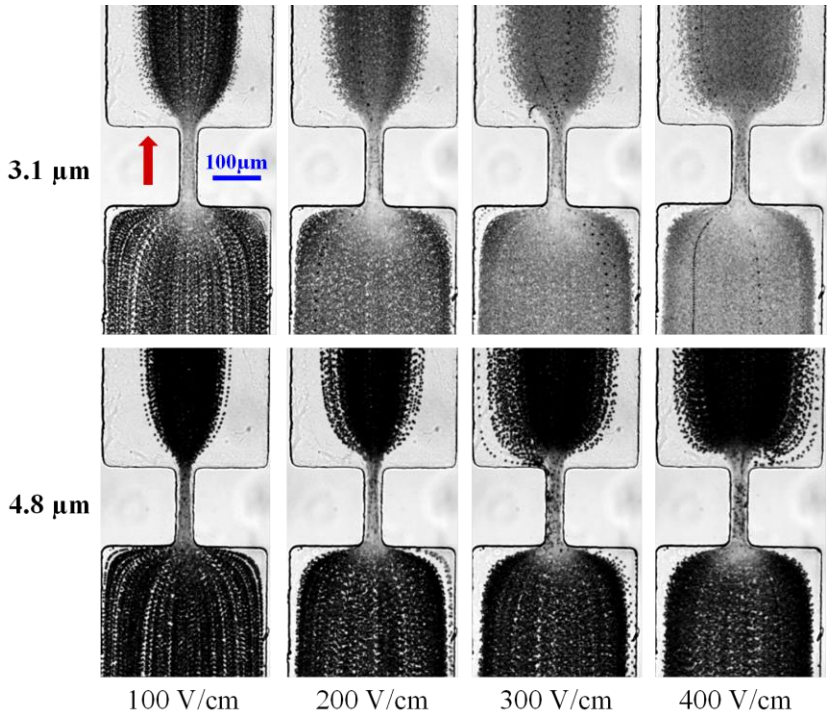

FIG. 5. Superimposed images illustrating the electrokinetic focusing of 3.1 µm and 4.8 µm-diameter particles (the images for 9.9 µm particles are referred to FIG. 1) in 200 ppm PEO solution under four different DC electric fields. The block arrow indicates the particle moving direction in all images.

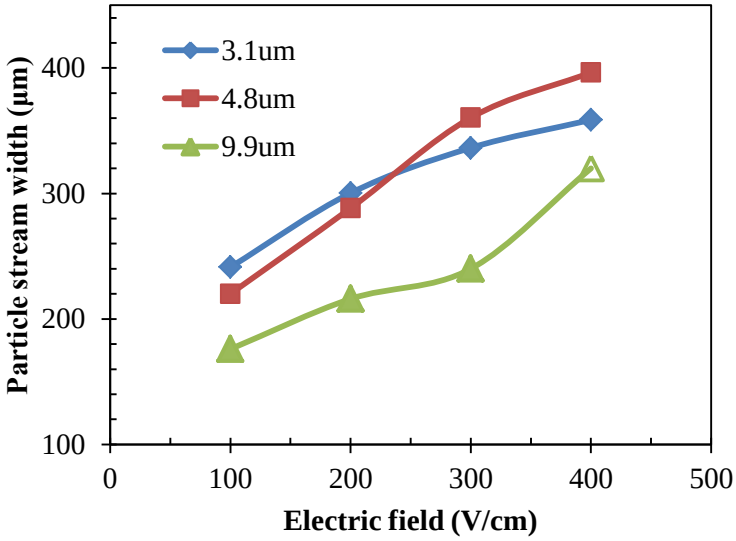

FIG. 6. Experimentally measured stream widths of the electrokinetically focused particles with different sizes in 200 ppm PEO solution in the constricted microchannel. The unfilled symbol for 9.9 µm particles represents the point at which particle

aggregation inside the constriction was observed. The particle stream width of this point is obtained from the superimposed images prior to the occurring of particle aggregation.

3.4 Conclusions

We have experimentally studied the electrokinetic particle focusing in viscoelastic PEO solutions through a 10:1 ratio microchannel constriction. Particles are found to be less focused with the increase of the applied DC electric field, which is different from the focusing trend in Newtonian fluids. Also, particle aggregations are formed first inside the constriction at high electric fields while the purely dielectrophoretic trapping of particles in Newtonian fluids only occurs at the entrance of the constriction. More surprisingly, the particle aggregation can either move forward and be ejected from the constriction in an explosive manner, or roll back and grow bigger in size at the constriction entrance with more particles getting trapped. All these interesting phenomena are owed to the fluid viscoelasticity effects that are speculated to be a stronger function of electric field than DEP. The exact mechanisms underlying these phenomena deserve intensive future studies. We have also examined the effects of PEO concentration and particle size on the electrokinetic particle focusing behavior in the constricted microchannel. The viscoelastic perturbations to particle focusing and trapping are found to increase with the PEO concentration for larger particles. Since the observed particle focusing in all tested PEO solutions is worse than in the Newtonian fluid, we conclude that constriction-induced DEP is not a good option for electrokinetic focusing of particles suspended in non-Newtonian fluids. However, the demonstrated particle oscillation[49] and aggregation under relative low electric fields may find applications in bead-based assays.[64,65]

Acknowledgements

This work was partially supported by Clemson University through a departmental SGER (Small Grants for Exploratory Research) grant to Xuan.

References

[1] D. A. Ateya, J. S. Erickson, P B. Howell Jr, L. R. Hilliard, J. P. Golden and F. S. Ligler Anal. Bioanal. Chem. **391**, 1485-1498 (2008).

[2] X. Xuan, J. Zhu and C. Church Microfluid. Nanofluid. **9**, 1-16 (2010).

[3] C. C. Chang, Z. Y. Huang and R. J. Yang J. Micromech. Microeng. **17**, 1479-1486 (2007).

[4] C. G. Tsai, H. H. Hou and L. M. Fu Microfluid. Nanofluid. **5**, 827-836 (2008).

[5] J. Shi, X. Mao, D. Ahmed, A. Colletti and T. J. Huang Lab Chip **8**, 221-223 (2008).

[6] I. F. Cheng, H. C. Chang, D. Hou and H. C. Chang Biomicrofluid. **1**, 021503 (2007).

[7] L. Liang, J. Zhu and X. Xuan Biomicrofluid. **5**, 034110 (2011).

[8] Y. Zhao, B. S. Fujimoto, G. D. M. Jeffries, P. G. Schiro and D. T. Chiu Opt. Express **15**, 6167-6176 (2007).

[9] H. Ramachandraiah, S. Ardabili, A. M. Faridi, J. Gantelius, J. M. Kowalewski, G. Martensson and A. Russom, Biomicrofluid. **8**, 034117 (2014).

[10] A. M. Leshansky, A. Bransky, N. Korin and U. Dinnar Phys. Rev. Lett. **98**, 234501 (2007).

[11] S. Yang, J. Y. Kim, S. J. Lee, S. S. Lee and J. M. Kim Lab Chip **11**, 266-273 (2011).

[12] K. Kang, S. S. Lee, K. Hyun, S. J. Lee and J. M. Kim Nat. Comm. **4**, Article number: 2567. doi:10.1038/ncomms3567 (2013).

[13] E. J. Lim, T. Ober, J. F. Edd, S. P. Desai, D. Neal, K. W. Bong, P. S. Doyle, G. H. McKinley, M. Toner Nat. Comm. **5**, Article number: 4120. doi:10.1038/ncomms5120 (2014).

[14] S. Yan, J. Zhang, H. Chen, G. Alici, H. Du, Y. Zhu and W. Li Biomicrofluid. **8**, 064115 (2014).

[15] C. P. Jen and W. F. Chen Biomicrofluid. **5**, 044105 (2011).

[16] D. Li, Electrokinetics in microfluidics, Academic Press (2004).

[17] H. C. Chang and L. Y. Yeo Electrokinetically-Driven Microfluidics and Nanofluidics, Cambridge University Press (2009).

[18] L. M. Fu, R. J. Yang and G. B. Lee Anal. Chem. **75**, 1905-1910 (2003).

[19] H. A. Pohl Dielectrophoresis: The Behavior of Neutral Matter in Non-uniform Electric Fields, Cambridge University Press, Cambridge (1978).

[20] C. Church, J. Zhu, G. Huang, T. R. Tzeng and X. Xuan Biomicrofluid. **4**, 44101 (2010).

[21] X. Xuan, S. Raghibizadeh and D. Li, J. Colloid Interf. Sci. **296**, 743-748 (2006).

[22] C. Church, J. Zhu, G. Huang, T. R. Tzeng and X. Xuan Biomicrofluid. **3**, 044109 (2009).

[23] M. Li, S. B. Li, W. B. Cao, W. H. Li, W. J. Wen, G. Alici, J. Micromech. Microeng. **22**, 095001 (2012).

[24] Y. C. Lam,H. Y. Gan, N. T. Nguyen, and H. Lie, Biomicrofluidics **3**, 014106 (2009).

[25] K. E. Jensen, P. Szabo, F. Okkels, and M. A. Alves, Biomicrofluidics **6**, 044112 (2012).

[26] D. L. Lee, H. Brenner, J. R. Youn, Y. S. Song, Scientific Reports **3**, article number 3258. DOI: 10.1038/srep03258 (2013).

[27] P. C. Sousa, F. T. Pinho, M. S. N. Oliveira, and M. A. Alves, Biomicrofluidics **5**, 014108 (2011).

[28] Y. J. Kang and S. J. Lee, Biomicrofluidics **7**, 054122 (2013).

[29] C. J. Pipe and G. H. McKinley, Mech. Research Comm. **36**, 110-120 (2009).

[30] M. S. N. Oliveira, M. A. Alves and F. T. Pinho, Transport and Mixing in Laminar Flows: From Microfluidics to Oceanic Currents, 1st Edition. Ed. R. Grigoriev, Wiley-VCH (2012).

[31] C. L. A. Berli, Electrophoresis **34**, 622-630 (2013).

[32] C. Zhao and C. Yang, Adv. Colloid Interf. Sci. **201-202**, 94-108 (2013).

[33] S. Das and S. Chakraborty, Analytica Chim. Acta **559**, 15-24 (2006).

[34] S. Chakraborty, Analytica Chim. Acta **605**, 175-184 (2007).

[35] C. L. A. Berli and M. L. Olivares, J. Colloid Interf. Sci **320**, 582-589 (2008).

[36] C. Zhao, E. Zholkovskij, J. H. Masliyah, and C. Yang, J. Colloid Interf. Sci **326**, 503-510 (2008).

[37] A. M. Afonso, M.A. Alves, and F.T. Pinho, J. Non-Newtonian Fluid Mech. **159**, 50-63 (2009).

[38] S. Dhinakaran, A. M. Afonso, M. A. Alves, and F.T. Pinho, J. Colloid Interf. Sci **344**, 513-520 (2010).

[39] C. Zhao and C. Yang, Biomicrofluidics **5**, 014110 (2011).

[40] A. M. Afonso, F.T. Pinho, and M. A. Alves, J. Non-Newtonian Fluid Mech. **179-180**, 55-68 (2012).

[41] A. M. Afonso, M. A. Alves, and F. T. Pinho, J. Colloid Interf. Sci **395**, 277-286 (2013).

[42] E. Lee, Y. F. Huang, and J. P. Hsu, J. Colloid Interface Sci. **258**, 283-288 (2003).

[43] J. P. Hsu and L. H. Yeh, Langmuir **23**, 8637-8646 (2007).

[44] L. H. Yeh and J. P. Hsu, Microfluid. Nanofluid. **7**, 383-392 (2009).

[45] A. S. Khair, D. E. Posluszny, and L. M. Walker, Phys. Rev. E **85**, 016320 (2012).

[46] F. M. Chang and H. K. Tsao, Appl. Phys Lett. **90**, 194105 (2007).

[47] R. M. Bryce and M. R. Freeman, Phys. Rev. E **81**, 036328 (2010).

[48] R. M. Bryce and M. R. Freeman, Lab Chip 10, 1436-1441 (2010).

[49] X. Lu, S. Patel, M. Zhang, S. W. Joo, S. Qian, A. Ogale and X. Xuan Biomocrofluid. **8**, 021802 (2014).

[50] L. E. Rodd, T. P. Scott, D. V. Boger, J. J. Cooper-White and G. H. McKinley J. Non-Newtonian Fluid Mech. **129**, 1-22 (2005).

[51] J. Soulages, M. S. N. Oliveira, P. C. Sousa, M. A. Alves and G. H. McKinley J. Non-Newtonian Fluid Mech. **163**, 9-24 (2009).

[52] P. C. Sousa, F. T. Pinho, M. S. N. Oliveira and M. A. Alves J. Non-Newtonian Fluid Mech. **165**, 652-671 (2010).

[53] J. Y. Kim, S. W. Ahn, S. S. Lee and J. M. Kim Lab Chip **12**, 2807-2814 (2012).

[54] J. Nam, H. Lim, D. Kim, H. Jung and S. Shin Lab Chip 12, 1347-1354 (2012).

[55] K. W. Seo, Y. J. Kang and S. J. Lee Phys. Fluid. **26**, 063301 (2014).

[56] I. Ermolina and H. Morgan J. Colloid Interf. Sci. **285**, 419-428 (2005).

[57] J. Zhu, S. Sridharan, G. Hu and X. Xuan J. Micromech. Microeng. **22**, 075011 (2012).

[58] S. Sridharan, J. Zhu, G. Hu and X. Xuan Electrophoresis **32**, 2274-2281 (2011).

[59] I. Wong and C. M. Ho Microfluid. Nanofluid. **7**, 291-306 (2009).

[60] J. Zhu and X. Xuan Electrophoresis **30**, 2668-2675 (2009).

[61] A. M. Afonso, F.T. Pinho and M. A. Alves, J. Non-Newton. Fluid Mech. **179-180**, 55-68 (2012).

[62] A. Kale, X. Lu, S. Patel and X. Xuan J. Micromech. Microeng. **24**, 075007 (2014).

[63] R. Pethig, Biomicrofluid. **4**, 022811 (2010).

[64] S. Senapati, A. R. Mahon, J. Gordon, C. Nowak S. Sengupta, T. H. Q. Powell, J. Feder, D. M. Lodge and H. C. Chang, Biomicrofluid. **3**, 022407 (2009).

[65] I. F. Cheng, S. C. Chiang, C. C. Chung, T. M. Yeh and H. C. Chang, Biomicrofluid. **8**, 061102 (2014).

CHAPTER FOUR

VISCOELASTIC EFFECTS ON ELECTROOSMOTIC FLOW IN A CONSTRICTION MICROCHANNLE

Abstract

The viscoelastic effects have been little studied in electrokinetic flow experimentally. Thus it is critical to unveil the details of electroosmosis in viscoelastic fluid. Flow visualization is an important tool in experimental fluid mechanics. By tracking the small particles in the fluid, the flow field can be captured. In the present paper, the flow visualization study of electrokinetic flow shows significant difference in Newtonian and viscoelastic fluids through a constriction microchannel. The deflected particle trajectories are observed near the constriction entrance at the upstream of the fluid in viscoelastic fluid. They are asymmetric along the centerline and grow with the electric field. A numerical work is also presented, which predicts smaller velocity in the middle area of the channel and hence smaller flow rate in Oldroyd-B model as compared with the Newtonian one.

4.1 Introduction

The unexpected particle electrokinetic motions in the viscoelastic fluids have been reported in our previous papers.[1,2] For a better understanding of the electrokinetic flow in viscoelastic fluid, the flow field study is highly needed. Most of previous flow visualization articles of non-Newtonian fluid are focused on pressure driven flow. There

are a great number of experimental investigations dealing with the flow patterns in planar constriction channel in polymer solutions. Rothstein et al.[3,4] presented visualized unstable streamlines and vortices at the upstream in PEO solutions. The vortices grew with polymer concentration and flow rate, i.e., the Weissenberg number. On the contrary, vortex at the downstream was generated more easily in Newtonian fluid than in non-Newtonian solution, because the elastic effect impeded the inertial effect which contributed the downstream vortex growth. Furthermore, Rodd's work[5] referred to a time dependent experimental phenomenon. When the Weissenberg number reached to a critical value, unstable and time dependent flow pattern appeared immediately. In addition, several researchers[3,6-8] observed varied flow patterns in channels of different constriction ratio and curvature to the reentrant corner.

However, very few flow visualization works have been reported in electroosmosis of viscoelastic fluid. The only experimental work was from Bryce and Freeman,[9,10] who showed that the flow streams of mixing were unstable in the PAA solution through a 2:1 microchannel constriction experimentally. Afonso[11] demonstrated the elastic flow instabilities in the numerical model of electroosmosis in viscoelastic fluids. Park and Lee's work[12] achieved smaller flow rate of viscoelastic electroosmotic flow as compared with that of Newtonian flow under same electric field by a general constitutive equation. In this paper, we present experimental and numerical studies of the flow field in viscoelastic fluid. To visualize the flow field, small fluorescent polystyrene particles were added to the solution. Due to the electrochemical nature, the particles are always electrical charged in the fluid. The small particle motion we captured was considered as a

superposition of electroosmosis (EO), electrophoresis (EP) and dielectrophoresis (DEP). Even though the instinctive drawback exists, we are able to study the flow flied (EO) from the particle motion, because the EP and DEP are independent in flow field. The abnormal particle trajectories were observed in experiment, which indicated the deformed flow streamlines. But our numerical result failed to predict the deflected particle trajectories. Velocity decrease in the middle of the channel was found in Oldroyd-B model as compared to Newtonian one.

4.2 Experiment

4.2.1 Preparation and technique of experiment

The 40 μm-deep microchannel is overall 1 cm-long and 400 μm-wide with a constriction of 200 μm length and 40 μm width in the middle. Detailed soft lithography method of fabrication is referred to Lu et al.[1] The 500 ppm polyethylene oxide (PEO) solution was prepared by by dissolving PEO powder (Sigma-Aldrich, average molecular weight $M_w = 4\times10^6$ Da) into 1 mM phosphate buffer. The viscosity is 2.0 mPa·s and the relaxation time is estimated as 18ms.[1] The polystyrene spheres of 0.53 μm and 1.01 μm (Bangs lab) in diameter were suspended in the PEO solution to a final concentration of about 10^6 particles per milliliter. To illustrate the viscoelastic effects, the particles were also re-suspended in the base fluid, i.e., 1 mM pure buffer, which is a Newtonian fluid, for a direct comparison. A small amount of Tween 20 (0.5% in volume ratio, Fisher Scientific) was added to both the Newtonian and non-Newtonian particle suspensions for the purpose of suppressing particle-wall and particle-particle adhesions.

The same experimental setup and visualization methods are referred to Lu et al.[1] Fluorescent light was used in order to visualize the fluorescent particles. The exposure time was 100 ms. The superimposed particle images were obtained by stacking a sequence of around 10 and 40 snapshot images with the maximum intensity projections for the 1.01 μm and 0.53 μm fluorescent particles respectively.

4.2.2 Electrokinetic mobility and dimensionless number

The measured electrokinetic mobility is -1.6×10^{-8} $m^2/(V\cdot s)$ and -2.5×10^{-8} $m^2/(V\cdot s)$ in the Newtonian buffer solution and the 500 ppm PEO solution, respectively. By the estimation of wall zeta potential as -80 mV and -20 mV in the Newtonian and PEO solutions, the zeta potential of particles is -100mV and -55mV in the Newtonian and PEO solutions, respectively. The electroosmotic and electrophoretic velocities are comparable and in the same order of magnitude. The Weissenberg number is defined as the ratio of effective relaxation time and the average shear rate, $\dot{\gamma}$,

$$Wi = \lambda_e \dot{\gamma} = \lambda_e \frac{V_p}{w/2} \quad (1)$$

in which λ_e is the effective relaxation times, V_p is the particle velocity at the constriction, w and h are the width and height of the channel constriction. Reynolds number is defined as the ratio of the inertial force to the viscous force,

$$Re = \frac{\rho V_p D_h}{\mu} \quad (2)$$

where ρ is the density, μ is the fluid dynamic viscosity, and D_h is the hydraulic diameter.

4.3 Mathematical model and numerical method

The same top-view geometry of the constriction microchannel is used in the 2D model, except that the total length is 2 mm-long to save computational time. The electroosmotic flow in viscoelastic fluid is investigated using the direct numerical simulation (DNS) method. The electric field is governed by the Laplace equation,

$$\nabla^2 \Phi = 0 \tag{3}$$

where Φ is the electric potential. The electric potentials applied on the inlet and outlet are Φ_0 and 0, respectively. The channel walls are electrically insulating,

$$\mathbf{n} \cdot \nabla \Phi = 0 \tag{4}$$

The incompressible viscoelastic flow is governed by continuity and Navier-Stokes equations,

$$\nabla \cdot \mathbf{u} = 0 \tag{5}$$

$$\rho \left(\frac{\partial \mathbf{u}}{\partial t} + \mathbf{u} \cdot \nabla \mathbf{u} \right) = \nabla \cdot \boldsymbol{\sigma} \tag{6}$$

$$\boldsymbol{\sigma} = -p\mathbf{I} + 2\mu_s \mathbf{D} + \boldsymbol{\tau} \tag{7}$$

where $\mathbf{D} = [\nabla \mathbf{u} + (\nabla \mathbf{u})^{\mathrm{T}}]/2$ is rate-of-deformation tensor, $\mathbf{I}$ is the unit tensor, and μ_s is the solvent viscosity. The symmetric $\boldsymbol{\tau}$ is extra stress contribution owing to the polymer, which is written in terms of the conformation tensor $\mathbf{c}$

$$\boldsymbol{\tau} = \frac{\mu_p}{\lambda} (\mathbf{c} - \mathbf{I}) \tag{8}$$

where μ_p is the polymer viscosity and λ is the polymer relaxation time. The fluid dynamic viscosity $\mu = \mu_p + \mu_s$. With constant viscosity, the Oldroyd-B (OB) constitutive equation is used to describe the transport of polymer stress in the flow:

$$\lambda \overset{\nabla}{\mathbf{c}} + \mathbf{c} - \mathbf{I} = 0 \tag{9}$$

where $\overset{\nabla}{\mathbf{c}}$ is the upper convected derivative

$$\overset{\nabla}{\mathbf{c}} = \frac{\partial \mathbf{c}}{\partial t} + \mathbf{u} \bullet \nabla \mathbf{c} - \left[(\nabla \mathbf{u}) \cdot \mathbf{c} + \mathbf{c} \cdot (\nabla \mathbf{u})^{\mathrm{T}} \right] \tag{10}$$

Smoluchowski slip velocity boundary conditions are imposed on the rigid walls,

$$\mathbf{u} = -\varepsilon \varepsilon_0 \zeta_w \mathbf{E} / \mu \tag{11}$$

where ε and ε_0 are the relative and vacuum permittivity, ζ_w is the zeta potential of channel wall, and $\mathbf{E}$ is the electric field. $p\mathbf{n} = \mathbf{0}$ is imposed on inlet and outlet. Dimensionless governing equations are respectively

$$\nabla'^2 \Phi' = 0 \tag{12}$$

$$\nabla' \cdot \mathbf{u}' = 0 \tag{13}$$

$$Re_m \left(\frac{\partial \mathbf{u}'}{\partial t'} + \mathbf{u}' \cdot \nabla' \mathbf{u}' \right) = \nabla' \cdot \boldsymbol{\sigma}' \tag{14}$$

$$Wi_m \overset{\nabla}{\mathbf{c}}' + \mathbf{c}' - \mathbf{I} + \alpha (\mathbf{c}' - \mathbf{I})^2 = 0 \tag{15}$$

where $Re_m = \rho U_0 w / \mu$, $Wi_m = \frac{\lambda U_0}{w}$, $\mu_s' = \mu_s / \mu$, $\mu_p' = \mu_p / \mu$, U_0 and w are the characteristic velocity and length respectively. $U_0 = \varepsilon \varepsilon_0 \zeta_p \Phi_0 / (\mu w)$, where Φ_0 is the characteristic potential and ζ_w is the zeta potential of particle. Hereinafter, the dimensionless variables in equations are written without apostrophe.

Due to the difficulty in numerical convergence at relatively high *Wi*, the constitutive equation is transformed to equivalent equations in terms of log conformation tensor **s**, which is defined as

$$\mathbf{s} = log(\mathbf{c}) \tag{16}$$

To decomposition of the velocity gradient into extensional and rotational components, a matrix decomposition, which is approved by Fattal and Kupferman,[13] is used the OB constitutive equation,

$$\nabla \mathbf{u} = \boldsymbol{\Omega} + \mathbf{B} + \mathbf{N}\mathbf{c}^{-1} \tag{17}$$

where $\boldsymbol{\Omega}$ and $\mathbf{N}$ are anti-symmetric (pure rotations) and $\mathbf{B}$ is symmetric, traceless and commutes with $\mathbf{c}$. Based on their matrix decomposition theorem, the diagonalizing transformation

$$\mathbf{s} = \mathbf{R}\begin{pmatrix}\lambda_1 & 0\\ 0 & \lambda_2\end{pmatrix}\mathbf{R}^{\mathrm{T}} \tag{18}$$

where λ_1 and λ_2 are the eigenvalues of $\mathbf{s}$, and $\mathbf{R} = [\mathbf{X}_1 \vdots \mathbf{X}_2]$, where $\mathbf{X}_1$ and $\mathbf{X}_2$ are the eigenvectors of $\mathbf{s}$ and $\|\mathbf{X}_1\| = \|\mathbf{X}_2\| = 1$. Thus

$$\mathbf{c} = \mathbf{R}\begin{pmatrix}e^{\lambda_1} & 0\\ 0 & e^{\lambda_2}\end{pmatrix}\mathbf{R}^{\mathrm{T}} \tag{19}$$

Set

$$\begin{pmatrix}\tilde{m}_{11} & \tilde{m}_{12}\\ \tilde{m}_{21} & \tilde{m}_{22}\end{pmatrix} = \mathbf{R}^{\mathrm{T}}(\nabla \mathbf{u})\mathbf{R} \tag{20}$$

Then,

$$\mathbf{N} = \mathbf{R}\begin{pmatrix}0 & \tilde{n}\\ -\tilde{n} & 0\end{pmatrix}\mathbf{R}^{\mathrm{T}},\ \mathbf{B} = \mathbf{R}\begin{pmatrix}\tilde{m}_{11} & 0\\ 0 & \tilde{m}_{22}\end{pmatrix}\mathbf{R}^{\mathrm{T}},\ \boldsymbol{\Omega} = \mathbf{R}\begin{pmatrix}0 & \tilde{\omega}\\ -\tilde{\omega} & 0\end{pmatrix}\mathbf{R}^{\mathrm{T}} \tag{21}$$

where $\tilde{n} = (\tilde{m}_{12} + \tilde{m}_{21})/(e^{-\lambda_1} + e^{-\lambda_2})$, $\tilde{\omega} = (e^{\lambda_1}\tilde{m}_{21} + e^{\lambda_2}\tilde{m}_{12})/(e^{\lambda_2} - e^{\lambda_1})$.

Therefore, eq. 15 is transformed to

$$Wi_m\left(\frac{\partial \mathbf{s}}{\partial t} + \mathbf{u}\cdot\nabla\mathbf{s} - (\boldsymbol{\Omega}\mathbf{s} - \mathbf{s}\boldsymbol{\Omega}) - 2\mathbf{B}\right) + \mathbf{I} - inv(e^{\mathbf{s}}) + \alpha\, inv(e^{\mathbf{s}})(e^{\mathbf{s}} - \mathbf{I})^2 = 0 \tag{22}$$

This log-conformation method is to overcome a stability/stiffness problem associated with the balance between stress advection and stress amplification, and to guarantee positive definiteness of the recovered conformation tensor.[14,15]

The particle transport was simulated by Lagrangian particle tracking method[16] in COMSOL 4.4. The particle-particle and particle-fluid interactions were neglected due to small particle size. The dimensionless particle velocity is given by

$$\mathbf{U}_p = \mathbf{u} + \mathbf{E} + \mu_{DEP}/\mu_{EP}(\mathbf{E} \cdot \boldsymbol{\nabla}\mathbf{E}) \qquad (23)$$

where $\mu_{EP} = \varepsilon\varepsilon_0\zeta_p/\mu$, $\mu_{DEP} = \varepsilon d^2 f_{CM}/6\mu$ and the particle diameter d. The Clausius-Mossotti (CM) factor $f_{CM} = (\sigma_p - \sigma_f)/(\sigma_p + 2\sigma_f)$. The electric conductivity of particles $\sigma_p = 4 \times 10^{-9}[s]/d$ and the electric conductivity of fluid σ_f is 200 $\mu S/cm$.

4.4 Results and discussion

Fig. 1(a) shows the results of particle trajectories in the Newtonian solution. The fluid flows from top to bottom while the particles move in the opposite direction. The DEP effect is very weak in a large range of electric field since the small particles are barely focused after passing through the constriction. The particle velocity can be considered as a liner superposition of flow velocity (EO), EP and DEP velocities, of which the EP and DEP components are only dependent on the electric field and not affected by flow field. The particle trajectory can reflect the streamlines of flow field. Therefore, if there is any abnormal particle trajectory, it is the contribution of flow field only. In fig.1 (a), the particle trajectories appear similar in a large range of flow field. Particles flow through the constriction smoothly. The particles get slightly focused at the

upstream due to the weak DEP effect. These results of Newtonian fluid agree with previous work.[17]

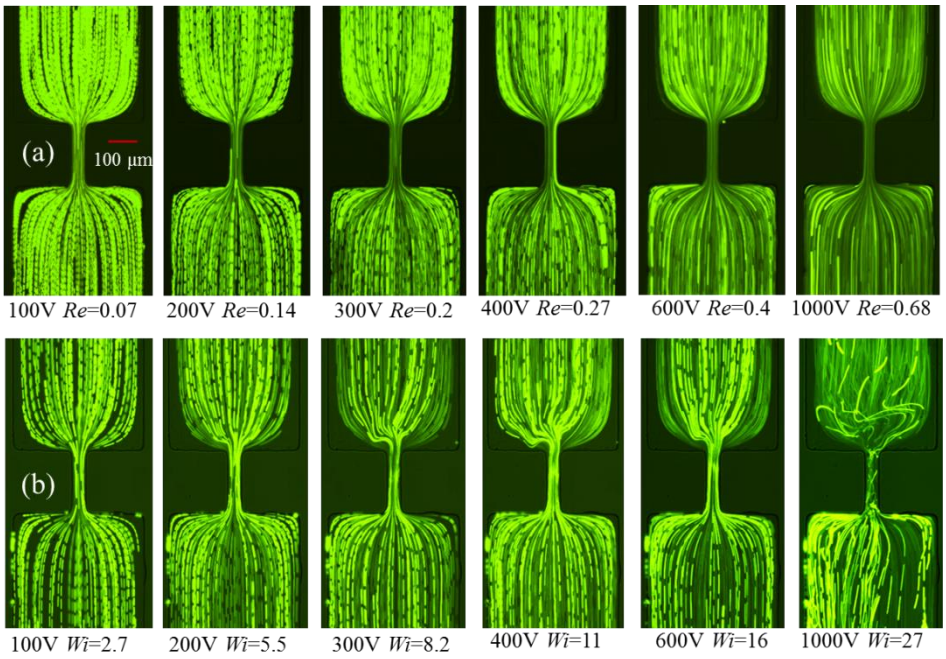

Fig. 1. Particle trajectories of 1.01 μm particles in Newtonian solution (a) and PEO solution (b) at different voltages. The electroosmotic direction is from top to bottom and the electrokinetic particle motion is in the opposite direction.

However, the particle trajectories in PEO solution are distinctly different from the Newtonian case in large range of electric field as shown in fig. 1(b). The trajectories look similar with the Newtonian one at 100V, but they are slightly deformed and asymmetric along the centerline at the constriction entrance in the upstream of the fluid at 200V. The deformation of trajectories becomes larger at 300V and grows with rising electric field. At 1000V, the particle streams show chaotic pattern. To observe the chaotic pattern more clearly, two snapshot images are introduced in fig. 2(a). The deformations do not only exist at the entrance of constriction, but also extend towards the upstream which are about 100 μm above the constriction. The curved streamlines are unstable and time

dependent. In fig. 2 (b), the results of 0.53 μm particles at the same conditions are provided, in which the curved streamlines are comparable with the 1.01 μm particles. This demonstrates the size-independence of small particles. We believe that the extensional viscoelastic instability is the source of this electroosmotic perturbation. The extensional instability was also reported by Bryce and Freeman[7,8] experimentally. The instability exists primarily at the upstream and grows with electric field/electroosmotic speed.

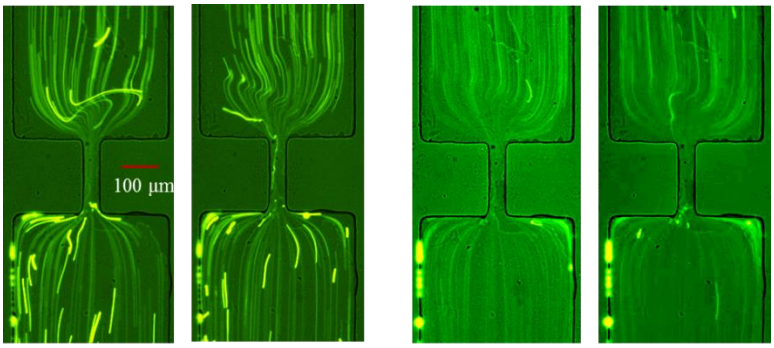

Fig. 2. Snapshot images of 1.01 μm (a) and 0.53 μm (b) particles in PEO solution at 1000V.

In our previous works,[1,2] the viscoelastic electrokinetic motion of large particles is more complicated than the present one of small particles, because the DEP effect is strong and the particle-fluid interaction of large particles significantly affects the electroosmosis. Although we are still not able to determine the mechanism of the electrokinetic particle motion by this flow visualization study, the viscoelastic effect is proved to influence the electroosmosis, which affects the electrokinetic particle motion.

Fig. 3 shows the numerical results in the Newtonian (a) and OB (b) models. The background color shows the normalized velocity magnitude, V/V_c, where V_c is the slip

velocity in the wide channel. The particle trajectories are plotted, which are similar with the streamlines of flow field in Fig. 1 (a). In the result of OB model (b) with Wi_m=46, corresponding to Wi=10 in experiment, no deformed streamlines are observed. The 2D OB model fails to predict the disturbed particle trajectories in experiment. Fig. 3 (c) shows that the differences between the Newtonian and OB models are the velocity magnitude in the middle area of the channel. The velocities predicted by the OB model are always smaller than those in the Newtonian model. The viscoelastic effect decreases the flow velocity and flow rate in electroosmosis, which agrees with Park and Lee's work.[12]

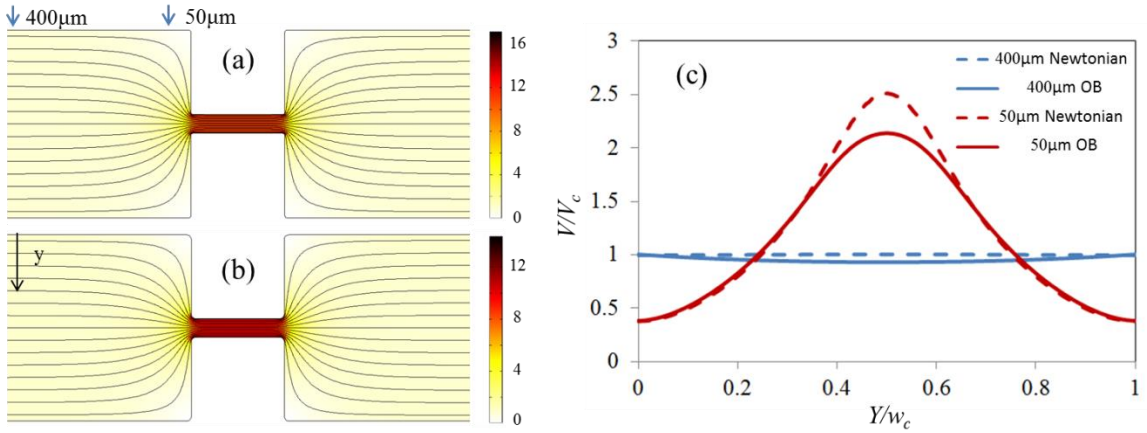

Fig. 3. Flow fields of Newtonian model (a) and OB model (b) with Wi_m=46, corresponding to Wi=10 in experiment. The background color shows the normalized velocity magnitude (V/V_c, where V_c is the slip velocity in the wide channel). The black lines indicate the particle trajectories. The velocity magnitudes are plotted in (c) for Newtonian model (dash lines) and OB model (solid lines) along the normalized lateral (y) direction at the places which are 50 μm and 400 μm away from the constriction at the upstream (indicated by the arrows in (a))

4.5 Conclusion

We have studied the flow visualization of electrokinetic flow in viscoelastic fluid through a constriction microchannel. It is shown that the electrokinetic particle

trajectories, which represent the electroosmotic flow streamlines, are significantly different between Newtonian and viscoelastic fluids. The deflected particle trajectories are observed near the constriction entrance at the upstream of the fluid. They are asymmetric along the centerline and grow with the electric field. At the high electric field, the deformation of particle trajectories extends towards upstream and become time dependent. The numerical result of Oldroyd-B model is presented at comparable *Wi* number. But it fails to predict the deflected particle trajectories. Instead, the velocity in the middle area of the channel, and hence the flow rate, in OB model is found smaller than the Newtonian one.

References

[1] X. Lu, S. Patel, M. Zhang, S.W. Joo, S. Qian, A. Ogale, and X. Xuan, Biomicrofluidics **8**, 021802 (2014).

[2] X. Lu, J. DuBose, S. W. Joo, S. Qian, and X. Xuan, Biomicrofluidics **9**, 014108 (2015).

[3] J. P. Rothstein and G. H. Mckinley, J. Non-Newtonian Fluid Mech. **98**, 33-63 (2001).

[4] L. E. Rodd, T. P. Scott, D. V. Boger, J. J. Cooper-White, and G. H. McKinley, J. Non-Newtonian Fluid Mech. **129**, 1–22 (2005).

[5] L. E. Rodd, J. J. Cooper-White, D. V. Boger, and G. H. McKinley, J. Non-Newtonian Fluid Mech. **143**, 170-191 (2007).

[6] D. V. Boger, Annu. Rev. Fluid Mech. **19**, 157–182 (1987).

[7] S. A. White, A. D. Gotsis, and D. G. Baird, J. Non-Newtonian Fluid Mech. **24**, 121–160 (1987).

[8] D. V. Boger and R. J. Binnington, J. Rheol. **38**, 333–349 (1994).

[9] R. M. Bryce and M. R. Freeman, Phys. Rev. E **81**, 036328 (2010).

[10] R. M. Bryce and M. R. Freeman, Lab Chip **10**, 1436-1441 (2010).

[11] A. M. Afonso, F.T. Pinho, and M. A. Alves, J. Non-Newtonian Fluid Mech. **179**, 55-68 (2012).

[12] H. M. Park and W. M. Lee, Lab on a Chip **8**, 1163-1170 (2008).

[13] R. Fattal and R. Kupferman, J. Non-Newtonian Fluid Mech. **123**, 281-5 (2004).

[14] R. Guénette, A. Fortin, A. Kane, and J. F. Hétu, J. Non-Newtonian Fluid Mech. **153,** 34-45 (2008).
[15] A. M. Afonso, P. J. Oliveira, F. T. Pinho, and M. A. Alves, Journal of Fluid Mech. **677**, 272-304 (2011).
[16] K.H., Kang, X., Xuan, Y. Kang, and D., Li, Journal of Applied Physics **99**(6), 064702 (2006).
[17] J. Zhu and X. Xuan, Electrophoresis **30**(15), 2668-2675 (2009).

CHAPTER FIVE

CONTINUOUS MICROFLUIDIC PARTICLE SEPARATION VIA ELASTO-INERTIAL PINCHED FLOW FRACTIONATION (eiPFF)

Abstract

Many of the fluids encountered in chemical and biomedical applications exhibit non-Newtonian behavior. However, the majority of current particle separation methods have been demonstrated in Newtonian fluids only. This work presents an experimental study of continuous particle separation in viscoelastic solutions via a combined action of elastic and inertial lift forces, which we term elasto-inertial pinched flow fractionation (eiPFF). The parametric effects on eiPFF are systematically investigated in terms of dimensionless numbers. It is found that eiPFF offers much higher particle throughput and separation resolution than the traditional steric effects-based PFF. Moreover, eiPFF works most efficiently when the Reynolds number, *Re*, is of order 1, and hence fills perfectly into the gap of our recently proposed inertia-enhanced PFF (iPFF) technique (*Anal. Chem.* **2015**, *87*, 4560-4565) that favors *Re* of order 10 or more. However, the particle separation via eiPFF does not increase monotonically with the elasticity number at higher polymer concentrations and is strongly affected by the aspect ratio of channel width to height, both of which have not been previously reported. More surprisingly, the elasto-inertial deflection of small particles can be even greater than that of large particles in a high-aspect-ratio channel for *Re* less than 1.

5.1 Introduction

In the past two decades microfluidic devices have become an attractive platform for many chemical and biomedical applications due to their enhanced efficiency and accuracy at a reduced cost.[1] Separating target particles (synthetic or biological) from a mixture in a continuous label-free manner is often a necessary step in these lab-on-a-chip applications.[2] It can be implemented based on the differences in intrinsic particle properties such as size, shape or deformability through either an externally imposed or an internally induced force field.[3] The former type of *active* separation methods has been achieved by the use of electric,[4] optical,[5] acoustic,[6] or magnetic[7] field-induced cross-stream phoretic motions. Additionally, a variety of *passive* separation methods have been developed which exploit the confinement-induced electric or hydrodynamic force to manipulate particles toward differential equilibrium positions.[8] This type of approaches covers insulator-based dielectrophoresis (iDEP),[9] deterministic lateral displacement (DLD),[10] hydrodynamic filtration,[11] hydrophoresis,[12] split-flow thin-cell fractionation (SPLITT),[13] pinched flow fractionation (PFF),[14] and inertial microfluidics[15] etc. However, all these continuous particle separation methods have thus far been demonstrated in Newtonian fluids only.

As a matter of fact, many of the fluids that are encountered in practical microfluidic applications like polymeric solutions and bodily fluids (e.g., blood and saliva) are complex, and can exhibit strong non-Newtonian behaviors such as shear thinning and viscoelasticity.[16-18] Early studies of particle motion in non-Newtonian fluids can be dated back to half a century ago,[19-20] which are mostly concerned with the particle sedimentation in a stationary fluid[21] or the particle migration in a pipe flow.[22] In the

former situation, anomalous particle motion has been reported such as velocity overshoot, oscillation and even reversal[23] due to the evolution of a negative wake.[24] For particles in viscoelastic pipe/slit flows, inward migration to the centerline has been experimentally observed,[25-27] which, as explored both theoretically[28] and numerically,[29,30] arises from the normal stress difference in the fluid. However, the effect of shear thinning can cause particles to migrate away from the centerline at increased flow rates.[31,32]

Recent studies of particle motion in non-Newtonian fluids have been shifted to rectangular microchannels that are easily available with state-of-the-art micro-fabrication techniques.[33] The involving flows are three-dimensional, wherein particles have been demonstrated to migrate toward multiple equilibrium positions including the centerline and the four corners.[34,35] This cross-stream particle migration to the regions of low shear rate is again a result of the normal stress difference in a viscoelastic fluid. The equilibrium positions can be reduced to only one along the channel centerline by the combined action of elastic and inertial effects,[36] which, however, is still strongly influenced by the fluid rheology.[37,38] Such a three-dimensional focusing effect has been demonstrated for a variety of (bio)particles, and can remain effective at extremely high flow rates in a hyaluronic acid-based weakly elastic fluid.[39] It has also been utilized to selectively enrich and filter the larger particles from a particle mixture.[40] In addition, similar single-line particle focusing has been observed in viscoelastic flows through both a rectangular microchannel with side-wells[41] and a spiral microchannel.[42]

Besides aligning particles in planar microchannels for detecting and analyzing purposes,[43,44] the cross-stream particle migration in viscoelastic flows has also been

demonstrated to separate particles in few recent studies. Yang et al.[45] reported that fresh red blood cells in a polyvinylpyrrolidone (PVP)-based phosphate buffered saline (PBS) solution can be directed toward the centerline of a straight square microchannel by the cell deformability-induced lift.[46] In contrast, rigidified red blood cells are mostly entrained along the corners due to the fluid viscoelasticity-induced lift under negligible inertia. The authors further utilized this phenomenon to isolate white blood cells (which are more rigid than red blood cells) from dilute whole blood with a high enrichment ratio.[45] Nam et al.[47] developed a simple method that exploits the particle size-dependence of elastic and inertial lift forces in viscoelastic fluids to continuously separate large particles from a sheath flow-focused particle mixture solution near the walls. This method was demonstrated to sort platelets from dilute whole blood in a polyethylene oxide (PEO)-based PBS solution with a purity of close to 99.9%. A similar idea was later employed by Kang et al.[26] to implement a continuous separation of multiple polystyrene particles in an extremely dilute DNA solution.

The continuous particle separation method developed by Nam et al.[47] is similar to PFF[14] in configuration and depends on the combined action of elastic and inertial lift forces in a viscoelastic fluid, so we term it elasto-inertial pinched flow fractionation (eiPFF). As compared to inertial microfluidics,[15,48] eiPFF is able to separate much smaller particles such as 1-2 μm in diameter[26] and can even potentially separate submicron particles[34] though at a smaller throughput. Moreover, it has the capability of separating complex samples (e.g.. quaternary mixture of particles[26]) and works for biological cells via the use of biocompatible polymer solutions (e.g., PVP[45] and hyaluronic acid[39]). Since

a direct numerical simulation of particle motion in viscoelastic fluids is currently still very challenging, this work presents a systematic experimental study of the parametric effects on continuous particle separation via eiPFF. The aim is to acquire a comprehensive understanding of the important factor(s) that may impact eiPFF and provide a useful guidance for future design and control of this novel microfluidic separation technique.

5.2 Experiment

5.2.1 Preparation of particle suspensions

3.1 μm- and 9.9 μm-diameter (referred to hereafter as 3 μm and 10 μm for brevity) polystyrene spheres (Thermo Scientific) were used in the separation experiments. They were mixed at an approximately 2:1 number density ratio and re-suspended in aqueous Newtonian and non-Newtonian fluids to a final concentration of about 10^7 particles per milliliter. The Newtonian fluid was prepared by mixing 21 wt.% glycerol (Fisher Scientific) with water (Fisher Scientific) to match the mass density of polystyrene particles (1.05 g/cm^3).[49] The non-Newtonian fluids were prepared by dissolving PEO powder (Sigma-Aldrich USA, molecular weight $M_w = 2\times10^6$ Da) into the glycerol (21 wt.%)/water solution at the concentrations of 500 ppm, 1000 ppm, and 2000 ppm, respectively. The properties of the prepared Newtonian and non-Newtonian fluids at 20 °C (the operation temperature of all experiments) are summarized in Table 1. The process for determining the relaxation times are provided in the Supporting Information (Appendix A).

Table 1. Properties of the 21 wt.% glycerol/water-based Newtonian and non-Newtonian fluids used in experiments.

Fluid properties (at 20 °C)	**Newtonian**	**Non-Newtonian** (*c*, ppm PEO)		
		500	1000	2000
Density ρ (g/cm^3)	1.05	1.05	1.05	1.05
Zero-shear viscosity η_0 (mPa·s)	1.8	2.8	4.0	10.6
Overlap concentration c^* (ppm)		858	858	858
Concentration ratio c/c^*		0.58	1.17	2.33
Zimm relaxation time, λ_{Zimm} (ms)		0.6	0.6	0.6
Effective relaxation time, λ_e (ms)		7.9	12.4	19.5

5.2.2 Experimental setup

Figure 1 shows a picture of the asymmetric T-shaped microchannel used in experiments, which was fabricated in polydimethylsiloxane (PDMS) using the standard soft lithography method.[50] The channel has a 2 cm-long main-branch and two 4 mm-long side-branches with a uniform width of 50 μm. There is a 900-μm wide, 2 mm-long expansion at the end of the main-branch for enhancing and visualizing the particle separation. Three depths of channels were used for the purpose of examining the effect of channel aspect ratio on particle separation, which are 25, 40 and 100 μm, respectively. The prepared sheath fluid (i.e., the pure suspending medium of the particle mixture) and particle mixture were each pumped through the T-shaped microchannel (see Figure 1) by an infusion syringe pump (sheath fluid, KDS-100 from KD Scientific; particle suspension, NE-300 from New Era Pump Systems, Inc.). Particle motion was visualized at the T-junction and the channel expansion (highlighted by the dashed-box in Figure 1) through an inverted microscope (Nikon Eclipse TE2000U) with a CCD camera (Nikon

DS-Qi1Mc). They were post-processed using the Nikon imaging software (NIS-Elements AR 3.22).

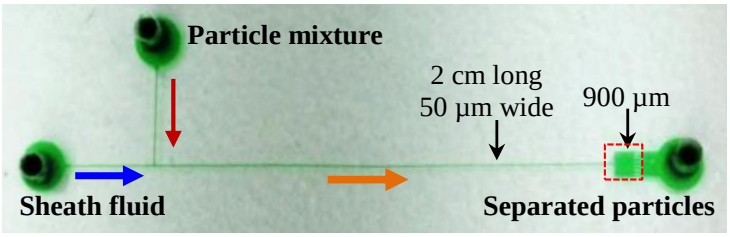

Figure 1. Top-view picture of the asymmetric T-shaped microchannel (filled with green food dye for clarity) used in experiments. The block arrows indicate the flow directions of the sheath fluid (which is the pure suspending medium of the particle mixture) and particle mixture for particle separation, which is visualized at the 900 µm-wide expansion region at the end of the 2 cm-long, 50 µm-wide main-branch (highlighted by a dashed-box highlights).

5.3 Theoretical

5.3.1 Dimensionless numbers

The dynamics of particle motion in non-Newtonian fluids through microchannels is often characterized by the following dimensionless numbers:[15,33,48] Reynolds number, Weissenberg number and elasticity number. The Reynolds number, *Re*, is defined as the ratio of the inertial force to the viscous force,

$$Re = \frac{\rho V D_h}{\eta_0} = \frac{2\rho Q}{\eta_0 (w+h)} \quad (1)$$

where V is the average fluid velocity in the main-branch of the T-shaped microchannel (see Figure 1), $D_h = 2wh/(w+h)$ is the hydraulic diameter with w and h being the width and height of the main-branch, and Q is the volumetric flow rate through the main-

branch. The Weissenberg number, *Wi*, measures the fluid elasticity effects and is defined in terms of the average shear rate, $\dot{\gamma}$, in the main-branch,

$$Wi = \lambda_e \dot{\gamma} = \lambda_e \frac{2V}{w} = \frac{2\lambda_e Q}{w^2 h} \quad (2)$$

The elasticity number, *El*, is defined as the ratio of fluid elasticity to inertia, which is independent of the flow kinematics,

$$El = \frac{Wi}{Re} = \frac{\lambda_e \eta_0 (w+h)}{\rho w^2 h} \quad (3)$$

Two other dimensionless numbers are also used in this work to study the parametric effects on particle separation via eiPFF. One is the flow rate ratio between the sheath fluid and particle mixture, α, in the two side-branches of the T-shaped microchannel, which measures the sheath flow focusing performance in the main-branch and affects the particle deflection and dispersion at the channel expansion,

$$\alpha = \frac{Q_{sheath}}{Q_{particle}} \quad (4)$$

Note that the definitions of *Re* and *Wi* in eq 1 and eq 2, respectively, are both based on the total flow rate in the main-branch of the microchannel, i.e., $Q = Q_{sheath} + Q_{particle}$. The other dimensionless number is the channel aspect ratio, *AR*, as mentioned in the Experimental section,

$$AR = w/h \quad (5)$$

which has been demonstrated to affect the equilibrium position(s) of particles in inertial microfluidics with Newtonian fluids.[15,48]

5.3.2 Mechanism of eiPFF

In traditional PFF,[14] particles of different sizes must first be aligned against one sidewall of the pinched branch (i.e., the main-branch of the T-shaped microchannel in Figure 1) by a strong sheath flow. This forces the centers of the particles to locate at different streamlines due to steric effects,[14,51] i.e., the center of larger particles stays further away from the wall than that of smaller ones. Subsequently, the spreading laminar flow profile at the exit of the pinched branch (i.e., the expansion of the main-branch in Figure 1) yields a continuous separation of particles based on size. For a theoretically complete separation via PFF, the maximum allowed width of the sheath flow-focused particulate solution in the main-branch, $w_{p,max}$, must fulfill (see the clarification in the Supporting Information),[52]

$$w_{p,max} = r_{p1} + r_{p2} \tag{6}$$

where r_{p1} and r_{p2} are the radii of the two types of particles to be separated. This $w_{p,max}$ corresponds to the limiting situation for which the larger particles share the same center position as those smaller particles that are most distant from the wall. Since its first introduction,[14] PFF has been improved by either reducing the particle dispersion[53] via an enhanced sheath flow focusing[54] or increasing the particle displacement via an extra force field (e.g., electrical lift,[55] inertial lift,[56] optical force[57] and gravity[58]).

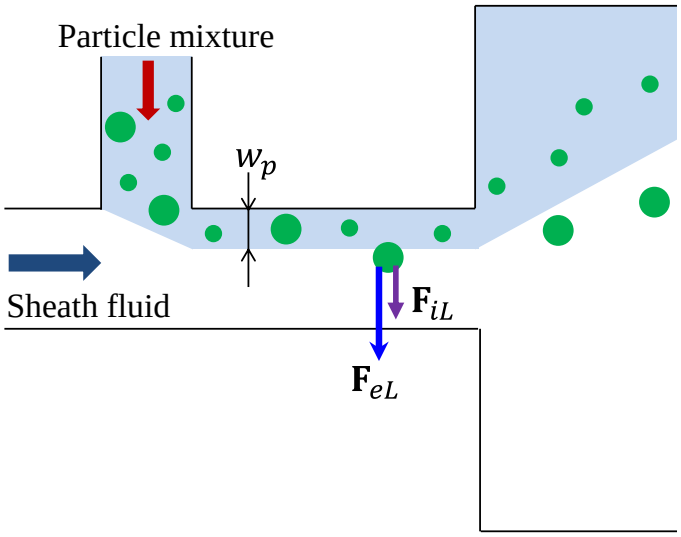

Figure 2. Schematic illustration (not to scale) of the mechanism for eiPFF. The sheath-fluid focused particle-mixture solution (highlighted by the background color) has a width of w_p in the main-branch, which for traditional PFF should be smaller than the maximum allowed width, $w_{p,max}$, given in eq 6. In eiPFF, this constraint is released because the elastic lift force, $\mathbf{F}_{eL}$, and inertial lift force, $\mathbf{F}_{iL}$, induced in a viscoelastic fluid act together to deflect particles toward the channel center at a size-dependent rate.

In contrast, eiPFF exploits the inherent elastic and inertial lift forces induced in a viscoelastic fluid flow to increase the lateral particle deflection for an enhanced separation. The particles to be separated need not be tightly focused, i.e., the width of the particulate solution in the main-branch can be (much) greater than the maximum allowed width, i.e., $w_{p,max}$, in eq 6 as we will demonstrate in the results section below. Consequently, the particle throughput in eiPFF will be significantly higher than that in the traditional PFF. Figure 2 displays the forces exerted on the particles in a viscoelastic fluid that have been focused by a sheath fluid to a layer near a sidewall. $\mathbf{F}_{eL}$ represents the elastic lift force given by,[25,36]

$$\mathbf{F}_{eL} \sim r_p^3 \nabla \mathbf{N}_1 \sim r_p^3 Wi\dot{\gamma}^2 \tag{7}$$

where r_p is the particle radius and $\mathbf{N}_1$ is the first normal stress difference. It increases with *Wi* and directs particles toward the regions of lower shear rate, i.e., the centerline and the four corners in a rectangular channel.[33] The inertial lift force, $\mathbf{F}_{iL}$, has the wall- and the shear gradient-induced components, where the former pushes particles away from the channel wall and the latter acts to direct particles toward the regions of high shear rate.[15,48] For near-wall particles, $\mathbf{F}_{iL}$ has been demonstrated to follow[59]

$$\mathbf{F}_{iL} \sim \rho V_m^2 r_p^6 / w^4 \tag{8}$$

with V_m being the maximum fluid velocity. As indicated by the arrows in Figure 2, $\mathbf{F}_{eL}$ and $\mathbf{F}_{iL}$ work together to deflect particles toward the channel center. This is why we term this particle separation approach eiPFF, which is efficient due to the strong dependence of both types of lift forces on particle size.

5.4 Results and discussion

5.4.1 Effects of fluid elasticity (*Wi*) and inertia (*Re*)

Figure 3 shows the effects of fluid elasticity (in terms of *Wi*) and inertia (in terms of *Re*) on the continuous separation of 3 μm and 10 μm particles in Newtonian (*El* = 0, top row) and non-Newtonian (1000 ppm PEO with *El* = 42.5, bottom row) fluids, respectively, in a 40-μm deep channel. The flow rate ratio between the sheath fluid and particle mixture was maintained at α = 20. A 3D numerical simulation of the flow field (COMSOL®) reveals that at this ratio the particle solution is squeezed to a fluid layer with $w_p = 7$ μm (more accurately, varying from 6.5 μm in the middle plane to 7.5 μm near the top/bottom walls; see the highlighted dimension in Figure 2) in the main-branch.

This value is slightly larger than the maximum allowed width of the focused particle solution, i.e., $w_{p,max}$ = (3.1+9.9)/2 = 6.5 μm in eq 6, for the traditional PFF. In other words, the two particles cannot be completely separated by PFF at α = 20. This analysis is consistent with the particle separation in the Newtonian fluid at Q_{sheath} = 0.1 ml/h in Figure 3 (top row), where both sizes of particles experience a negligible inertial lift in the main-branch at *Re* = 0.35 and still overlap with each other at the expansion. With the increase of *Re*, 10 μm particles experience a greater inertial lift and are pushed away from the wall at a visibly higher rate than 3 μm ones. An almost clear gap with only a few particles of either size present is thus formed in between the two particle streams as seen from the images at Q_{sheath} = 0.3-1 ml/h in Figure 3 (top row). This separation does not seem to get apparently better at flow rates higher than 1.0 ml/h (*Re* = 3.72) due to the influence of particle dispersion, which is mainly caused by the insufficient particle focusing and the parabolic fluid velocity profile in the channel depth.

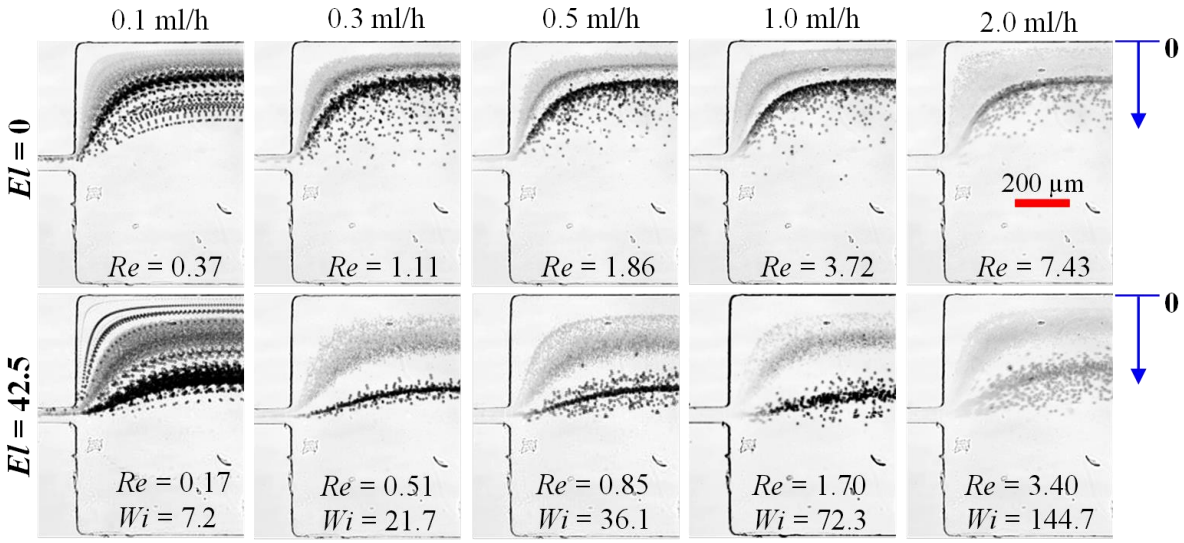

Figure 3. Superimposed images at the expansion of the main-branch comparing the continuous separation of 3 μm (appearing gray) and 10 μm (appearing black) particles in

glycerol/water-based Newtonian (top row, $El = 0$) and non-Newtonian (bottom row, 1000 ppm PEO, $El = 42.5$) fluids at various sheath flow rates (indicated on top of the images) in a 40 μm deep T-shaped microchannel. The flow rate ratio between the sheath fluid and particle mixture was maintained at $\alpha = 20$. The arrows on the right-most images indicate the reference points to which the particle stream positions shown in Figures 4 and 8 were measured. The flow direction is from left to right in all images.

In contrast, the non-Newtonian fluid yields a considerably better separation of 3 μm and 10 μm particles; see the bottom row images in Figure 3. This is attributed to the elasticity-enhanced deflections of both particles in the viscoelastic fluid. At the sheath flow rate Q_{sheath} = 0.1 ml/h, 10 μm particles seem to have an (unstable) equilibrium position near the channel wall (or more accurately, the corner) other than that along the centerline. This phenomenon is absent from 3 μm particles and happens due to the dominant elastic lift force at $Wi = 7.2$ over the inertial lift force at $Re = 0.17$, which is consistent with previous observations.[34-36] With the increase of both *Re* and *Wi* at higher flow rates, 10 μm particles migrate toward the channel centerline yielding a wide and clear gap from the stream of 3 μm particles. However, the deflection of 10 μm particles does not increase monotonically with *Re* due to the combined effects of viscoelastic and inertial lift forces, which direct particles toward the channel centerline[33-37] and the half-way (specifically 0.4 times the channel half-width from the wall),[15,48,59] respectively. It achieves the maximum at Q_{sheath} = 1 ml/h with $Re = 1.70$ among the tested cases in Figure 3 (bottom row), where 10 μm particles are still slightly off the channel center. This implies that the previously reported elasto-inertial particle focusing along the centerline of a straight square microchannel[36,40,45] is sensitive to the flow kinematics and works within a narrow range of flow rate.

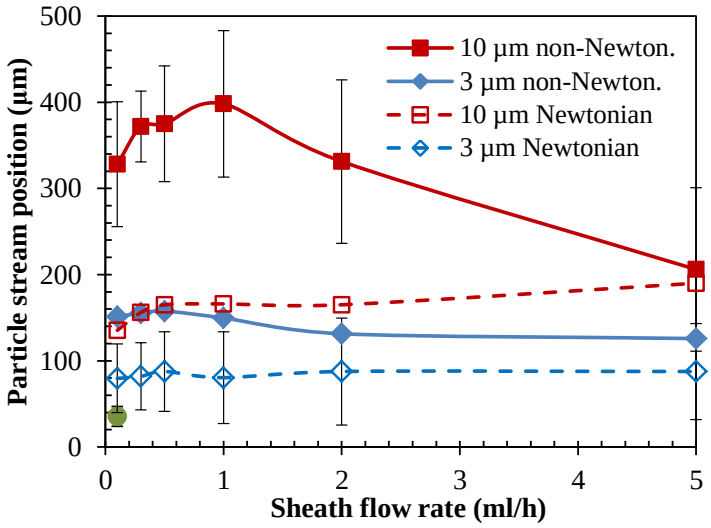

Figure 4. Comparison of the exiting positions of 3 μm and 10 μm particle streams at the expansion of the main-branch (measured from the images in Figure 3 with reference to the top sidewall as indicated by the arrows) in Newtonian (dashed lines with unfilled symbols) and non-Newtonian (solid lines with filled symbols) fluids. Error bars are included for only 3 μm particles in the Newtonian fluid and 10 μm particles in the non-Newtonian fluid for a non-blocked view, which encompass the span of each particle stream. The single data point with a circular symbol near the origin of the plot indicates an (unstable) equilibrium position at the corner of the channel for 10 μm particles in the non-Newtonian fluid due to the dominant elastic lift force at a negligible *Re*. Note that all lines are used to guide eyes only.

A quantitative comparison of the exiting positions of 3 μm- and 10 μm-particle streams in the Newtonian and non-Newtonian fluids is shown in Figure 4. The data (symbols) were measured directly from the particle images in Figure 3, where the top sidewall of the channel expansion was used as the reference point (see the arrows in Figure 3) and the center of the particle traces with the lowest intensity (note the lower intensity, the darker in a gray-scale image) was used as the measuring point. In the Newtonian fluid, the center position of the 3 μm particle stream changes slightly at

around 80 μm (with ±50 μm error bars included in Figure 4 to cover the span of the stream) for the range of flow rates tested. This indicates that 3 μm particles remain confined within the sheath flow-focused particulate solution, which, as noted above, is about 7 μm wide in the 50 μm-wide main-branch and should become around 126 μm in the 900 μm-wide expansion due to the laminar flow feature. In the non-Newtonian fluid, however, 3 μm particles can travel out of the sheath flow-focused particulate solution due to the elastic lift force. Their deflection remains nearly unchanged at around 150 μm when $Q_{sheath} \leq 1$ ml/h ($Re = 1.7$; see Figure 3) and decreases slightly at higher flow rates. The displacement of 10 μm particles increases at a higher flow rate in the Newtonian fluid, which converges to the previously reported equilibrium position for inertial particle focusing in a (nearly) square microchannel,[15,48,59] i.e., 0.4×(900/2) = 180 μm. Moreover, the 10 μm particle deflection in the non-Newtonian fluid (with error bars included in Figure 4) seems to approach the same equilibrium position as in the Newtonian fluid at high flow rates. The former is, however, more than twice larger when $Q_{sheath} < 2$ ml/h ($Re = 3.40$) due to the dominant elasticity over inertia.

5.4.2 Effect of flow rate ratio (α) between sheath fluid and particle mixture

The effect of flow rate ratio, α, between sheath fluid and particle mixture on particle separation via eiPFF was studied in 1000 ppm PEO solution by fixing the sheath flow rate at $Q_{sheath} = 0.3$ ml/h while varying the particle flow rate from 90 μl/h (i.e., $\alpha = 3.3$) to 6 μl/h (i.e., $\alpha = 50$) in a 40 μm deep T-shaped microchannel. Figure 5 shows the superimposed images of 3 μm and 10 μm particles at the T-junction (top row) and

expansion (bottom row) of the main-branch, which clearly demonstrate an enhanced particle separation with the increase of α. Since the total flow rate in the main-branch does not change significantly, *Re* (labeled on the images in Figure 5) slightly decreases from 0.63 to 0.50 when α (as labeled on the images) increases from 3.3 to 50. Accordingly, *Wi* also decreases slightly to maintain the elasticity number at *El* = 42.5. These indicate nearly constant inertial and elastic effects for the cases tested in Figure 5, which explains why the average deflections of 3 µm and 10 µm particles at the expansion remain nearly unaffected by the change of α (see the two dotted lines across the images in the bottom row).

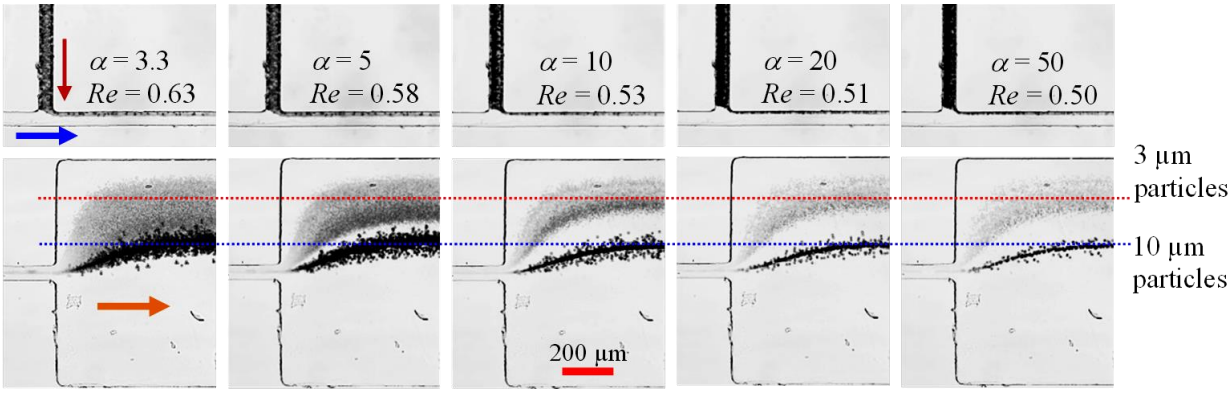

Figure 5. Superimposed images at the T-junction (top row) and expansion (bottom row) of the main-branch illustrating the sheath-flow focusing and elasto-inertial separation of 3 µm and 10 µm particles in 1000 ppm PEO solution through a 40 µm deep T-shaped microchannel. The volume flow rate of the sheath fluid, Q_{sheath}, was maintained at 0.3 ml/h in all cases. The flow rate ratio between the sheath fluid and particle mixture, α, was varied as seen on the images. The two dotted lines across the images are used to assist viewing the effects of α on the exiting positions of the separated particle streams. The block arrows indicate the flow directions.

However, as viewed from the images at the T-junction in Figure 5 (top row), the particle mixture solution is squeezed by the sheath fluid to a narrower layer in the main-

branch with the increase of α. This enhanced focusing helps aligning both sizes of particles, especially important for the smaller ones, against the channel wall, leading to a smaller band of each particle type at the expansion (see the bottom row images in Figure 5). Our 3D flow simulation (COMSOL®) tells that the width of the sheath flow-focused particulate solution, i.e., w_p as highlighted in Figure 2, decreases from 15.1 μm to 13.0, 9.9, 7.4 and 5.5 μm for the tested values of α at 3.3, 5, 10, 20, and 50 in Figure 5. The first five width values are all greater than the maximum allowed width, i.e., $w_{p,max}$ = 6.5 μm, for a theoretically 100% separation via PFF. As a decent separation can be achieved at α as low as 5, eiPFF is able to offer a much higher particle throughput than PFF (which works only for α > 30 based on our 3D flow simulation) at the same sheath flow rate.

5.4.3 Effect of PEO concentration (in terms of *El*)

Figure 6 shows the effect of PEO concentration on the separation of 3 μm and 10 μm particles via eiPFF in a 40 μm deep T-shaped microchannel. The sheath flow rate, Q_{sheath}, was varied to include the inertial effect, but the flow rate ratio was maintained at α = 20. Three different PEO concentrations were tested, which are 500 ppm, 1000 ppm and 2000 ppm. As the fluid viscosity and relaxation time (see Table 1) both increase at a higher PEO concentration, *Re* (labeled on the images) decreases while *Wi* increases yielding a significantly increasing *El* as highlighted in Figure 6. To assist viewing the concentration effect on the particle stream positions, dotted lines, which indicate the exiting positions of 3 μm and 10 μm particles in 1000 ppm PEO solution (*El* = 42.5), have been added onto the images in Figure 6. For the range of flow rates tested (up to

Q_{sheath} = 5 ml/h), 3 μm particles attain a larger deflection with the increase of PEO concentration due to a stronger elastic lift force. Their trajectories, however, do not change significantly with *Re*, except in 2000 ppm PEO solution. These behaviors are better viewed from the exiting stream positions in Figure 7. The deflection of 3 μm particles in 2000 ppm PEO solution quickly decreases from around 260 μm to 100 μm with the increase of flow rate. This phenomenon is believed to be a consequence of the shear thinning effect that gets stronger at a higher PEO concentration and tends to move particles away from the channel centerline.[31,32]

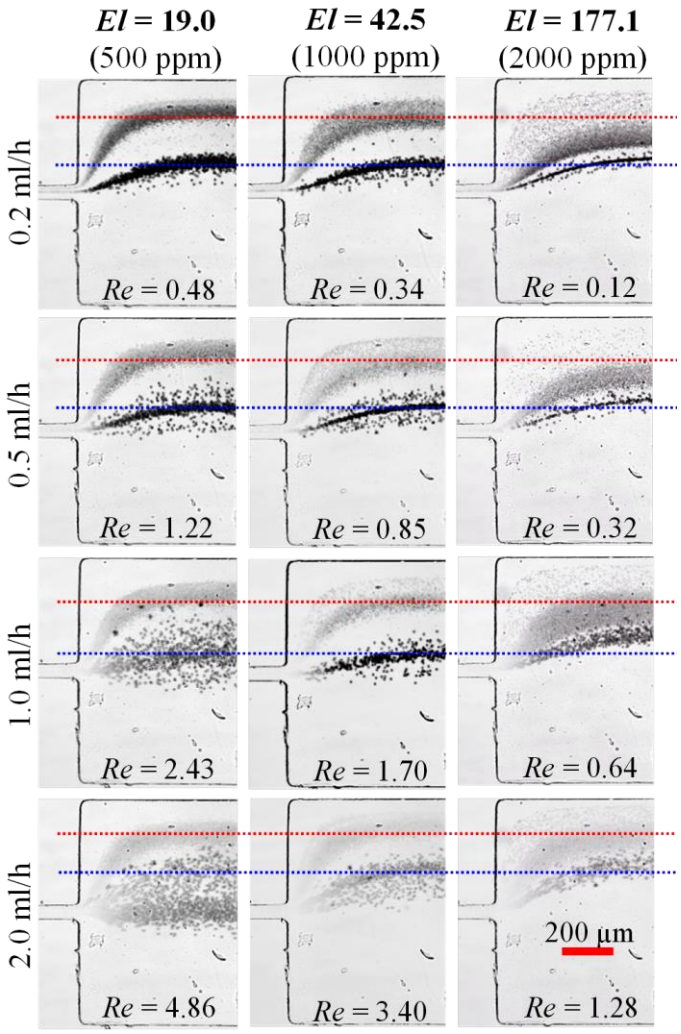

Figure 6. Superimposed images at the expansion of the main-branch illustrating the effect of PEO concentration (500, 1000 and 2000 ppm from left to right; in terms of *El*) on the separation of 3 µm and 10 µm particles via eiPFF in a 40 µm deep T-shaped microchannel. The flow rate ratio between sheath fluid (labeled to the left of the images) and particle mixture was fixed at 20. The dotted lines across the images, which indicate the exiting positions of the two types of particles in 1000 ppm PEO solution, are drawn to assist viewing the PEO concentration effect on the particle stream positions at the expansion.

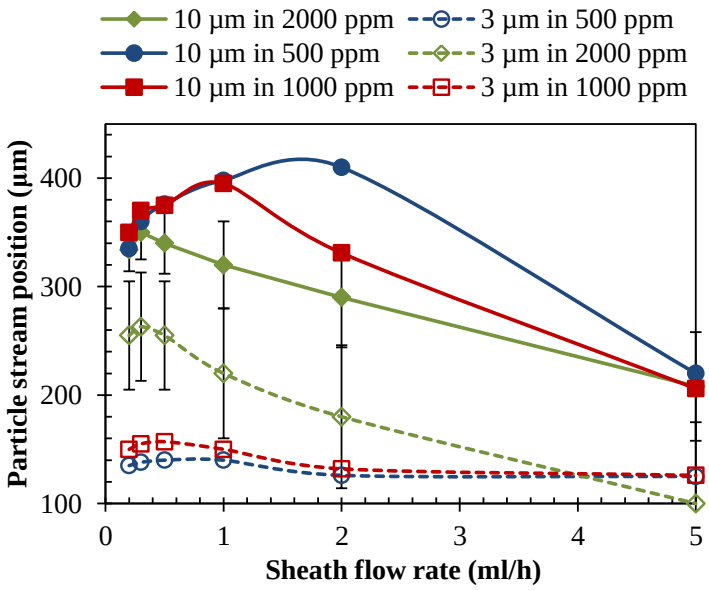

Figure 7. Comparison of the exiting positions of 3 µm (dashed lines) and 10 µm (solid lines) particle streams at the expansion of the main-branch (measured directly from the images in Figure 6) in non-Newtonian fluids with different PEO concentrations. Error bars are included for particles suspended in 2000 ppm PEO solution. Note that all lines are used to guide eyes only.

In contrast, the deflection of 10 µm particles is much more profound and dependent on both *Re* and *El* (or *Wi*). It attains the maximum value in 1000 ppm PEO solution at small flow rates (up to 1 ml/h) while in 500 ppm PEO solution at higher flow rates. Since 3 µm particles experience a larger deflection at a higher PEO concentration, the separation in 2000 ppm PEO turns out to be the worst in all tested flow rates as seen from Figure 6. This is clearly viewed from the exiting positions of both particle streams (with error bars included to cover the span) in Figure 7. The 10 µm particle deflection follows a similar first-rise/then-drop trend with *Re* in all three PEO solutions. However, the turning point occurs at the largest flow rate in 500 ppm PEO (2 ml/h vs. 1 ml/h in 1000 ppm and 0.3 ml/h in 2000 ppm. Interestingly and importantly, 10 µm particles can

be deflected all the way to the channel center in 500 ppm PEO solution, which was not observed in the two higher concentrations. This may imply a potentially high-throughput particle separation in a low concentration PEO solution or a non-Newtonian fluid with a weaker elasticity such as the hyaluronic acid used recently for inertia-elastic particle focusing at *Re* up to 10,000.[39]

5.4.4 Effect of channel aspect ratio (*AR*)

Figure 8 shows the effect of channel aspect ratio, *AR*, on the separation of 3 μm and 10 μm particles via eiPFF in 1000 ppm PEO solution through 100, 40 and 25 μm (from left to right) deep T-shaped microchannels. Both *Re* and *Wi* increase in a shallower channel, i.e., with a larger *AR*, while the latter is about twice faster. This yields an increasing *El* with the increase of *AR*. In the channel with *AR* = 0.5 (i.e., 100 μm deep), 10 μm particles can have two equilibrium positions, i.e., the corners and centerline, at Q_{sheath} < 0.3 ml/h in Figure 8 (left column) due to the dominant elastic lift force at negligible *Re*. Moreover, the higher the flow rate, the more 10 μm particles are along the centerline. This phenomenon is different from the inertial particle motion in Newtonian fluids in a low-*AR* microchannel, where the particle equilibrium positions are preferably centered at the wider faces in the channel depth direction.[15,48,60] A visible separation of 10 μm particles from 3 μm particles is achieved at Q_{sheath} = 0.5 ml/h (*Re* = 0.51) and gets better at 1.0 ml/h. This trend is similar to that in the channel with *AR* = 1.25 (i.e., 40 μm deep, middle column of Figure 8) where the separation is visually better though the deflections of both sizes of particles are smaller. In contrast, the particle behavior in the

channel with AR = 2.0 (i.e., 25 μm deep) are much more interesting. As seen from the images in the right column of Figure 8, the deflection of 10 μm particles can be either smaller (at low flow rates) or larger (at high flow rates) than that of 3 μm particles depending on the value of Re. This switch takes place at Q_{sheath} = 0.5 ml/h where Re = 1.02. Such a surprising phenomenon also occurs for 500 and 2000 ppm PEO solutions in the same channel (data not shown). It is, however, absent from the particle motion in Newtonian fluids, where larger particles always migrate to the channel centerline faster than smaller ones due to the rotation-induced inertial lift force.[61] In addition, the stream width of each size of particles in the 25 μm deep channel seems to be the narrowest among the three channels due to perhaps the strongest steric effects from the top/bottom walls therein.

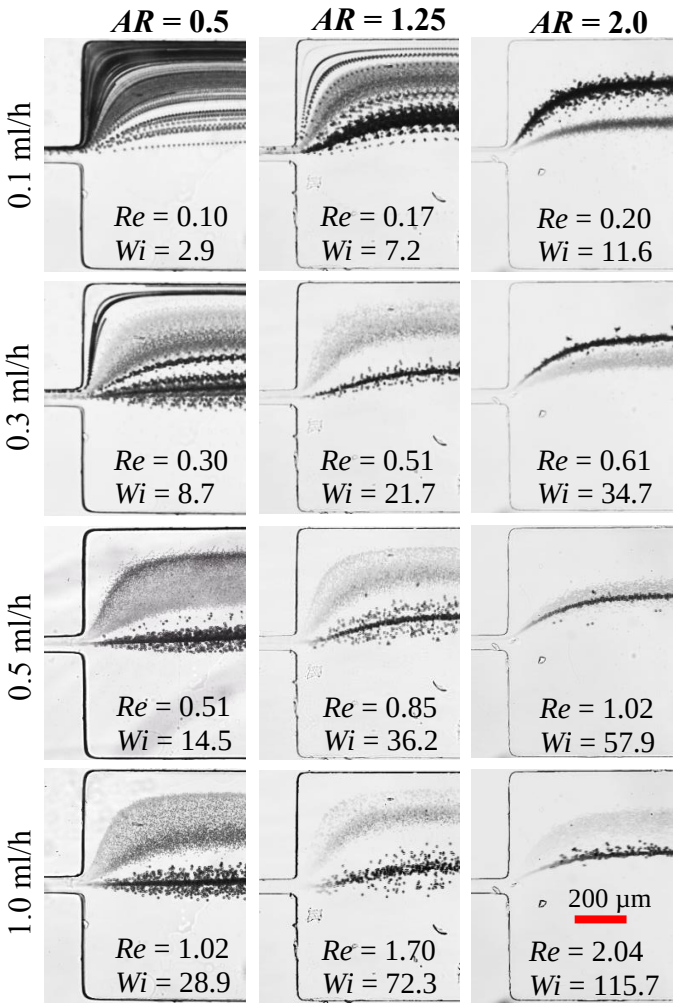

Figure 8. Superimposed images at the expansion of the main-branch illustrating the effect of aspect ratio, *AR*, on the 3 µm and 10 µm particle separation via eiPFF in T-shaped microchannels of various depths (100, 40 and 25 µm from left to right). The sheath flow rate, Q_{sheath}, was varied as labeled while the flow rate ratio between sheath fluid and particle mixture was fixed at 20.

Figure 9 compares the exiting positions of 3 µm and 10 µm particle streams (with error bars included) at the expansion of the main-branch in T-shaped microchannels with (A) *AR* = 0.5 (i.e., 100 µm deep) and (B) *AR* = 2.0 (i.e., 25 µm deep), respectively. These two graphs can be compared directly to that in Figure 4 for the channel with *AR* = 1.25 (i.e., 40 µm deep). The deflection of 10 µm particles exhibits a similar trend in all three

depths of channels, which first increases with the rise of flow rate and then decreases at higher flow rates. However, the maximum deflection decreases from 450 µm (right along the centerline of the expansion) in the deepest channel to around 340 µm in the shallowest channel. While the flow rate at which the maximum particle deflection happens seems to remain at approximately 1 ml/h in all three channels, the slope of the decreasing particle deflection with flow rate turns out to be the steepest in the 40 µm deep channel. In contrast, the deflection of 3 µm particles in the 25 µm-deep channel decreases with the increase of flow rate, which is apparently different from that in the two deeper channels.

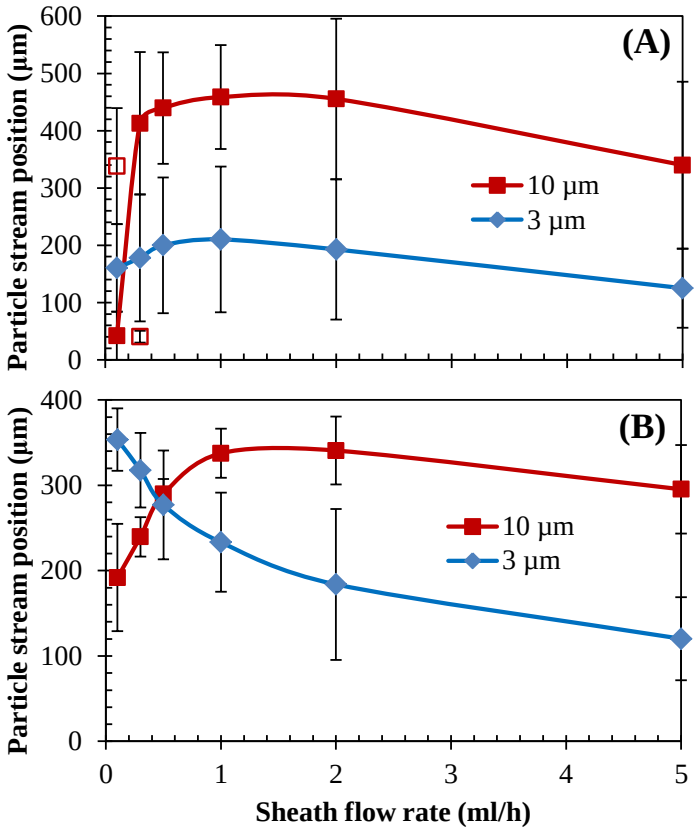

Figure 9. Comparison of the exiting positions (symbols with error bars, measured directly from the images in Figure 8) of 3 µm and 10 µm particle streams in 1000 ppm

PEO solution at the expansion of the main-branch in T-shaped microchannels with (A) AR = 0.5 (100 μm deep) and (B) AR = 2.0 (25 μm deep), respectively. The unfilled data points in (A) represent a secondary equilibrium position (with fewer particles present) at the corner of the channel for 10 μm particles. Note that all lines are used to guide eyes only.

5.5 Conclusions

We have conducted a systematic experimental study of the continuous particle separation in PEO solutions via eiPFF. Five dimensionless numbers, i.e., *Re*, *Wi*, *El*, α and *AR*, have been used to quantify the parametric effects for a fundamental understanding of the important factors in device design and control. We have demonstrated that eiPFF offers a much higher particle throughput and a much better separation resolution than the traditional PFF. Moreover, as it works most efficiently for *Re* of order 1, eiPFF fills perfectly into the gap of our recently proposed inertia-enhanced PFF (iPFF) technique[56] that requires *Re* of order 10 or more. This feature makes eiPFF suitable for particle and cell separation in microfluidic devices that typically process a limited amount of samples.[62,63] In addition, eiPFF has the potential to separate particles of 1 μm diameter[26] or even smaller[34], which is very hard (if not impossible) for iPFF[56] and other inertia-based separation techniques.[15,48] We have also observed two new phenomena that have not been reported in the literature: one is that the particle focusing and separation via eiPFF does not increase monotonically with *El* at higher PEO concentrations due to the mutual influences of elastic and inertial effects; and the other is that the channel aspect ratio, *AR*, strongly affects the particle separation due to its influence on the particle deflection. More surprisingly, the elasto-inertial deflection of

small particles can be even greater than that of large ones in a high-*AR* channel when *Re* is less than 1.

Acknowledgements

This work was partially supported by Clemson University through a departmental SGER (Small Grants for Exploratory Research) grant.

Supporting Information Available (Appendix A)

Details on how to determine the Newtonian and non-Newtonian fluid properties in Table 1 and how to understand eq 6. This information is available free of charge via the Internet at http://pubs.acs.org/.

References

(1) Pamme, N. *Lab Chip* **2007**, *7*, 1644-1659.

(2) Gossett, D. R.; Weaver, W. M.; Mach, A. J.; Hur, S. C.; Tse, H. T.; Lee, W.; Amini, H.; Di Carlo, D. *Anal. Bioanal. Chem.* **2010**, *397*, 3249-3267.

(3) Karimi, A.; Yazdi, S.; Ardekani, A. M. *Biomicrofluid.* **2013**, *7*, 021501.

(4) Pethig, R. *Biomicrofluid.* **2010**, *4*, 022811.

(5) Kim, S. B.; Yoon, S. Y.; Sung. H. J.; Kim, S. S. *Anal. Chem.* 2008, *80*, 2628-2630.

(6) Ding, X.; Li, P.; Lin, P. S. C.; Stratton, Z. S.; Nama, N.; Guo, F.; Slotcavage, D.; Mao, X. Shi, J.; Costanzo, F.; Huang, T. J. *Lab Chip* **2013**, *13*, 3626-3649.

(7) Hejazian, M.; Li, W.; Nguyen, N. T. *Lab Chip* **2015**, *15*, 959-970.

(8) Watarai, H. *Annu. Rev. Anal. Chem.* **2013**, *6*, 353-378.

(9) Regtmeier, J.; Eichhorn, R.; Viefhues, M.; Bogunovic, L.; Anselmetti, D. *Electrophoresis* **2011**, *32*, 2253-2273.

(10) Huang, L.; Cox, E. C.; Austin, R. H.; Sturm, J. C. *Science* **2004**, *304*, 987-990.

(11) Yamada, M.; Seki, M. *Anal. Chem.* **2006**, *78*, 1357-1362.

(12) Choi, S. Y.; Song , S.; Choi, C.; Park, J. K. *Anal. Chem.* **2009**, *81*, 1964-1968.

(13) Giddings, J. C. *J. Chromatogr.* **1989**, *480*, 21-33.

(14) Yamada, M.; Nakashima, M.; Seki, M. *Anal. Chem.* **2004**, *76*, 5465-5471.

(15) Martel, J. M.; Toner, M. *Annu. Rev. Biomed. Eng.* **2014**, *16*, 371-396.

(16) Pipe, C. J.; McKinley, G. H. *Mech. Research Comm.* **2009**, *36*, 110-120.

(17) Berli, C. L. A. *Electrophoresis* **2013**, *34*, 622-630.

(18) Zhao, C.; Yang, C. *Adv. Colloid Interf. Sci.* **2013**, *201-202*, 94-108.

(19) Karnis, A.; Goldsmith, H. L.; Mason, S. G. *Nature* **1963**, *200*, 159-160.

(20) Karnis, A.; Mason, S. G. *Trans. Soc. Rheol.* **1966**, *10*, 571-592.

(21) McKinley, G. H. *Transport Processes in Bubbles, Drops & Particles*, **2001**, chapter 14, 2nd Ed. Ed. R. Chhabra, D. De Kee, Taylor & Francis.

(22) Leal, G. *J. Non-Newton. Fluid Mech.* **1979**, *5*, 33-78.

(23) Becker, L. E.; McKinley, G. H.; Rasmussen, H. K.; Hassager, O. *J. Rheol.* **1994**, *38*, 377-403.

(24) Arigo, M. T.; Mckinley, G. H. *Rheol. Acta* **1998**, *37*, 307-327.

(25) Leshansky, A. M.; Bransky, A.; Korin, N.; Dinnar, U. *Phys. Rev. Lett.* **2007**, *98*, 234501.

(26) Kang, K.; Lee, S. S.; Hyun, K.; Lee, S. J.; Kim, J. M. *Nat. Comm.* **2013**, *4*, Article number: 2567. doi:10.1038/ncomms3567.

(27) Romeo, G.; D'Avino, G.; Greco, F.; Nettiab, P. A.; Maffettone, P. L. *Lab Chip* **2013**, *13*, 2802-2807.

(28) Ho, B. P.; Leal, L. G. *J. Fluid Mech.* **1976**, *76*, 783-799.

(29) Huang, P. Y.; Feng, J.; Hu, H. H.; Joseph, D. D. *J. Fluid Mech.* **1997**, *343*, 73-94.

(30) Villone, M. M.; D'Avino, G.; Hulsen, M. A.; Greco, F.; Maffettone, P. L. *J. Non-Newton. Fluid Mech.* **2011**, *166*, 1396-1405.

(31) Huang, P. Y.; Joseph, D. D. *J. Non-Newtonian Fluid Mech.* **2000**, *90*, 159-185.

(32) Seo, K. W.; Byeon, H. J.; Huh, H. K. Lee, S. J. *RSC Adv.* **2014**, *4*, 3512-3520.

(33) D'Avino, G.; Maffettone, P. L. *J. Non-Newton. Fluid Mech.* **2015**, *215*, 80-104.

(34) Kim, J. Y.; Ahn, S. W.; Lee, S. S.; Kim, J. M. *Lab Chip* **2012**, *12*, 2807-2814.

(35) Seo, K. W.; Kang, Y. J.; Lee, S. J. *Phys. Fluid.* **2014**, *26*, 063301.

(36) Yang, S. Y.; Kim, J. Y.; Lee, S. J.; Lee, S. S.; Kim, J. M. *Lab Chip* **2011**, *11*, 266-273.

(37) Giudice, F. D.; Romeo, G.; D'Avino, G.; Greco, F.; Netti, P. A.; Maffettone, P. L. *Lab Chip* **2013**, *13*, 4263-4271.

(38) Lim, H.; Nam, J. Shin, S. *Microfluid. Nanofluid.* **2014**, *17*, 683-692.

(39) Lim, E. J.; Ober, T.; Edd, J. F.; Desai, S. P.; Neal, D.; Bong, K. W.; Doyle, P. S.; McKinley, G. H.; Toner, M. *Nat. Comm.* **2014**, *5*, Article number: 4120. doi:10.1038/ncomms5120.

(40) Ahn, S. W.; Lee, S. S.; Lee, S. J.; Kim, J. M. *Chem. Eng. Sci.* **2015**, *126*, 237-243.

(41) Cha, S.; Kang, K. You, J. B.; Im, S. G.; Kim, Y. Kim, J. M. *Rehol. Acta* **2014**, *53*, 927-933.

(42) Lee, D. L.; Brenner, H. Youn, J. R. Song, Y. S. *Sci. Rep.* **2013**, *3*, article number 3258. DOI: 10.1038/srep03258.

(43) Cha, S.; Shin, T.; Lee, S. S.; Shim, W.; Lee, G. Lee, S. J.; Kim, Y.; Kim, J. M. *Anal. Chem.* **2012**, *84*, 10471-10477.

(44) Seo, K. W.; Ha, Y. R.; Lee, S. J. *Appl. Phys. Lett.* **2014**, *104*, 213702.

(45) Yang, S.; Lee, S. S.; Ahn, S. W.; Kang, K.; Shim, W.; Lee, G.; Hyune, K.; Kim, J. M. *Soft Matt.* **2012**, *8*, 5011-5019.

(46) Geislinger, T. M.; Franke, T. *Adv. Colloid Interf. Sci.* **2014**, *208*, 161-176.

(47) Nam, J.; Lim, H.; Kim, D.; Jung, H.; Shin, S. *Lab Chip* **2012**, *12*, 1347-1354.

(48) Amini, H.; Lee, W.; Di Carlo, D. *Lab Chip* **2014**, *14*, 2739-2761.

(49) Liang, L.; Qian, S.; Xuan, X. *J. Colloid Interf. Sci.* **2010**, *350*, 377-379.

(50) Lu, X.; Patel, S.; Zhang, M.; Joo, S.; Qian, S.; Ogale, A.; Xuan, X. *Biomicrofluid.* **2014**, *8*, 021802.

(51) Maenaka, H.; Yamada, M.; Yasuda, M.; Seki, M. *Langmuir* **2008**, *24*, 4405-4410.

(52) Mortensen, N. A. *Anal. Chem.* **2007**, *79*, 9240-9241.

(53) Jain, A.; Posner, J. D. *Anal. Chem.* **2008**, *80*, 1641-1648.

(54) Nho, H. W.; Yoon, T. H. *Lab Chip* **2013**, *13*, 773-776.

(55) Lu, X.; Hsu, J. P.; Xuan, X. *Langmuir* **2015**, *31*, 620-627.

(56) Lu, X.; Xuan, X. *Anal. Chem.* **2015**, *87*, 4560-4565.

(57) Lee, K. H.; Kim, S. B.; Lee, K. S.; Sung, H. J. *Lab Chip* **2011**, *11*, 354-357.

(58) Morijiri, M.; Sunahiro, S.; Senaha, M.; Yamada, M.; Seki, M. *Microfluid. Nanofluid.* **2011**, *11*, 105-110.

(59) Di Carlo, D.; Edd, J. F.; Humphry, K. J.; Stone, H. A.; Toner, M. *Phys. Rev. Lett.* **2009**, *102*, 094503.

(60) Bhagat, A. A. S.; Kuntaegowdanahalli, S. S.; Papautsky, I. *Phys. Fluid.* **2008**, *20*, 101702.

(61) Zhou, J.; Papautsky, I. *Lab Chip* **2013**, *13*, 1121-1132.

(62) Reyes, D. R.; Iossifidis, D.; Auroux, P. A.; Manz, A., *Anal. Chem.* **2002**, *74*, 2623-2636.

(63) Auroux, P. A.; Iossifidis, D.; Reyes, D. R.; Manz, A., *Anal. Chem.* **2002**, *74*, 2627-2652.

CHAPTER SIX

PARTICLE FOCUSING IN VISCOELASTIC FLUIDS THROUGH RECTANGULAR STRAIGHT MICROCHANNELS

Abstract

Particle transport in non-Newtonian fluids has recently drawn increasing attentions for Lab-on-a-chip devices due to its potential on particle focusing and sorting. However, the understanding of the particle equilibrium position and focusing in experiment and numerical simulation are still incomplete. In this work, we have a comprehensive study of the elasto-inertial particle focusing in terms of various parameters, such as particle size, flow rate, channel aspect ratio and polymer solution type. Multiple equilibrium positions are observed and affected by the parameters stated above significantly. With aspect ratio increasing from 0.5 to 3.3 at moderate flow rate, the multiple equilibrium positions (center and walls) shift to one center position, then to two off-center positions, and finally to multiple equilibrium positions (center and off-centers) again. In addition, an interesting trend is found that the particle size (blockage ratio) plays a less significant role on the equilibrium position with the increase of channel aspect ratio. A size-based particle separation is also achieved. Moreover, the differences of the equilibrium positions in different types of polymer solution are presented. Further experiments in polyacrylamide (PAA) solutions of varied glycerol concentrations in a near-slit channel demonstrate that the shear-thinning effect inhibits the elastic lift and deflects particles away from the center. The 2D numerical study of the Oldroyd-B and

Giesekus models supports our analysis of the viscoelastic and shear thinning effects qualitatively.

6.1 Introduction

Lab-on-a-chip devices have become effective platforms for many biomedical and chemical applications because of the advantages of high efficiency, accuracy and low cost (Stone et al. 2004; Dittrich and Manz 2006). Among the numerous applications, particle (synthetic or biological) focusing and sorting (Sajeesh and Sen 2014; Shields et al. 2015) can be implemented based on different characteristics such as size, shape, deformability, density, charge and polarizability (electric, magnetic and optical) etc, though a variety of microfluidic approaches. By the use of externally imposed optical (Jung et al. 2014), acoustic (Ding et al. 2013), electric (Swaminathan et al. 2015), and magnetic (Zhou et al. 2015) fields, active particle manipulations have been developed. Additionally, passive particle manipulations have been achieved via confinement-induced hydrodynamic or electric forces, which cover approaches of hydrodynamic filtration (HDF) (Yamada and Seki 2005), deterministic lateral displacement (DLD) (Huang et al. 2004), hydrophoresis (Choi and Park 2007), pinched flow fractionation (PFF) (Yamada et al. 2004), inertia (Lu and Xuan 2015a), elasto-inertia (Kang et al. 2013; Nam et al. 2012; Lu and Xuan 2015b), and insulator-based dielectrophoresis (DuBose et al. 2014). Among them, elasto-inertial technique has demonstrated effective particle manipulations and draws increasing attentions from scientists and engineers.

Particle transport in viscoelastic fluid has been studied for half a century. In the 1960s and 1970s, Karnis et al (Karnis and Mason 1966; Gauthier F et al. 1971) studied the particle cross-stream migration in a pipe flow, where inward migration to centerline was observed. The nonzero normal stress in a viscoelastic fluid was reported as the source of the cross-stream particle migration. With the rapid development of state-of-the-art micro-fabrication technologies, recent studies have been shifted to rectangular microchannels (Leshansky et al. 2007; Kang et al. 2011; Lim et al. 2014; Del Giudice et al. 2013; Del Giudice et al. 2015). Multiple equilibrium positions (centerline and corners) were observed for rigid colloidal particles in the viscoelastic flow (Kim and Yoo 2008; Kim et al. 2012), which were influenced by a combined effect of inertia and viscoelasticity (Seo et al. 2014). The elasto-inertial particle migration has also been used for particle separation in a few recent studies. Separation was demonstrated for different particles of different features, such as size (Liu et al. 2015), shape (Lu et al. 2016c), and deformability (Yang et al. 2012).

A few Numerical studies have predicted the viscoelastic particle focusing. Different non-Newtonian constitutive equations were used, such as Oldroyd-B (OB) (Huang et al. 2000), Giesekus (Villone et al. 2011a), and PTT model (Villone et al. 2013). The OB model has constant viscosity, i.e., the so-called Boger fluids (James 2009), while the others have shear thinning effect. Due to the high computational expanse, most works were in 2D Poiseuille flows. Lee et al. (2010) predicted that cylinder particle migrated to the center by OB model. Trofa et al. (2015) predicted both center and wall equilibrium positions with consideration of shear thinning effect by

Giesekus model. Villone et al. (2011b), Villone et al. (2013) and Li et al. (2015) studied viscoelastic and shear thinning effects in three dimensional channels. They stated that the shear thinning reduced the particle center focusing. Consistently, most of those works agreed that the increases of shear thinning, flow rate and particle size affect the migration speed. In addition, some models neglected the inertial term, which has been demonstrated appropriate by Trofa et al. (2015). They presented that the inertial effect was not relevant until the Reynolds number is two orders of magnitudes higher than Weissenberg number.

This work presents a systematic study of particle focusing in non-Newtonian fluid through a rectangular straight channel as functions of flow rate, blockage ratio, channel aspect ratio, and polymer type which affects shear thinning and viscoelasticity. It is demonstrated that the focusing phenomenon is highly dependent on these parameters. Two interesting phenomena, equilibrium position change and blockage ratio dependence, in terms of aspect ratio are observed as stated in the abstract. Meanwhile, the focusing study guides us to achieve a size-based elasto-inertial separation. In addition, the experiment of the polymer type effect in a near-slit channel explores the differences between the fluids with only viscoelastic effect and that with both viscoelastic and shear-thinning effects. The shear-thinning effect is demonstrated to suppress the elastic lift and drive particles towards the wall. The numerical results also support our conclusion qualitatively. In the following parts, we first briefly describe the preparations of microchannel and particle suspension, experimental setup, and dimensionless number involved in experiment. The modelling governing equations, methods and code validation are followed. Then, we present the result section of parametric studies on particle

focusing in terms of the defined dimensionless numbers, a size-based separation, comparison of polymer type effect, and the numerical analysis. Finally, we present the conclusion.

6.2 Experiment

6.2.1 Microchannel fabrication and particle suspensions

2 cm-long straight microchannels were used in experiment with 50 μm width and different depths, which were 15, 25, 40, 100, and 340 μm. At the end of the channel, a 900 μm-wide and 2 mm-long expansion was added to enhance and visualize particle separation. The microchannels were fabricated through standard soft lithography method with polydimethylsiloxane (PDMS). The detailed procedure was referred to Lu et al (2014). The 100 μm-deep channel was fabricated by a double-layer soft lithography method. After coating the 40 μm-thick SU-8-25 photoresist (MicroChem) and a two-step soft bake (65 °C for 4 min and 95 °C for 8 min) in a hot plate (HP30A, Torrey Pines Scientific), another layer of photoresist was coated onto the first layer using the same coating. By measuring through the microscope (Nikon Eclipse TE2000U, Nikon Instruments), the thickness of the two layers was around 100 μm. The 340 μm-deep channel was fabricated with the SU-8-2100 photoresist (MicroChem). The coating speed started at 500 rpm for 10 s and ramped by 300 rpm/s to the terminal spin speed of 1000 rpm with a dwelling of 30 s. After a two-step soft bake (65 °C for 7 min and 95 °C for 60 min) on the hot plate, the photoresist film was exposed through the photo mask to a 365 nm UV light (ABM Inc., San Jose, CA) for 50 seconds. It then underwent a two-step hard

bake (65 °C for 5 min and 95 °C for 15 min) before being submerged into a SU-8 developer solution (MicroChem) for 20 min. Following a brief rinse with isopropyl alcohol (Fisher Scientific) and another two-step hard bake (65 °C for 1 min and 95 °C for 5 min), a positive replica of photoresist was left on the glass slide with 340 μm thickness by measuring through the microscope.

3.1, 4.8 and 9.9 μm-diameter spherical polystyrene particles (Thermo Scientific) were used in experiment. The particles were suspended in water-based Newtonian solution and three types of dilute non-Newtonian solutions with concentration of about 10^6 particles/ml. The non-Newtonian solutions are 1000 ppm polyethylene oxide (PEO, molecular weight $M_w = 2\times10^6$ Da, Sigma-Aldrich), 50 ppm polyacrylamide (PAA, $M_w = 18\times10^6$ Da, Polysciences) and 8% Polyvinylpyrrolidone (PVP, $M_w = 0.36\times10^6$ Da, Sigma-Aldrich) solutions. 0.5% (v/v) Tween 20 (Fisher Scientific) was added to all solutions to reduce the influences of particle aggregations and adhesions to channel walls. Table 1 lists the solution properties. The calculation of effective relaxation time of the 1000 ppm PEO solution is provided in Supplementary Material (Appendix B). The effective relaxation times of PVP (Del Giudice et al. 2013) and PAA (Campo-Deaño et al. 2011) solutions and the zero-shear viscosities of PEO (Rodd et al. 2005), PVP (Del Giudice et al. 2013), and PAA (Galindo-Rosales et al. 2012) solutions were obtained from previous work. The PVP (Del Giudice et al. 2013) and dilute PEO (Cox and Brenner 1968; Rodd et al. 2005; Rodd et al. 2007) solutions exhibit non- or mild shear-thinning effect, while the PAA solution (Galindo-Rosales et al. 2012) shows strong shear-thinning effect.

Table 1. Properties of water-based non-Newtonian fluids used in experiments.

Fluid properties (at 20 °C)	1000ppm PEO	8% PVP	50ppm PAA
Density ρ (g/cm^3)	1.0	1.0	1.0
Zero-shear viscosity η_0 (mPa·s)	2.3	90	30
Effective relaxation time, λ_e (ms)	6.8	1.3	10

6.2.2 Experimental setup

The particle suspension was stored in a 100 µl air-tight glass syringe (SGE Analytical Science) and driven through the microchannel by an infusion syringe pump (KDS-100, KD Scientific). The glass syringe and microchannel was connected via a PFA (perfluoro alkoxy alkane) tubing (IDEX Health & Science). Particle motion was visualized and recorded by an inverted microscope (Nikon Eclipse TE2000U, Nikon Instruments) with a CCD camera (Nikon DS-Qi1Mc) at frame rate of 15 frames per second. The 3.1 µm fluorescent particles were observed under fluorescent light for better visualization. The lens had magnification of 10 times, numerical aperture of 0.3 and the depth of field of around 8 µm. Post-processing was made by Nikon imaging software (NIS-Elements AR 3.22). Particle streak images were used to illustrate particle transport, which were obtained by superimposing a sequence of around 500 snapshot images with minimum and maximum intensity projections for the plain and 3.1 µm fluorescent particles respectively. Particle analysis with ImageJ software package (NIH) was used to measure the particle positions along the lateral direction by conducting for about 500 images (more than 200 particles). The probability distribution function (PDF) was calculated based on the particle positions.

6.2.3 Dimensionless numbers

Four dimensionless numbers are used to characterize the flow dynamics of non-Newtonian fluid. Usually measuring the fluid elasticity, Weissenberg number is defined as the ratio of effective relaxation time and the average shear rate, $\dot{\gamma}$,

$$Wi = \lambda_e \dot{\gamma} = \lambda_e \frac{V}{w/2} = \frac{2\lambda_e Q}{w^2 h} \quad (1)$$

in which λ_e is the effective relaxation times, V is the average fluid velocity, w and h are the width and height of the straight channel, and Q is the volumetric flow rate. Reynolds number is defined as the ratio of the inertial force to the viscous force,

$$Re = \frac{\rho V D_h}{\eta_0} = \frac{2\rho Q}{\eta_0 (w+h)} \quad (2)$$

where D_h is the hydraulic diameter. The channel aspect ratio is the ratio of channel width to height, which affects the particle equilibrium positions in non-Newtonian fluid,

$$AR = w/h \quad (3)$$

The channel depths used in experiment are 15, 25, 40,100, and 340 μm corresponding to AR = 3.3, 2, 1.25, 0.5, and 0.15. The blockage ratio, the ratio of the particle diameter and the hydraulic diameter of microchannel, is given by

$$\beta = d/D_h \quad (4)$$

6.3 Numerical modeling

6.3.1 Mathematical model and numerical method

Fig. 1 shows the schematic diagram of the computational model: a rigid, non-Brownian, circular particle (2D) suspended in a straight channel in Poiseuille flow. The flow domain sigma denotes the rectangular channel with width *w* and length *L* (*L*>100*w*) subtracted by the circular particle with diameter *d*. The external boundaries are denoted by Γ_{1-4}, and the internal particle boundary is denoted by $\Gamma_5(t)$. The Cartesian x and y coordinates with the origin located at the center of the microchannel are illustrated in Fig. 1. A parabolic velocity profile is imposed on the left boundary, driving fluid flowing along the x-direction, and the upper and lower boundaries are channel walls.

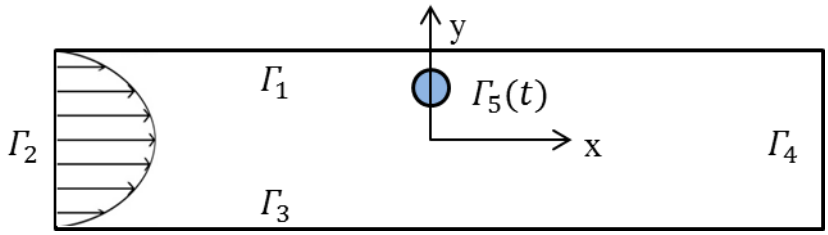

Fig. 1. Sketch of the flow cell

The elasto-inertial particle motion in viscoelastic fluid is investigated using the direct numerical simulation (DNS) method. The hydrodynamic force and torque acting on the particle are computed from the flow field which is fully coupled with the particle translational and rotational motions. The incompressible viscoelastic flow is governed by continuity and Navier-Stokes equations,

$$\nabla \cdot \mathbf{u} = 0 \tag{5}$$

$$\rho\left(\frac{\partial \mathbf{u}}{\partial t} + \mathbf{u} \cdot \nabla \mathbf{u}\right) = \nabla \cdot \boldsymbol{\sigma} \tag{6}$$

$$\boldsymbol{\sigma} = -p\mathbf{I} + 2\mu_s \mathbf{D} + \boldsymbol{\tau} \tag{7}$$

where $\mathbf{D} = [\nabla\mathbf{u} + (\nabla\mathbf{u})^{\mathrm{T}}]/2$ is rate-of-deformation tensor, $\mathbf{I}$ is the unit tensor, and μ_s is the solvent viscosity. The symmetric $\boldsymbol{\tau}$ is extra stress contribution owing to the polymer, which is written in terms of the conformation tensor $\mathbf{c}$

$$\boldsymbol{\tau} = \frac{\mu_p}{\lambda}(\mathbf{c} - \mathbf{I}) \tag{8}$$

where μ_p is the polymer viscosity and λ is the polymer relaxation time. The fluid dynamic viscosity $\mu = \mu_p + \mu_s$. The Giesekus constitutive equation is used to describe the transport of polymer stress in the flow:

$$\lambda \overset{\nabla}{\mathbf{c}} + \mathbf{c} - \mathbf{I} + \alpha(\mathbf{c} - \mathbf{I})^2 = 0 \tag{9}$$

where $\overset{\nabla}{\mathbf{c}}$ is the upper convected derivative

$$\overset{\nabla}{\mathbf{c}} = \frac{\partial \mathbf{c}}{\partial t} + \mathbf{u}\bullet\nabla\mathbf{c} - \left[(\nabla\mathbf{u})\cdot\mathbf{c} + \mathbf{c}\cdot(\nabla\mathbf{u})^{\mathrm{T}}\right] \tag{10}$$

α is the mobility parameter that accounts for the shear thinning behavior. It reduces to the Oldroyd-B model at α=0, which can be used to simulate viscoelastic fluids with a constant viscosity. Dimensionless governing equations are respectively

$$\nabla' \cdot \mathbf{u}' = 0 \tag{11}$$

$$Re_m\left(\frac{\partial \mathbf{u}'}{\partial t'} + \mathbf{u}' \cdot \nabla'\mathbf{u}'\right) = \nabla' \cdot \boldsymbol{\sigma}' \tag{12}$$

$$Wi_m \overset{\nabla}{\mathbf{c}}{}' + \mathbf{c}' - \mathbf{I} + \alpha(\mathbf{c}' - \mathbf{I})^2 = 0 \tag{13}$$

where $Re_m = \rho U_0 w/\mu$, $Wi_m = \frac{\lambda U_0}{w} = Wi/2$, $\mu_s' = \mu_s/\mu$, $\mu_p' = \mu_p/\mu$, and U_0 and w are the characteristic velocity and length respectively, i.e., the average flow velocity and channel width. Hereinafter, the dimensionless variables in equations are written without apostrophe.

Non-slip boundary conditions are imposed on the rigid walls and on the particle boundary,

$$\mathbf{u} = \mathbf{0} \text{ on } \Gamma_1 \text{ and } \Gamma_3 \tag{14}$$

$$\mathbf{u} = \mathbf{u}_p + \boldsymbol{\omega}_z \times (\mathbf{x} - \mathbf{x}_p) \text{ on } \Gamma_5(t) \tag{15}$$

A parabolic velocity profile is imposed on Γ_2 with average velocity 1, i.e., $u_x = \frac{3}{2}(1-2y)^2$, and $u_y = 0$. $p\mathbf{n} = \mathbf{0}$ is imposed on Γ_4. The translational and rotational velocity of particle is governed by Newton's second law and Euler's equation on $\Gamma_5(t)$ respectively,

$$m_p \frac{d\mathbf{u}_p}{dt} = \int \boldsymbol{\sigma} \cdot \mathbf{n} \mathrm{d}\Gamma \tag{16}$$

$$I_p \frac{d\boldsymbol{\omega}_p}{dt} = \int (\mathbf{x} - \mathbf{x_p}) \times (\boldsymbol{\sigma} \cdot \mathbf{n}) \mathrm{d}\Gamma \tag{17}$$

where $m_p = \frac{\pi d^2 \rho U_0}{4\mu w}$ and $I_p = \frac{d^2}{8w^2} m_p$ are the dimensionless mass and moment of inertia of particle. The dimensionless particle center $\mathbf{x_p}$ is computed from

$$\frac{d\mathbf{x_p}}{dt} = \mathbf{u}_p \tag{18}$$

Due to the difficulty in numerical convergence at relatively high *Wi*, the constitutive equation is transformed to equivalent equations in terms of log conformation tensor **s**, which is defined as

$$\mathbf{s} = log(\mathbf{c}) \tag{19}$$

To decomposition of the velocity gradient into extensional and rotational components, a matrix decomposition, which is approved by Fattal and Kupferman (2004), is used the Giesekus constitutive equation is transformed to

$$\frac{\partial \mathbf{s}}{\partial t} + \mathbf{u} \cdot \nabla \boldsymbol{s} = g(\nabla \mathbf{u}^T, \mathbf{s}) \tag{20}$$

This log-conformation method is to overcome a stability/stiffness problem associated with the balance between stress advection and stress amplification, and to guarantee positive definiteness of the recovered conformation tensor (Guénette et al. 2008; Afonso et al. 2011).

The coupled fluid and particle equations will be numerically solved using the Arbitrary Lagrangian-Eulerian (ALE) method with a moving, unstructured finite element mesh (Hu et al. 2001). In an ALE formulation, the material time derivative of velocity at a given point ***x*** in the physical domain and at a time instant *t* is written as

$$\frac{D}{Dt}\mathbf{u}(\mathbf{x}, t) = \frac{\partial \mathbf{u}}{\partial t} + (\mathbf{u} - \hat{\mathbf{u}}) \cdot \nabla \mathbf{u} \tag{21}$$

where

$$\frac{\partial}{\partial t}\mathbf{u}(\mathbf{x}, t) = \frac{\partial}{\partial t}\mathbf{u}[\mathbf{x}(\boldsymbol{\chi}, t), t] \tag{22}$$

is described in the referential domain coordinate $\boldsymbol{\chi}$. The function $\mathbf{x}(\boldsymbol{\chi}, t)$ can be viewed as a mapping from the fixed referential domain to the physical domain. The mesh velocity (velocity of the domain) $\hat{\mathbf{u}}$ is defined as

$$\frac{d}{dt}\mathbf{x}(\boldsymbol{\chi}, t) = \hat{\mathbf{u}} \tag{23}$$

When the mesh velocity coincides with the velocity of particle in physical domain, $\hat{\mathbf{u}} = \mathbf{u}$, and the referential time derivative recovers the Lagrangian time derivative. When the referential domain coincides with the physical domain at the current time $\boldsymbol{\chi} = \mathbf{x}$, the referential time derivative reduces to the local Eulerian time derivative with $\hat{\mathbf{u}} = 0$.

The mesh velocity $\hat{\mathbf{u}}$ is governed by Laplace equation,

$$\nabla \cdot (\varepsilon \nabla \hat{\mathbf{u}}) = 0 \tag{24}$$

where ε is the inverse of the local element volume.

$$\hat{\mathbf{u}} = 0 \text{ on } \Gamma_1 \text{ to } \Gamma_4 \tag{25}$$

$$\hat{\mathbf{u}} = \mathbf{u}_p \text{ on } \Gamma_5(t) \tag{26}$$

Once the mesh quality is below a critical value 0.5 due to the distortion of the moving particle, a new mesh will be generated upon which the solution on the old mesh is projected. At each time step, the moving mesh and the particle's motion are updated explicitly, while the flow field, particle velocity, and mesh velocity are solved implicitly. The ALE method is implemented in COMSOL® using the built-in finite-element-method (FEM)-based functions, which are controlled by custom-written MATLAB® scripts. In this study, quadratic triangular elements are generated in fluid domains. A finer mesh is created around the particles to accurately capture the nearby flow field for precise calculation of the force and torque exerting on each particle. The total element number is typically around 16,000 to obtain converged and mesh-independent results.

6.3.2 Code validation

Fig. 2 compares the predicted lateral particle position, Y_p, (normalized by the channel width) vs. time, t, (dimensionless) with the result of Trofa et al. (2015) under identical conditions (i.e., a 2D particle motion in a straight channel with blockage ratio $\beta=d/w=0.1$, $\alpha=0.2$, $\mu_s/\mu_p = 0.1$, neutral buoyant, $Re_m=1$, and $Wi_m=1$). The particle position Y_p starts at 0.3, where 0 indicates the center and 0.5 indicates the channel wall. They are predicted to migrate towards the channel center with a close agreement.

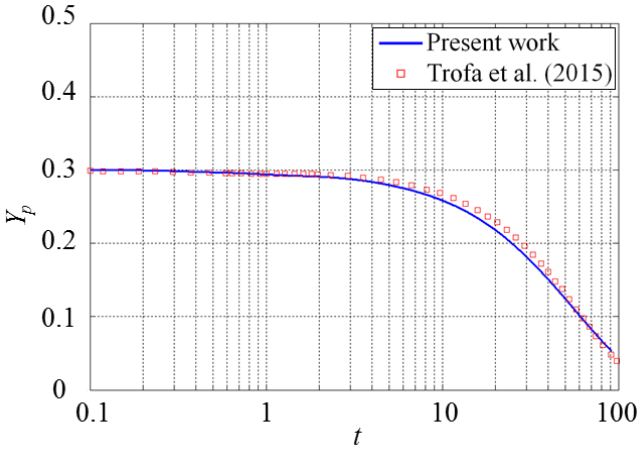

Fig. 2. Code validation for case Y_{p0}=0.3, β=0.1, α=0.2, $\mu_s/\mu_p = 0.1$, Re_m=1, and Wi_m=1

6.4 Results and discussion

6.4.1 Effects of particle size (β) and flow rate (Wi)

Fig. 3 shows the focusing patterns of the 3.1, 4.8, and 9.9 μm particles in the 1000 ppm PEO solution through the 40 μm-deep microchannel. The red dashed box highlights the region to be used as cropped image in this and the following figures. As the flow rate grows, Re and *Wi* both increase (see the labeled values in fig. 3). In a large range of *Wi*, the 3.1 μm particles are barely focused to the center. It indicates a very weak elasto-inertial effect on small particles (β=0.07) in a near-square channel. For the 4.8 and 9.9 μm particles, the focusing at center and corner equilibrium positions are observed at low *Wi*=3.8. With *Wi* increasing to 11.3, the corner equilibrium positions disappears for both sizes of particles due to the stronger wall lift force (Di 2009). But the focusing of the 9.9 μm particles focusing improves dramatically. The focusing of large particles is better than the small ones, which agrees with previous observation (Seo et al. 2014). At *Wi* = 37.8, a clear transition from center equilibrium position to two off-center ones is

observed for the 9.9 μm particles. Three corresponding probability distribution function (PDF) plots are provided for different particles respectively at *Wi* = 37.8. Invisible from the superimposed image, the PDF of 4.8 μm particles shows three peaks, a center one and two off-center ones, although there are particles between these peaks. For the 3.1 μm particles, the probability of particles in the center is higher than that of particles close to the wall. When *Wi* reaches 75.6, the particle positions barely vary.

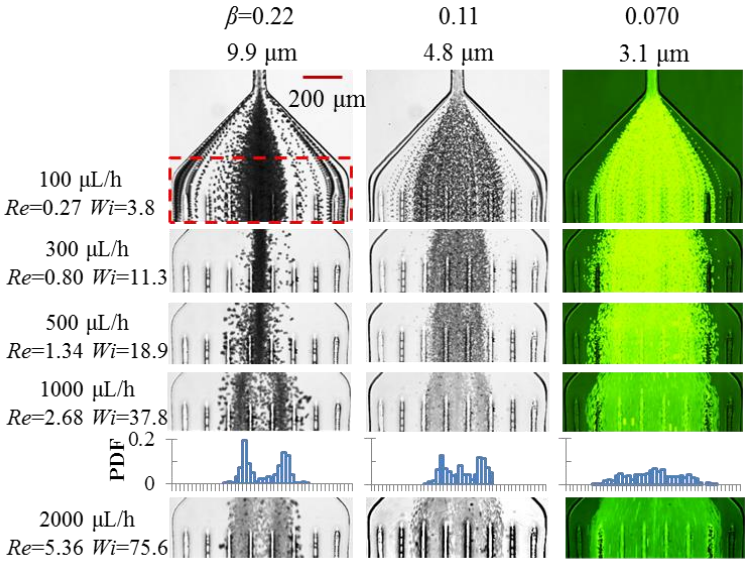

Fig. 3. Focusing patterns of the 3.1, 4.8, and 9.9 μm particles in the 1000 ppm PEO solution through the 40 μm-deep microchannel at different flow rates. At 1000 μL/h, PDF plots are provided for different particles. The red dashed box highlights the region to be used as cropped image in this and the following figures if applicable.

It is concluded that the focusing equilibrium positions is highly dependent on the blockage ratio (particle size). Because the elastic lift force is proportional to the third order of particle size (Tehrani 1996), $\mathbf{F}_{eL} \sim d^3 \nabla N_1$, the small particle is much more weakly deflected by the elastic lift as compared to large particles. In addition, the elasto-inertial focusing is not monotonously affected by the flow rate (*Wi*). As fig. 3 shows, the best

center-focusing of the 9.9 μm particles happens at 300 μL/h (*Wi*=11.3), and it is worse at 500 μL/h (*Wi*=18.9). It is noticed that the equilibrium positions becomes complicated at high flow rate (*Wi*) as discussed in the PDF plot in Fig. 3, i.e., the 9.9 μm particles have two off-center positions and the 4.8 μm particles show three peaks. We speculate that this is a result of the competition between the elastic lift and the shear-induced inertial lift. The elastic lift force can be expressed as $\mathbf{F}_{eL} \sim \lambda_e (d/w)^3 Q^3$ (Lu et al. 2015d), and the shear-induced inertial lift force is given by $\mathbf{F}_{iL\_s} \sim \rho (d/w)^4 Q^2$ (Asmolov 1999) which drives particle away from the channel center. $\mathbf{F}_{iL\_s}$ is negligible at low flow rate (*Re*) but until *Re* is higher than one. And the inertial lift is more sensitive to particle size than the elastic lift force, i.e., it is proportional to the forth order of particle diameter while the elastic lift is proportional to the third order. So the 9.9 μm particles starts to be deflected away from the center at high flow rate (*Re*= 2.68), while the shear-induced inertial lift is not able to eliminate the center particle equilibrium position for the other two smaller particles.

6.4.2 Effect of channel aspect ratio (*AR*)

The channel aspect ratio (*AR*) plays a significant role on the elasto-inertial particle equilibrium positions. Fig. 4 shows the focusing pattern of the three types of particles at 300 μL/h in the 50 μm-wide channels with *AR* varying from 0.5 to 3.3. PDF plots of 9.9 μm particles are presented. At *AR*=0.5, Corner equilibrium positions exist for both 9.9 and 4.8 μm particles. The 3.1 μm particles (β=0.05) are barely focused to any equilibrium positions. The center focusing of all particles are weak at low *AR* channel. At *AR*=1.25,

the center focusing is better than that at *AR*=0.5. It also shows a trend that larger particles have stronger focusing effect. At *AR*=2, the particles are focused to off-center equilibrium positions. Therefore, a size-based particle separation can be achieved between 9.9 and 3.1 μm particles under this condition. At *AR*=3.3, three equilibrium positions are observed for all of the particles, with the center one reappearing. It is observed that the three focusing equilibrium positions of 9.9, 4.8, and 3.1 (β=0.13) μm particles are similar. Accordingly, the effect of blockage ratio is less significant on the equilibrium positions at high-*AR* channel when β is no less than 0.13. In another word, the differences of particle positions between particles of different sizes decrease with rising *AR*. The particle separation cannot be achieved in high-*AR* channels (*AR*≥3.3) due to similar equilibrium positions.

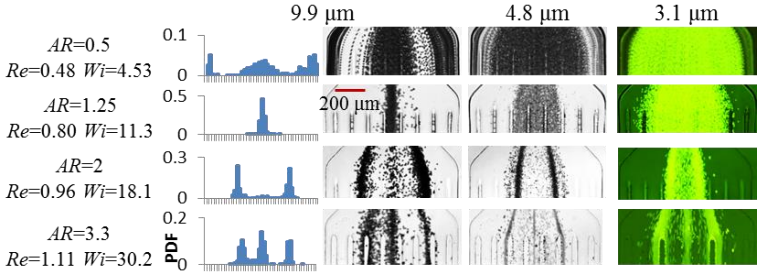

Fig. 4. Focusing patterns of *AR* effect for the 3.1, 4.8, and 9.9 μm particles in the 1000 ppm PEO solution at 300 μL/h. The PDF plots show the positions of 9.9 μm particles.

We have also studied the flow rate effect on the particle focusing in channel *AR*=0.5, 2, and 3 (see Fig. S1-3 in the Supplementary Material). At *AR*=0.5, the smallest particles can also be focused at the corner equilibrium positions. The corner equilibrium positions exist even at 500 μL/h. At *AR*=1.25, the corner equilibrium positions can be observed at 100μL/h only for 9.9 and 4.8 μm particles. At *AR*=2, the corner equilibrium

positions are observed only for 9.9 μm particles at 100μL/h. At *AR*=3.3, no corner equilibrium positions appear. Therefore, the lower *AR* and larger size of particles lead to the higher possibility of corner equilibrium positions. In addition, particles in channel of *AR*=0.5 are always able to reach the channel core despite of strong or weak center focusing. But at high *AR*≥2, only off-center equilibrium positions can be seen at moderate ranges of flow rate. With the increase in flow rate, 4.8 μm particles at *AR*=2 experience first a transition from single center equilibrium position (at 100μL/h) to dual off-center equilibrium positions (at 300μL/h) and then to triple equilibrium positions (at 500μL/h) at both the centerline and two sides. This is consistent with our previous study of 4.2 μm particles under similar condition (Lu et al. 2015d).

It should be noticed that the mechanisms of particle vacancy in the channel core region are different for high *AR* channel at low flow rate (*Re*<1) and the 9.9 μm particles at high flow rate (*Re*>1). As stated above, the latter case (*Re*>1, in near-squared channel) happens due to the nontrivial shear-induced inertial lift. However, the former one (*Re*<1, in high *AR* channel) results from a dominated elastic lift. Different from the square channel, in which there are one center and four corner elastic equilibrium positions, the elastic lift is too weak to deflect particles to the corner equilibrium positions in high *AR* channel under most conditions. And the elastic lift in high *AR* channel is able to drive particle to two off-center equilibrium positions between the center and walls in a large of flow rate (*Wi*). Based on the trend of two off-center equilibrium positions with respect to particle size (β), a size based separation is presented in the following paragraph.

Fig. 5 shows the size based separation between 9.9 and 3.1 μm particles at 200 μL/h at *AR*=2. Calculated from the PDF plot, 95.4% 3.1 μm particles are in the region with normalized lateral position from 0.29 to 0.73, out of which 95.6% 9.9 μm particles distribute. Huang et al. (1997) and Liu et al. (2015) stated that larger particle has greater deflection to the wall due to enhanced compressive normal stress at the near-center side of the particle. The 9.9 μm particles with larger blockage ratio deform the Poiseuille flow more intensively, resulting to a more enhanced compressive normal stress at the near-center side.

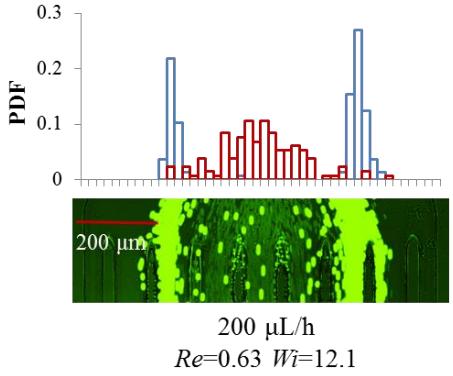

Fig. 5. Particle separation between 3.1 and 9.9 μm particles in the 1000 ppm PEO solution at 200 μL/h at *AR*=2. In the PDF plot, the blue bars indicate 9.9 μm particles and the red bars indicate 3.1 μm particles.

6.4.3 Effects of polymer type and shear-thinning

Fig. 6 shows the effect of polymer type of 9.9 μm particles in the PEO, PVP and PAA solutions at comparable *Wi* in low aspect ratio channels (*AR*=0.5 and 0.15). Due to the complicated mechanisms of elasto-inertial effect in different non-Newtonian solutions, we studied the polymer type effect from the near-slit microchannels. With *AR*=0.15, the channel can be nearly considered as a slit channel. Three types of solutions

were prepared at different concentrations to match the effective relaxation time. Different flow rates were chosen to match the *Wi* number. In the Newtonian fluid, weak focusing effect were observed for both channels because of inertial wall lift. The results in all three non-Newtonian solutions shows three equilibrium positions, one in the center and two near the walls, at similar *Wi* from 6.67 to 8.67 at *AR*=0.5. Due to the extremely high viscosity and hence low *Re*, particles are able to migrate to the wall in the PVP solution at 3000 µL/h. At such high flow rate, the wall equilibrium positions disappear in the PAA and PEO solutions resulting from the growing inertial wall lift. However, in the near-slit channel, the wall equilibrium positions only show in PAA solution. It is also noticed that the center focusing of PAA solution are weaker than those of PEO and PVP solutions in both channels. The 2D numerical results of different constitutive equations are provided in the later part to analysis the mechanism of the experimental differences between the PEO/PVP and the PAA solutions qualitatively.

With a further observation of the wall equilibrium positions at *AR*=0.5, differences are found between the PAA with the other two solutions. In the PAA solution, particles near the wall are all well focused. It indicates that all particles at the near-wall positions are in the same focal plane. However, in both PEO and PVP solutions, some particles are well focused while others are not as shown in the zoom-in image (image taken in the PEO solution) in fig. 6. In experiment, two focal planes were confirmed by adjusting the height of lens. After an adjustment of the focal plane about 70 µm, the previous blurry/out-of-focused ones could be well focused and the previous focused ones became blurry. It indicates that the near-wall particles are located near the channel

corners in the PEO and PVP solutions. Because the near-slit channel is close to an ideal 2D channel which has no corners, the corner positions vanish at *AR*=0.15 in the PEO and PVP solutions.

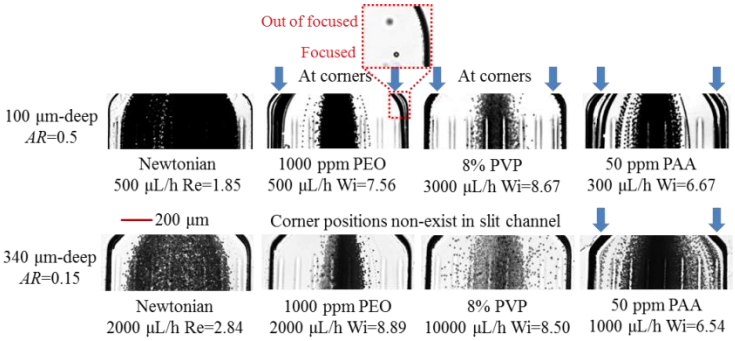

Fig. 6. Experimental results of 9.9 μm particles in the Newtonian, PEO, PVP, and PAA solutions with *AR*=0.5 (the first row) and 0.15 (the second row). The arrows above images indicate the existence of particles near the wall. At *AR*=0.5, wall equilibrium positions are observed for all non-Newtonian solutions. However in the near-slit channel (*AR*=0.15), they only exist for PAA solution. A snapshot image near the wall is provided for the PEO solution to illustrate the particle focal planes at *AR*=0.5.

It is believed that the weaker center-focusing and wall equilibrium positions in the near-slit channel result from the shear-thinning effect of PAA solution. The result of wall equilibrium positions looks different from previous work in PAA solution with highly concentrated glycerol (Leshansky et al. 2007), which only showed center-focusing in a slit channel. Fig. 7 shows the results of PAA solutions with different glycerol concentrations to study the deviation and shear-thinning effect. The viscosities of 23w% and 76w% glycerol are 2 and 40 mPa·s respectively (Segur and Oberstar 1951). The shear viscosity of the 50 ppm PAA solution varies from 30 to 1.5 mPa·s over the range of shear rates 1-5000 s^{-1} (Galindo-Rosales et al. 2012). By a coarse estimation of simple summation of the two viscosity values of PAA and glycerol solutions at the same shear

rate, The shear viscosity of the 50 ppm PAA solution with 23w% glycerol varies from 32 to 3.5 mPa·s, and that of 76w% glycerol varies from 70 to 41.5 mPa·s over the range of shear rates 1-5000 s^{-1}. Thus the shear-thinning effect of the PAA solution decreases with rising glycerol concentration. Compared with the 0% glycerol PAA solution, the 23w% glycerol solution has fewer particles migrating to the wall equilibrium positions. We use narrower arrows to distinguish them. Moreover, no particles are observed near the wall in the 76w% glycerol solution. Meanwhile, the center-focusing in the two glycerol solutions are also better than the pure PAA solution. The shear viscosity ratio at shear rate 1 s^{-1} and 5000 s^{-1} in the three solutions are 20, 9.1, and 1.7 respectively. The weaker shear-thinning effect, the better elastic center-focusing the PAA solution has. Therefore, we conclude that the shear-thinning effect suppresses the elastic lift and deflects particle away from the center.

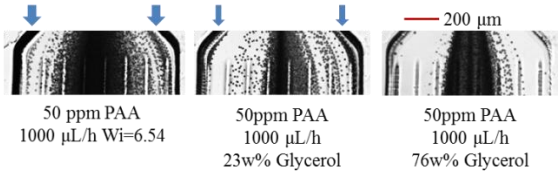

Fig. 7. Shear-thinning effect in 50 ppm PAA solutions in near-slit channel (*AR*=0.15) for 9.9 µm particles. The glycerol concentrations in the images from left to right are 0, 23wt%, and 76wt%. The arrows above images indicate the existence of particles near the wall. The thickness of the arrow corresponds to the amount of particles near the wall qualitatively.

Fig. 8 presents the 2D numerical results of 10 µm particles for Newtonian, OB and Giesekus models. Because of the convergence problem at relatively high *Wi*, the relaxation time in the model was chosen as the Zimm relaxation time, $\lambda_{Zimm} = 0.34ms$, of the 1000 ppm PEO solutions as provided in Supplementary Material. With comparable

average speed and the same channel width with experiment, we get Re_m=0.6 Wi_m=0.2 (corresponding to experimental Wi=0.4). Although the Wi in model is one order of magnitude smaller than that in experiment, previous elasto-focusing studies have demonstrated that numerical result with much lower Wi (Li 2015) and experimental result (Leshansky 2007) agrees with each other qualitatively. In the plot, Y_p=0 corresponds to the centerline and Y_p=0.5 corresponds to the wall. The closest position of particle to the wall is at Y_p=0.4, due to d/w=0.2.

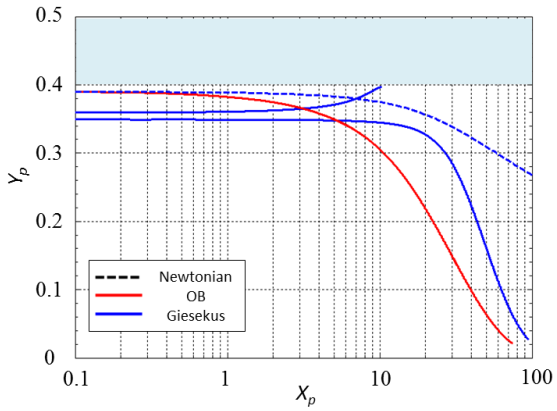

Fig. 8. Numerical (plots) and experimental (superimposed images) results for different fluids. The numerical result of Newtonian model is compared to the experimental result of Newtonian solution, the OB model is compared to the PEO and PVP solution, and Giesekus model is compared to the PAA solution.

The particle trajectory (dash line) of Newtonian model starts at Y_p=0.39, and migrates to the center slower as compared to other models. Finally the particle reaches to the equilibrium position at Y_p=0.22 if the channel is long enough. The numerical result over-predicts the particle migration as compared with experiment, where particles in Newtonian solution have a weak center focusing. The particle trajectory of OB model starts at Y_p=0.39 and migrates to the center at the highest speed as compared to other

models. The center focusing trends in the modelling and experiment in the PEO and PVP solutions are consistent, although the numerical result over-predicts the particle migration as well. Two trajectories of Giesekus model were predicted at Y_p=0.35 and 0.36, one of which moves to the center while the other one migrates to the channel wall. The wall and center equilibrium positions are consistent with experiment in pure PAA solution. As compared with OB model, the one to the center has lower migration speed. It agrees with the experimental trend that the center focusing of the PEO/PVP solution is better than that of PAA solution. Therefore loosely speaking, the OB model is likely to qualitatively predict the center focusing trend of the PEO and PVP solution, and the Giesekus model can predict both of the center and wall focusing trends of PAA solutions in the near-slit channel. For the numerical over-prediction on the migration to the experiment, the main reason we speculate is the deviation of particle geometry, which is an infinite long cylinder in the modeling but is a sphere in the experiment.

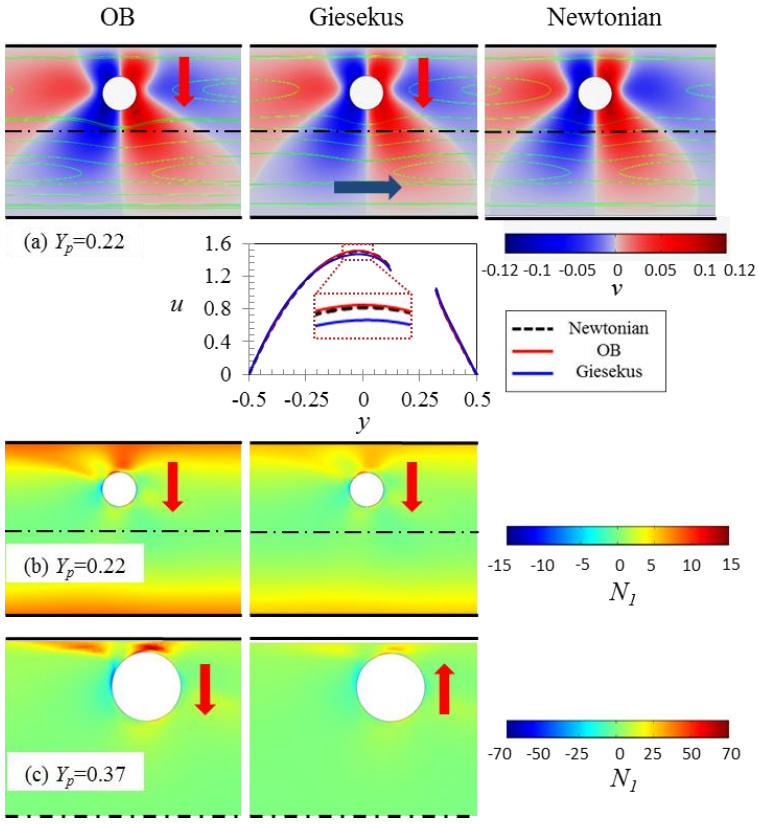

Fig. 9. Flow field around the particle in a channel with OB model (first column), Giesekus model (second column), and Newtonian model (last column). The dark blue arrow indicates the flow direction and the red ones indicate the particle lateral migration direction. The background color (a) shows *v*, the flow velocity in y-coordinate at Y_p=0.22, and the green streamlines (a) are plotted in the frame of reference moving with the particle velocity in x-coordinate. The velocity, *u*, profiles (a) are plotted in y direction at $x=X_p$ for different models. The distributions of first normal stress difference, N_1, in transient OB and Giesekus models at Y_p=0.22 (b) and 0.37 (c) respectively

Fig. 9(a) shows the flow field of transient OB, Giesekus and Newtonian models when particles reach the Newtonian equilibrium position, Y_p=0.22. The dark blue arrow indicates the flow direction and the red ones indicate the particle lateral migration direction. The background color shows *v*, the flow velocity in y-coordinate. The green streamlines are plotted in the frame of reference moving with the particle velocity in x-

coordinate. In all three cases, several streamlines are reversed, which indicate a particle-induced convection along the flow direction (Zurita-Gotor et al. 2007). The velocity, u, profiles are plotted in y direction at $x=X_p$ for different models. In general, the flow fields of three models are similar, except that the velocity of Giesekus at the peak is slightly smaller. Fig. 9(b) and (c) show the distributions of first normal stress difference, N_1, in the OB and Giesekus models at Y_p=0.22 and 0.37 respectively. At Y_p=0.22, both models predict particle migration to the center. But at Y_p=0.37, particle in Giesekus model migrates to the wall. The Newtonian case is needless due to null N_1. Under the same range of color bar, N_1 of OB model is much larger than that of Giesekus model. This is consistent with previous work (Li et al. 2015), which states that the shear-thinning property of Giesekus model reduces the elastic force. Experimentally, it explains the weaker focusing in the PAA solution than the PEO and PVP solutions. We also speculate that the key factor of the wall equilibrium position for Giesekus model and experimental result in PAA solution is the strong shear-thinning effect, which restrains the first normal stress difference and hence the elastic lift, and deflects the particle away from the center. In addition, we observe that a wake of the first normal stress difference exists at the upper-left of the particle in each case of (b) and (c). It indicates the memory effect on the normal stress of non-Newtonian fluid, which leaves a negative wake behind the particle that needs time to be recovered.

6.5 Conclusions

We have studies the elasto-inertial particle focusing systematically in terms of various parameters. Multiple equilibrium positions (center and off-center) are observed in the near-square straight channel in the PEO solution. The larger particles have stronger center focusing. In the *AR* effect study, it has been found that the particle size (blockage ratio) plays a less significant role on the particle focusing equilibrium position with the increasing *AR* in the PEO solution. At *AR*=3.3, those positions for 3.1 and 9.9 μm particles are similar at different flow rates. For 9.9 μm particles at 300 μL/h, an interesting trend of *AR* effect is observed that with AR increasing from 0.5 to 3.3, the multiple equilibrium positions (center and corners) shift to one center position, then to two off-center positions, and finally to multiple equilibrium positions (center and off-centers, but which are not at corners) again. Meanwhile, the corner equilibrium positions appear more easily in the lower *AR* channel and for larger size of particles. Guiding from the *AR* effect, a size-based particle separation is achieved in the channel with *AR*=2 at moderate flow rate.

In addition, polymer types are studied in low *AR* channel and compared with different numerical models. The center focusing in the PAA solution with strong shear-thinning effect is weaker than those in the PEO and PVP solution with no or very weak shear-thinning effect. At *AR*=0.5, it is found that the near-wall equilibrium positions for the PAA and PEO/PVP solutions are different. In the PAA solution, particles near the wall are all located in one certain focal plane, while in the PEO/PVP solutions particles are located at corner positions in two focal planes. At *AR*=0.15, the near-slit channel, the wall equilibrium positions only exist in PAA solution. Further experiments of varied

glycerol concentrations in the PAA solutions in near-slit channels have demonstrated that the shear-thinning effect of the pure PAA solution inhibits the elastic lift and deflects particles away from the center towards the walls. The 2D numerical studies of the particle motion via Oldroyd-B and Giesekus models qualitatively consistent with our experimental observations of the viscoelastic and shear thinning effects on the elasto-inertial particle focusing. The shear-thinning effect of the Giesekus model is able to reduce the normal stress difference and hence the elastic lift force. The OB model without shear-thinning effect successfully predicts the trend of particle center focusing in the PEO and PVP solutions in the near-slit channel. And the Giesekus model is speculated more representative to predict the wall and center focusing trends in the PAA solution. In the numerical flow study, the flow fields look similar between the Newtonian, OB and Giesekus models. A negative wake of the first normal stress difference appears behind the particle in the transient OB and Giesekus models.

Reference

Afonso AM, Oliveira PJ, Pinho FT, Alves MA (2011) Dynamics of high-Deborah-number entry flows: a numerical study. Journal of Fluid Mechanics 677:272-304

Asmolov ES (1999) The inertial lift on a spherical particle in a plane Poiseuille flow at large channel Reynolds number. Journal of Fluid Mechanics 381:63-87

Campo-Deaño L, Galindo-Rosales FJ, Pinho FT, Alves MA, Oliveira MS (2011) Flow of low viscosity Boger fluids through a microfluidic hyperbolic contraction. Journal of Non-Newtonian Fluid Mechanics 166(21):1286-96

Choi S, Park JK (2007) Continuous hydrophoretic separation and sizing of microparticles using slanted obstacles in a microchannel. Lab on a Chip 7(7):890-7

Cox RG and Brenner H (1968) The lateral migration of solid particles in Poiseuille flow—I Theory. Chemical Engineering Science 23(2):147-73.

Del Giudice F, D'Avino G, Greco F, Netti PA, Maffettone PL (2015) Effect of fluid rheology on particle migration in a square-shaped microchannel. Microfluidics and Nanofluidics 19(1):95-104

Del Giudice F, Romeo G, D'Avino G, Greco F, Netti PA, Maffettone PL (2013) Particle alignment in a viscoelastic liquid flowing in a square-shaped microchannel. Lab on a Chip 13(21):4263-71

Di Carlo D (2009) Inertial microfluidics. Lab on a Chip 9(21):3038-46.

Ding X, Li P, Lin SC, Stratton ZS, Nama N, Guo F, Slotcavage D, Mao X, Shi J, Costanzo F, Huang TJ (2013) Surface acoustic wave microfluidics. Lab on a Chip 13(18):3626-49

Dittrich PS, Manz A (2006) Lab-on-a-chip: microfluidics in drug discovery. Nature Reviews Drug Discovery 5(3):210-8

DuBose J, Lu X, Patel S, Qian S, Joo SW, Xuan X (2014) Microfluidic electrical sorting of particles based on shape in a spiral microchannel. Biomicrofluidics 8(1):014101

Fattal R, Kupferman R (2004) Constitutive laws for the matrix-logarithm of the conformation tensor. Journal of Non-Newtonian Fluid Mechanics 123(2):281-5

Galindo-Rosales FJ, Campo-Deaño L, Pinho FT, Van Bokhorst E, Hamersma PJ, Oliveira MS, Alves MA (2012) Microfluidic systems for the analysis of viscoelastic fluid flow phenomena in porous media. Microfluidics and nanofluidics 12(1-4):485-98

Gauthier F, Goldsmith HL, Mason SG (1971) Particle Motions in Non‐Newtonian Media. II. Poiseuille Flow. Transactions of The Society of Rheology (1957-1977) 15(2):297-330

Guénette R, Fortin A, Kane A, Hétu JF (2008) An adaptive remeshing strategy for viscoelastic fluid flow simulations. Journal of Non-Newtonian Fluid Mechanics 153(1):34-45

Hu HH, Patankar NA, Zhu MY (2001) Direct numerical simulations of fluid–solid systems using the arbitrary Lagrangian–Eulerian technique. Journal of Computational Physics 169(2):427-62.

Huang PY, Feng J, Hu HH, Joseph DD (1997) Direct simulation of the motion of solid particles in Couette and Poiseuille flows of viscoelastic fluids. Journal of Fluid Mechanics 343:73-94.

Huang LR, Cox EC, Austin RH, Sturm JC (2004) Continuous particle separation through deterministic lateral displacement. Science 304(5673):987-90

Huang PY, Joseph DD (2000) Effects of shear thinning on migration of neutrally buoyant particles in pressure driven flow of Newtonian and viscoelastic fluids. Journal of non-newtonian fluid mechanics 90(2):159-85

James DF (2009) Boger fluids. Annual Review of Fluid Mechanics 41:129-42

Jung JH, Lee KH, Lee KS, Ha BH, Oh YS, Sung HJ (2014) Optical separation of droplets on a microfluidic platform. Microfluidics and nanofluidics 16(4):635-44

Kang AR, Ahn SW, Lee SJ, Lee B, Lee SS, Kim JM (2011) Medium viscoelastic effect on particle segregation in concentrated suspensions under rectangular microchannel flows. Korea-Australia Rheology Journal 23(4):247-54

Kang K, Lee SS, Hyun K, Lee SJ, Kim JM (2013) DNA-based highly tunable particle focuser. Nature communications 4

Karnis A, Mason SG (1966) Particle motions in sheared suspensions. XIX. Viscoelastic media. Transactions of The Society of Rheology (1957-1977). 10(2):571-92

Kim JY, Ahn SW, Lee SS, Kim JM (2012) Lateral migration and focusing of colloidal particles and DNA molecules under viscoelastic flow. Lab on a Chip 12(16):2807-14

Kim YW, Yoo JY (2008) The lateral migration of neutrally-buoyant spheres transported through square microchannels. Journal of Micromechanics and Microengineering (6):065015.

Lee EF, Koch DL, Joo YL (2010) Cross-stream forces and velocities of fixed and freely suspended particles in viscoelastic poiseuille flow: Perturbation and numerical analyses. Journal of Non-Newtonian Fluid Mechanics 165(19):1309-27

Leshansky AM, Bransky A, Korin N, Dinnar U (2007) Tunable nonlinear viscoelastic "focusing" in a microfluidic device. Physical review letters 98(23):234501

Li G, McKinley GH, Ardekani AM (2015) Dynamics of particle migration in channel flow of viscoelastic fluids. Journal of Fluid Mechanics 785:486-505

Lim EJ, Ober TJ, Edd JF, Desai SP, Neal D, Bong KW, Doyle PS, McKinley GH, Toner M (2014) Inertio-elastic focusing of bioparticles in microchannels at high throughput. Nature communications 5

Liu C, Xue C, Chen X, Shan L, Tian Y, Hu G (2015) Size-based separation of particles and cells utilizing viscoelastic effects in straight microchannels. Analytical chemistry (12):6041-8

Lu X, Patel S, Zhang M, Joo SW, Qian S, Ogale A, Xuan X (2014) An unexpected particle oscillation for electrophoresis in viscoelastic fluids through a microchannel constriction. Biomicrofluidics 8(2):021802

Lu X, Xuan X (2015a) Inertia-Enhanced Pinched Flow Fractionation. Analytical chemistry 87(8):4560-5

Lu X, Xuan X (2015b) Continuous Microfluidic Particle Separation via Elasto-Inertial Pinched Flow Fractionation. Analytical chemistry 87(12):6389-96

Lu X, Xuan X (2015c) Elasto-Inertial Pinched Flow Fractionation for Continuous Shape-Based Particle Separation. Analytical chemistry 87(22):11523-30

Lu X, Zhu L, Hua RM, Xuan X (2015d) Continuous sheath-free separation of particles by shape in viscoelastic fluids. Applied Physics Letters 107(26):264102

Nam J, Lim H, Kim D, Jung H, Shin S (2012) Continuous separation of microparticles in a microfluidic channel via the elasto-inertial effect of non-Newtonian fluid. Lab on a chip 12(7):1347-54

Rodd LE, Cooper-White JJ, Boger DV, McKinley GH (2007) Role of the elasticity number in the entry flow of dilute polymer solutions in micro-fabricated contraction geometries. Journal of Non-Newtonian Fluid Mechanics 143(2):170-91.

Rodd LE, Scott TP, Boger DV, Cooper-White JJ, McKinley GH (2005) The inertio-elastic planar entry flow of low-viscosity elastic fluids in micro-fabricated geometries. Journal of Non-Newtonian Fluid Mechanics 129(1):1-22

Rodd LE, Scott TP, Boger DV, Cooper-White JJ, McKinley GH (2005) The inertio-elastic planar entry flow of low-viscosity elastic fluids in micro-fabricated geometries. Journal of Non-Newtonian Fluid Mechanics 129(1):1-22

Sajeesh P, Sen AK (2014) Particle separation and sorting in microfluidic devices: a review. Microfluidics and nanofluidics 17(1):1-52

Segur JB, Oberstar HE (1951) Viscosity of glycerol and its aqueous solutions. Industrial & Engineering Chemistry 43(9):2117-20

Seo KW, Kang YJ, Lee SJ (2014) Lateral migration and focusing of microspheres in a microchannel flow of viscoelastic fluids. Physics of Fluids (1994-present) 26(6):063301

Shields IV CW, Reyes CD, López GP (2015) Microfluidic cell sorting: a review of the advances in the separation of cells from debulking to rare cell isolation. Lab on a Chip 15(5):1230-49

Stone HA, Stroock AD, Ajdari A (2004) Engineering flows in small devices: microfluidics toward a lab-on-a-chip. Annu Rev Fluid Mech 36:381-411

Swaminathan VV, Shannon MA, Bashir R (2015) Enhanced sub-micron colloidal particle separation with interdigitated microelectrode arrays using mixed AC/DC dielectrophoretic scheme. Biomedical microdevices 17(2):1-9

Tehrani MA (1996) An experimental study of particle migration in pipe flow of viscoelastic fluids. Journal of Rheology (1978-present) 40(6):1057-77

Trofa M, Vocciante M, D'Avino G, Hulsen MA, Greco F, Maffettone PL (2015) Numerical simulations of the competition between the effects of inertia and

viscoelasticity on particle migration in Poiseuille flow. Computers & Fluids 107:214-23

Villone MM, D'avino G, Hulsen MA, Greco F, Maffettone PL (2011a) Numerical simulations of particle migration in a viscoelastic fluid subjected to Poiseuille flow. Computers & Fluids 42(1):82-91

Villone MM, D'Avino G, Hulsen MA, Greco F, Maffettone PL (2011b) Simulations of viscoelasticity-induced focusing of particles in pressure-driven micro-slit flow. Journal of Non-Newtonian Fluid Mechanics 166(23):1396-405

Villone MM, D'Avino G, Hulsen MA, Greco F, Maffettone PL (2013) Particle motion in square channel flow of a viscoelastic liquid: Migration vs. secondary flows. Journal of Non-Newtonian Fluid Mechanics 195:1-8

Yamada M, Nakashima M, Seki M (2004) Pinched flow fractionation: continuous size separation of particles utilizing a laminar flow profile in a pinched microchannel. Analytical chemistry 76(18):5465-71

Yamada M, Seki M (2005) Hydrodynamic filtration for on-chip particle concentration and classification utilizing microfluidics. Lab on a Chip 5(11):1233-9

Yang S, Lee SS, Ahn SW, Kang K, Shim W, Lee G, Hyun K, Kim JM (2012) Deformability-selective particle entrainment and separation in a rectangular microchannel using medium viscoelasticity. Soft Matter 8(18):5011-9

Zhou Y, Kumar DT, Lu X, Kale A, DuBose J, Song Y, Wang J, Li D, Xuan X (2015) Simultaneous diamagnetic and magnetic particle trapping in ferrofluid microflows via a single permanent magnet. Biomicrofluidics 9(4):044102

Zurita-Gotor M, Bławzdziewicz J, Wajnryb E (2007) Swapping trajectories: A new wall-induced cross-streamline particle migration mechanism in a dilute suspension of spheres. Journal of Fluid Mechanics 592:447-69

CHAPTER SEVEN

ELASTO-INERTIAL PINCHED FLOW FRACTIONATION (eiPFF) FOR CONTINUOUS SHAPE-BASED PARTICLE SEPARATION

Abstract

Shape is an important passive marker in label-free particle and cell separation for chemical, biomedical and environmental applications. We demonstrate herein a continuous-flow shape-based separation of spherical and peanut-shaped rigid particles of equal volume (or equivalent spherical diameter) via elasto-inertial pinched flow fractionation (eiPFF). This microfluidic technique exploits the shape-dependence of the flow-induced elasto-inertial lift (and hence the cross-stream migration) in viscoelastic fluids to increase the displacement of a sheath flow-focused particle mixture for a high-purity separation. The parametric effects on this shape-based particle separation via eiPFF are systematically investigated in terms of five dimensionless numbers. It is found that the separation is strongly affected by the flow rate, fluid elasticity and channel aspect ratio. Interestingly, the elasto-inertial deflection of the peanut particles can be either greater or smaller than that of equally-volumed spherical particles. This phenomenon is speculated to correlate with the rotational effects of peanut particles.

7.1 Introduction

Shape is a fundamental property of particles and cells that can influence their interactions with the environment and determine their functional capabilities.[1] can be an important factor for characterizing cellular biospecies, for instance, prokaryotes are

classified into different groups by shape such as rod-shaped, spiral-shaped and spherical ones.[2] Shape has been found to play a significant role in phagocytosis where macrophages internalize pathogens and airborne particles of various shapes.[3] It can also be used to identify cell cycle stages. For example, budding yeasts undergo shape changes from spheres to bi-spherical twins or larger aggregates during cell division.[4] Moreover, shape is a good indicator of cell states that can provide useful information for disease diagnostics. It has been long known that the shape change of red blood cells is often accompanied with a disease such as sickle-cell disease[5] or malaria.[6] Therefore, shape is an important intrinsic marker for label-free cell and particle sorting, which may find applications in pathogen isolation from biological fluids for disease diagnostics, classification of environmental bacteria and elimination of aggregates from synthesized particles etc.

A variety of microfluidic techniques have thus far been demonstrated to separate particles and cells in continuous flows.[7,8] However, the majority of these techniques are focused on particle separation by size.[9,10] Only until very recently has the particle shape been exploited as a passive sorting marker in a limited number of studies. Sugaya et al.[11] exploited the dissimilar rotation at fluid branch points to separate spherical particles from non-spherical particles and single yeasts from budding yeasts. This hydrodynamic filtration[12] technique requires the use of a network of microchannels. Valero et al.[13] utilized multi-frequency dielectrophoresis to synchronize yeast cell division, which requires the integration of in-channel microelectrodes and also a precise control of the medium electric conductivity. Beech et al.[14] used deterministic lateral displacement[15] to

classify morphologically altered red blood cells based on shape. This technique, which has also been investigated by Zeming et al.[16] for shape-based separation, requires the fabrication of a high-resolution array of posts. Masaeli et al.[17] utilized differential inertial focusing[18] to sort spheres and rods as well as yeast cells at various stages in a long straight microchannel. This separation relies on high flow speed-induced inertial lift and is thus restricted from handling small amount of samples. Recently, our group has used curvature-induced dielectrophoresis (C-iDEP)[19-21] to separate particles by shape in an asymmetric double-spiral microchannel.[22] This electrokinetic method suffers from a low throughput and may be harmful to cells due to potential electrical damages.[23]

In this work we demonstrate the use of a recently developed size-based particle separation technique in viscoelastic fluids,[24,25] which we termed elasto-inertial pinched flow fractionation or eiPFF in short,[26] to continuously separate particles based on shape in straight rectangular microchannels. As illustrated by the schematic (not to scale) in Figure 1, eiPFF exploits the strong size-dependence of the flow-induced elasto-inertial lift (and hence the cross-stream migration) to increase the displacement of a sheath flow-focused particle mixture for a significantly enhanced separation than the traditional steric effects-based PFF.[27,28] We hypothesize that the elasto-inertial lift induced particle migration in viscoelastic fluids are also a function of particle shape, which will be demonstrated in this work by the continuous deflection and separation of spherical and peanut-shaped particles of equal volume. The observations will also be directly compared with those for particles suspended in a Newtonian fluid under identical experimental conditions. Moreover, a systematic study of the parametric effects such as flow rate, fluid

elasticity and channel aspect ratio will be carried out for a comprehensive understanding of the important factors that may impact the shape-based particle separation via eiPFF.

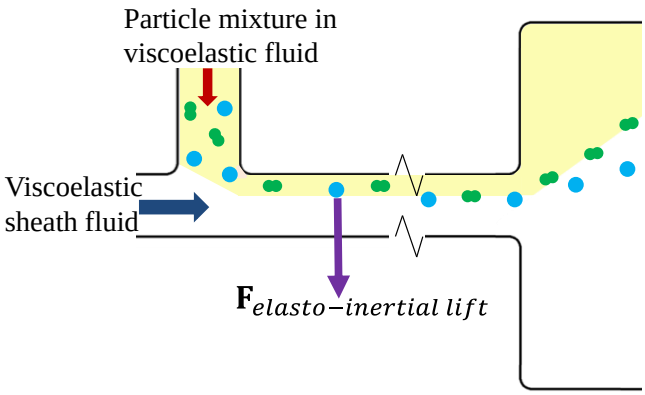

Figure 1 Schematic illustration (not to scale) of the mechanism for shape-based particle separation via eiPFF. The flow-induced elasto-inertial lift force (which can be simply viewed as a combination of elastic lift and inertial lift) in a viscoelastic fluid significantly increases the displacement of a sheath flow-focused mixture of spherical and peanut-shaped particles for a high-purity separation.

7.2 Experimental

7.2.1 Preparation of particle suspensions

Fluorescent spherical polystyrene particles of 4.18 μm diameter (Bangs Laboratories, Inc.) and plain peanut-shaped polystyrene particles of 3.5 μm-diameter/6 μm-length (Magsphere, Inc.) were used to demonstrate the shape-based separation. The peanut particles are obtained by fusing two 3.5 μm-diameter spherical particles, whose overall volume was calculated to be 39.84 μm^3 using the geometry package in COMSOL®. This volume corresponds to an equivalent spherical diameter of 4.23 μm, which deviates from that of the spherical particles by only 1.2%; see a zoom-in picture of both particles in Figure 2(A). The two types of particles were mixed at a 1:1 ratio and re-suspended in water-based Newtonian and non-Newtonian fluids to a final concentration

of about 10^7 particles/ml. The Newtonian fluid was prepared by adding 0.5% (v/v) Tween 20 (Fisher Scientific) to water (Fisher Scientific) to reduce the influences of particle adhesions (to channel walls) and aggregations. The non-Newtonian fluids were prepared by dissolving polyethylene oxide (PEO) powder (Sigma-Aldrich USA, molecular weight $M_w = 2\times10^6$ Da) into water at a range of concentrations. Tween 20 was also added to them at 0.5% (v/v) for a fair comparison of particle separation in between water and PEO solutions.

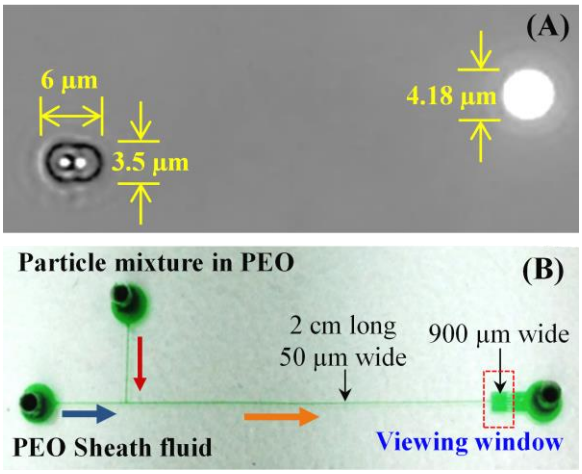

Figure 2 (A) shows a zoom-in view of one plain peanut-shaped particle (left, black) and one fluorescent spherical particle (right, white) of equal volume; (B) shows a top-view picture of the asymmetric T-shaped microchannel (filled with green food dye for clarity, adapted from Figure 1 in ref. 26 with permission from American Chemical Society) used in experiments, where the block arrows indicate the flow directions and the dashed-box highlights the 900 µm-wide expansion region for visualizing particle separation.

Table 1 lists the properties of the prepared PEO solutions at 20 °C (the operation temperature of all experiments). The zero-shear dynamic viscosities, η_0, of 500 ppm, 1000 ppm and 3000 ppm PEO solutions were obtained from the paper of Rodd et al.,[29] which were originally measured in experiments. The viscosities of PEO solutions at other

concentrations were calculated using the viscosity blending equation.[30] The overlap concentration, c^*, was calculated from the expression of Graessley,[31] $c^* = 0.77/[\eta]$ ppm, where the intrinsic viscosity, $[\eta] = 0.072M_w^{0.65} = 897$ ml/g, was given by the Mark-Houwink relation.[29] The effective relaxation times of the prepared PEO solutions were estimated from,[32]

$$\lambda_e = 18\lambda_{Zimm}(c/c^*)^{0.65} \quad (1)$$

where λ_{Zimm} is the relaxation time predicted according to Zimm theory,[33]

$$\lambda_{Zimm} = F\frac{[\eta]M_w\eta_s}{N_A k_B T} \quad (2)$$

In the above the pre-factor, $F = \sum_{i=1}^{\infty} i^{-3\nu} = 0.463$, was estimated from the Remann Zeta function using a solvent quality exponent, $\nu = 0.55$,[29] the solvent (i.e., water) viscosity η_s is equal to 1.0 mPa·s, N_A is the Avogadro's constant, k_B is the Boltzmann's constant, and $T = 293.15$ K is the absolute temperature. The prepared PEO solutions are in the dilute (under 500 ppm) or semi-dilute (beyond 500 ppm) regime, which exhibit a zero or a mild shear-thinning effect as reported in earlier studies.[34-37]

Table 1. Properties of the PEO solutions used in experiments (at 20 °C).

Fluid properties	**PEO concentration (*c*, ppm)**								
	50	100	200	300	500	1000	1500	2000	3000
Density ρ (g/cm^3)	1.0	1.0	1.0	1.0	1.0	1.0	1.0	1.0	1.0
Zero-shear viscosity η_0 (mPa·s)	1.05	1.1	1.2	1.4	1.8	2.3	3.0	4.1	8.3
Overlap concentration c^* (ppm)	858	858	858	858	858	858	858	858	858
Concentration ratio c/c^*	0.06	0.12	0.23	0.35	0.58	1.17	1.75	2.33	3.50
Zimm relaxation time, λ_{Zimm} (ms)	0.34	0.34	0.34	0.34	0.34	0.34	0.34	0.34	0.34
Effective relaxation time, λ_e (ms)	0.96	1.5	2.4	3.1	4.3	6.8	8.8	10.6	13.8

7.2.2 Experimental setup

The standard soft lithography method was used to fabricate microchannels with polydimethylsiloxane (PDMS); see a top-view picture of the channel in Figure 2(B). The details of the fabrication procedure are referred to Lu et al.[26,38] The asymmetric T-shaped microchannel has two 4 mm-long side-branches followed by a 2 cm-long main-branch with a uniform width of 50 μm. At the end of the main-branch there is a 900-μm wide, 2 mm-long expansion for enhancing and visualizing the particle separation. Four depths of channels were fabricated for the purpose of examining the effect of channel aspect ratio on particle separation, which are 15, 25, 40 and 100 μm, respectively. Infusion syringe pumps were used to drive the sheath fluid (New Era Pump Systems, Inc.) and particle mixture (KD Scientific). Particle motion was recorded through an inverted microscope (Nikon Eclipse TE2000U, Nikon Instruments) with a CCD camera (Nikon DS-Qi1Mc) at a frame rate of around 15 Hz. Fluorescent and bright-field lights were simultaneously used in order to visualize both the fluorescent spherical particles and the plain peanut-shaped particles. Images were post-processed using the Nikon imaging software (NIS-Elements AR 3.22). Superimposed particle images were obtained by stacking a sequence of around 800 snapshot images with the maximum and minimum intensity projections for the fluorescent and plain particles, respectively.

7.2.3 Dimensionless numbers

We study the parametric effects on particle separation via eiPFF in terms of five dimensionless numbers.[26] The Reynolds number is defined as the ratio of the inertial force to the viscous force,

$$Re = \frac{\rho V D_h}{\eta_0} = \frac{2\rho Q}{\eta_0 (w+h)} \quad (3)$$

where ρ is the fluid density, V is the average fluid velocity in a rectangular microchannel of width w and height h, $D_h = 2wh/(w+h)$ is the hydraulic diameter, and Q is the volumetric flow rate. The Weissenberg number measures the fluid elasticity effects and is defined as

$$Wi = \lambda_e \dot{\gamma} = \lambda_e \frac{2V}{w} = \frac{2\lambda_e Q}{w^2 h} \quad (4)$$

where $\dot{\gamma}$ is the average fluid shear rate in the microchannel. The elasticity number is defined as the ratio of fluid elasticity to inertia and is hence independent of the flow kinematics,

$$El = \frac{Wi}{Re} = \frac{\lambda_e \eta_0 (w+h)}{\rho w^2 h}. \quad (5)$$

The flow rate ratio between the sheath fluid and particle mixture in the two side-branches measures the sheath flow focusing performance in the main-branch, which affects the particle deflection and dispersion at the channel expansion,

$$\alpha = \frac{Q_{sheath}}{Q_{particle}}. \quad (6)$$

Note that the definitions of *Re* in eq 1 and *Wi* in eq 2 are both based on the total flow rate in the main-branch of the microchannel, i.e., $Q = Q_{sheath} + Q_{particle}$. The channel aspect ratio is the channel width to height ratio,

$$AR = w/h \quad (7)$$

Which, as recently reported,[39] affects the particle focusing position in non-Newtonian fluids through straight microchannels.

7.3 Results and discussion

7.3.1 Effects of fluid elasticity (*Wi*)

Figure 3 compares the shape-based separation of fluorescent spherical particles and plain peanut particles in water (A, $Wi = 0$) and 1000 ppm PEO solution (B, $Wi = 6.35$) through a 25 μm deep microchannel ($AR = 2.0$). The sheath flow rate is 100 μl/h in both experiments and the flow rate ratio between the sheath fluid and particle mixture is fixed at $\alpha = 20$. In the Newtonian water solution, the spherical (appearing white) and peanut (appearing black) particles both move near the channel sidewall and overlap with each other without a visible separation; see the snapshot (left) and superimposed (middle for peanuts and right for spheres) images in Figure 3(A). In contrast, they are both significantly deflected away from the sidewall by the flow-induced elasto-inertial (primarily elastic) lift in the viscoelastic PEO solution. Moreover, as demonstrated in Figure 2(B), the exiting positions of spherical particles are much closer to the channel centerline and are thus clearly separated from the peanut particles with only very few particles scattered in between the two streams.

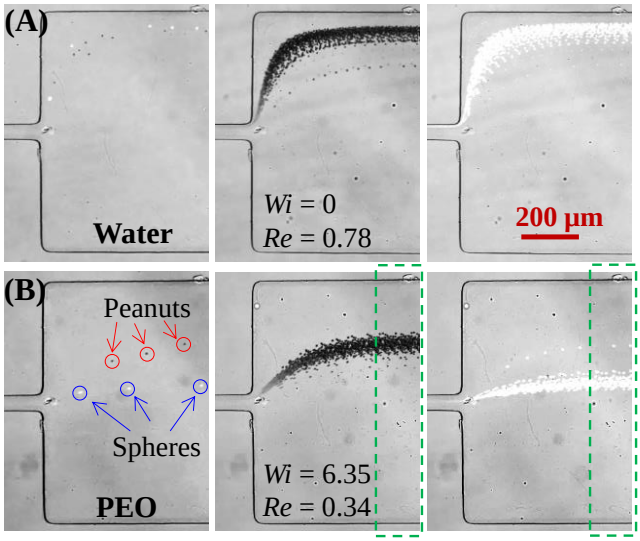

Figure 3 Comparison of shape-based separation of fluorescent spherical (white) and plain peanut-shaped particles (black) in water (A) and 1000 ppm PEO solution (B) through a 25 µm deep microchannel under the sheath flow rate of 100 µl/h and the flow rate ratio of 20. The images in the left, middle and right columns are the snapshot images of both particles, superimposed images of peanut particles, and superimposed images of spherical particles at the channel expansion, respectively. The two dashed boxes in (B) highlight the regions to be used as cropped images in the following figures if applicable. The flow direction is from left to right in all images.

As suggested by the recent work from Masaeli et al.[17], we tracked the orientation of peanut particles in the above two experiments using a high-speed camera (Photron SA-4, Motion Capture Technologies) at a frame rate of 3600/s. Figure 4(A) displays two superimposed images of single peanut particle traveling through the 50 µm-wide main-branch in water (top) and 1000 ppm PEO solution (bottom), respectively. The images were each obtained by superimposing every other frame of a short video, i.e., the time interval between neighboring particle positions on the images is fixed at 1/1800 s. The peanut particle in water seems to undergo a periodic three-dimensional rotation, both in-plane and out-of-plane, which has also been observed by Masaeli et al.[17] In contrast, the

rotation in the PEO solution appears to be primarily in plane and happens at an apparently lower speed than in water.

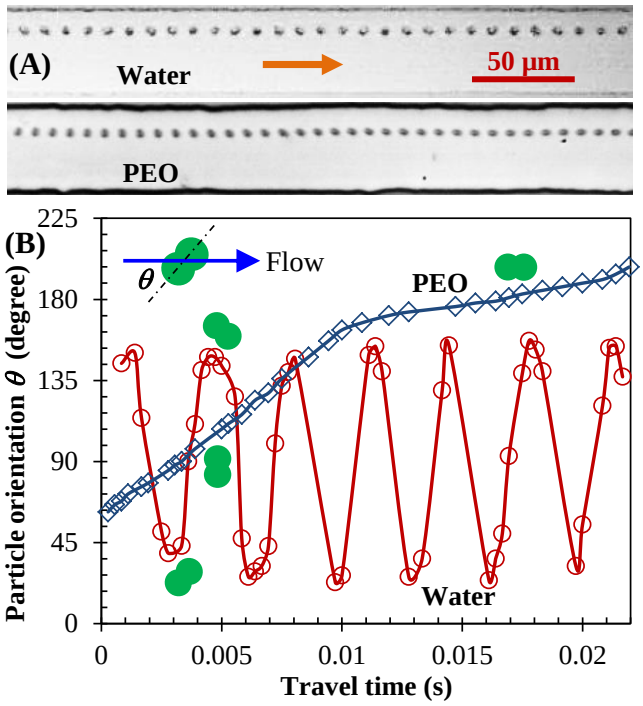

Figure 4 Comparison of the rotation of peanut particles in water and 1000 ppm PEO solution through a 25 µm deep microchannel under a sheath flow rate of 100 µl/h: (A) shows the superimposed images of single peanut particle in water (top) and PEO (bottom), where the time interval between neighboring particle positions is 1/1800 s and the block arrow indicates the particle traveling direction; (B) shows the time-varied orientations of the long axis of peanut particles (markers) with respect to the flow direction (see the definition of angle θ on the schematic) in the two suspending fluids, which were estimated from the images in (A) (note that not all the particle orientations are included in the plot). The schematics of peanut particles on the plot are used to highlight the particle orientations at different angles. The solid lines are used to connect the markers only.

Figure 4(B) compares the time-varied orientations of the long axis of peanut particles (markers) in the two suspending fluids, which were estimated with respect to the flow direction from the top-view images in Figure 4(A). The period of the peanut particle

rotation in water is around 3 ms, which is consistent with the theoretical prediction of the orbit period, T_{orbit}, for an inertialess ellipsoid, [17,40]

$$T_{orbit} = \frac{2\pi}{\dot{\gamma}}\left(\alpha + \frac{1}{\alpha}\right) \quad (8)$$

where $\dot{\gamma}$ is the local fluid shear rate, and α is the particle aspect ratio. Specifically, if it is viewed as an approximate ellipsoid, the peanut particle has an aspect ratio of α = 3.5/6. The local shear rate can be estimated from the average flow velocity at 100 µl/h (i.e., 0.022 m/s) divided by the equivalent spherical diameter of the peanut particle (i.e., 4.23 µm), which gives $\dot{\gamma} = 5201\ s^{-1}$. Substituting these parameters into eq 8 yields an orbit period of T_{orbit} = 2.8 ms for the peanut particle rotation in water, which is at least an order of magnitude shorter than that in PEO. Such a substantially extended period of particle rotation in a viscoelastic solution is consistent with the experimental observation of Bartram et al.[41], who found a significant increase in the period of rotational rods in polyacrylamide (PAA) solution over that predicted by a Newtonian fluid-based theory. Moreover, this difference grows with increasing shear rate due to likely the existence of an elastic restoring torque opposing that from the viscous deformation of the fluid.[41]

It is also noticed in Figure 4(B) that the peanut particle in the PEO solution tends to travel with its long axis aligned towards the flow direction, i.e., 0 or 180 degree orientation. This can be viewed from the slope of the particle orientation vs. time curve, which indicates that the rotational speed is around 10 degree/ms and 2.4 degree/ms when the long axis of the peanut particle is perpendicular (i.e., 90 degree orientation) and parallel to the flow direction, respectively. Such a preferred parallel orientation renders the elasto-inertial lift force more dependent on the shorter dimension of the peanut

particle (i.e., 3.5 μm), which is smaller than the diameter of the spherical particle (i.e., 4.18 μm). Furthermore, the peanut particle experiences a greater drag force due to its larger surface area,[42] yielding a smaller deflection than that of the spherical one as demonstrated in Figure 3.

7.3.2 Effects of fluid inertia (*Re*)

Figure 5 shows the effect of flow rate (in terms of *Re*) on the shape-based separation in water (A) and 1000 ppm PEO solution (B) in a 25 μm deep microchannel. The sheath flow rate is varied from 20 μl/h to 400 μl/h while the flow rate ratio between the sheath fluid and particle mixture is fixed at α = 20. In the Newtonian fluid, the equilibrium positions of spherical (white) and peanut (black) particles both appear to migrate away from the wall slightly with the increase of *Re*. This is a result of the increasing inertial lift force, though weak for small particles at *Re* of order 1, that acts to push particles away from walls.[43,44] However, as seen from Fig. 5(A), there is no particle separation observed in all the tested flow rates (up to 1 ml/h with *Re* = 7.76, image not shown). In contrast, the effect of *Re* on the equilibrium positions and separation of spherical/peanut particles in the PEO solution is much more complicated as demonstrated in Figure 5(B). At the lowest sheath flow rate of 20 μl/h with *Re* = 0.07, each type of particles already attain a much larger deflection than that in water due to the action of the dominant elastic lift force at *Wi* = 1.27. While the deflection of spherical particles (white) is apparently greater than that of peanut particles (black), the two particle streams still partially overlap with each other rendering the separation incomplete. Moreover, there

seems to exist a secondary equilibrium position at the corner of the channel cross-section for spherical particles [highlighted by the dashed arrow on the left-most image in Figure 5(B)] due to the negligible influence of inertial lift.[25,36,45] With the increase of *Re*, the deflection of spherical particles grows while that of peanut particles reduces, leading to an enhanced separation at 60 µl/h. Further increasing *Re* worsens the separation because the two types of particles tend to migrate toward a common equilibrium position due to the increasing dominance of inertial lift over elastic lift.

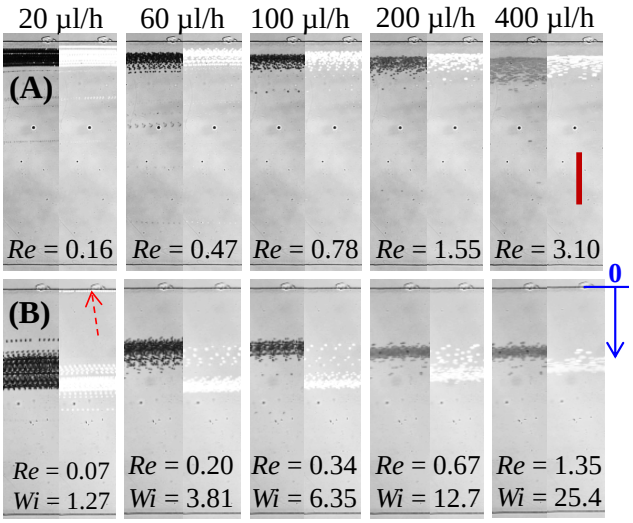

Figure 5 Cropped superimposed images [highlighted by the dashed boxes in Figure 3(B)] illustrating the effects of fluid elasticity (*Wi*) and inertia (*Re*) on the shaped-based separation of fluorescent spherical (white) and plain peanut (black) particles in water (A) and PEO solution (B) in a 25 µm deep microchannel. The sheath flow rate is varied from 20 to 400 µl/h from left to right while the flow rate ratio between the sheath fluid and particle mixture remains at α = 20. The solid arrow on the right-most image in (B) indicates the reference point to which the particle stream positions in Figures 6, 9, and 10 were measured. The dashed arrow on the left-most image in (B) highlights a secondary equilibrium position at the channel corner for spherical particles in the PEO solution at a low flow rate. The scale bar on the right-most image in (A) represents 200 µm.

Figure 6 presents a quantitative comparison of the exiting positions of fluorescent spherical and plain peanut-shaped particles at the channel expansion. The data points

were measured directly from the particle images in Figure 5(B), where the top sidewall of the channel expansion was used as the reference point (see the solid arrow on the right-most image) and the center of each particle trace was used as the measuring point. The best particle separation seems to take place under a sheath flow rate of approximate 75 µl/h, where the deflections of spherical and peanut particles reach the maximum and minimum, respectively. The increase of flow rate beyond 100 µl/h appears to diminish the difference between the two types of particles due to the increasing role of the inertial lift force in eiPFF. The displacements of both particles from the channel sidewall seem to converge to a value of around 300 µm for flow rates greater than 400 µl/h, which is about 1/3 of the half-channel-width away from the channel centerline. This particle focusing position seems consistent with that reported in a recent study,[39] where particles in a PEO solution were observed to migrate toward two positions that are each less than 0.4 times the half-channel-width from the center. It is, however, different from the centerline equilibrium position for particles in Newtonian fluids through rectangular high-*AR* microchannels.[46,47]

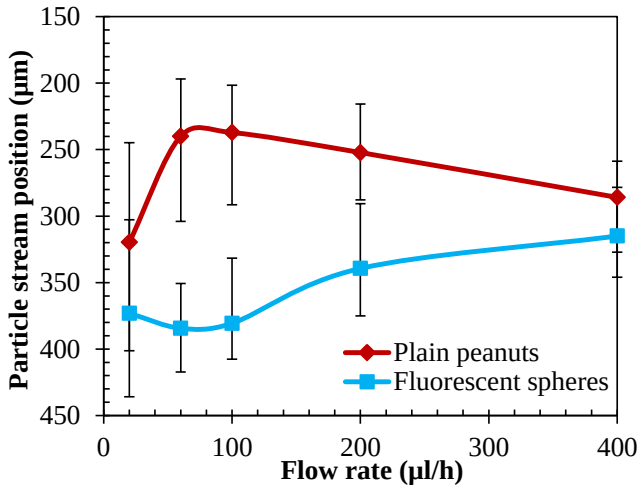

Figure 6 Comparison of the exiting positions of fluorescent spherical and plain peanut particles at the expansion of the main-branch in 1000 ppm PEO solution under various flow rates. All data points (symbols with error bars to encompass the span of each particle stream) were measured directly from the images in Figure 5(B) with reference to the top sidewall of the channel expansion as indicated by the solid arrow therein.

7.3.3 Effects of flow rate ratio, α

Figure 7(A) shows the flow rate ratio effect on the shape-based particle separation via eiPFF in 1000 ppm PEO solution through a 25 μm deep microchannel. The sheath flow rate is fixed at 100 μl/h while the particle mixture flow rate is varied from 20 μl/h (i.e., α = 5) to 2 μl/h (i.e., α = 50). As the total flow rate in the main-branch of the microchannel does not change significantly, *Re* slightly decreases from 0.39 to 0.33 with the increase of α. Meanwhile, *Wi* also decreases slightly from 7.25 to 6.17 to maintain the elasticity number at *El* = 18.8. Therefore, the elastic and inertial lift forces both remain nearly constant in the range of the tested α values, which explains why the deflections of spherical (white) and peanut (black) particles both remain almost unvaried in Figure 7(A). However, a larger α indicates a better focusing of both types of particles at the T-junction

of the microchannel [see Figure 1 and Figure 2(B)],[24-28] which yields a smaller dispersion of either particles and hence an enhanced separation. The separation purity was determined by manually counting the percentages of spherical and peanut particles below and above the dashed-dotted line in Figure 7(A), respectively, using the Nikon imaging software. This line was drawn right in the middle of the two separated particle streams because their center positions are both fixed in the range of the tested flow rate ratios. As seen from Figure 7(B), the separation purity of either type of particles increases with α and is over 90% even for the smallest α of 5. Interestingly, the separation purity of peanut particles is higher than that of spherical particles at all the tested α values due partially to a smaller dispersion, for which the reason is currently unclear.

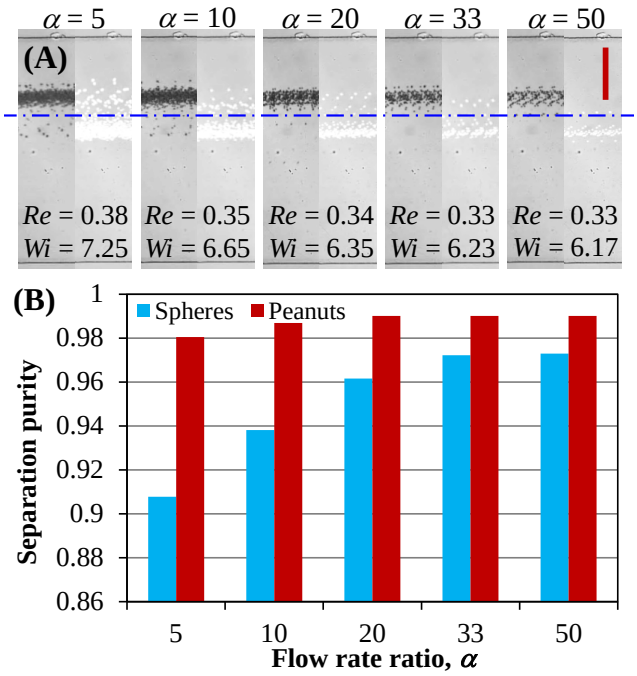

Figure 7 Flow rate ratio effect on the shape-based separation of fluorescent spherical (white) and plain peanut (black) particles via eiPFF in 1000 ppm PEO solution through a 25 μm deep microchannel under a constant 100 μl/h sheath flow rate: (A) shows the cropped superimposed images at the channel expansion, where the dashed-dotted line is

right in the middle of the two separated particle streams; (B) shows the column plot for the measured separation purity (i.e., percentage) of spherical and peanut particles below and above the dashed-dotted line in (A), respectively. The scale bar on the right-most image in (A) represents 200 μm.

7.3.4 Effects of PEO concentration (*El*)

Figure 8 shows the PEO concentration effect on the shape-based particle separation via eiPFF in a 25 μm deep microchannel. The sheath flow rate and flow rate ratio are fixed at 100 μl/h and 20, respectively. The PEO concentration is increased from 0 (i.e., water with $El = 0$) to 3000 ppm ($El = 138$) with eight other concentrations in between. Due to the increase of viscosity at higher PEO concentrations (see Table 1), *Re* decreases from 0.78 to 0.09 indicating a continuously weakened inertial lift force. As illustrated in Figure 8, the deflections of fluorescent spherical (white) and plain peanut (black) particles both appear to increase with the PEO concentration due to the dominant elastic lift force. However, since the trend differs between the two types of particles, the particle separation exhibits an interesting concentration-dependent pattern. Specifically, peanut particles (black) obtain a greater deflection than spherical particles (white) when the PEO concentration is below 300 ppm. Within this range, the center-to-center separation gap between the two particle streams first increases with the PEO concentration till 100 ppm and then decreases to zero at 300 ppm. In contrast, when the PEO concentration is over 300 ppm, spherical particles (white) experience a larger deflection than peanut particles (black). However, similar to the lower concentration range (i.e., < 300 ppm), the particle separation gap also undergoes a first-increase-then-decrease trend with the maximum taking place at around 1000 ppm. These interesting

phenomena are speculated to be a consequence of the complicated PEO concentration effects on the rotation of peanut particles, which requires further intensive studies.

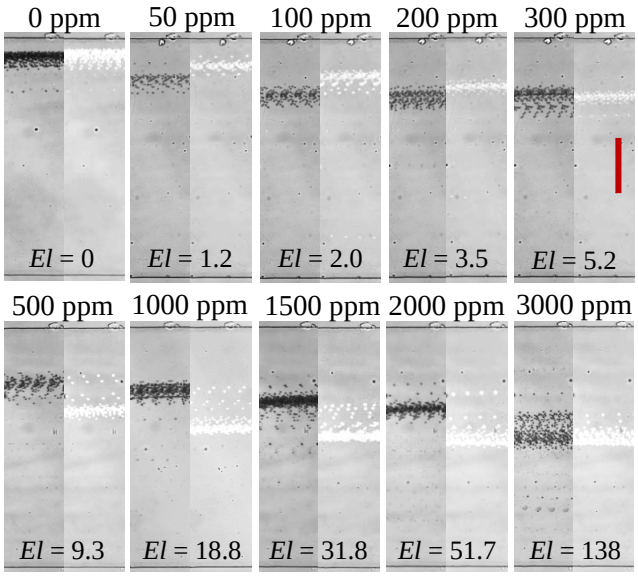

Figure 8 PEO concentration effect on the shape-based separation of fluorescent spherical (white) and plain peanut (black) particles via eiPFF in a 25 μm deep microchannel under a 100 μl/h sheath flow rate with a fixed flow rate ratio of 20. The scale bar on the right-most image of the top row represents 200 μm.

The effect of PEO concentration on particle deflection and separation in eiPFF can be viewed more clearly from the quantitative comparison of the exiting particle positions in Figure 9. The deflection of spherical particles quickly grows from 70 μm to 405 μm with the increase of PEO concentration until 1000 ppm, which then gradually levels off for concentrations over 1000 ppm with a seemingly equilibrium position near the channel centerline (i.e., particle stream position at 450 μm). In contrast, three regimes are observed for the deflection of peanut particles as the PEO concentration increases. From 0 ppm to 100 ppm (*El* = 2.0), the deflection rapidly increases from 80 μm to 220 μm, which is faster than that of spherical particles as viewed from the slopes of the two

curves in Figure 9. It then remains nearly constant at 225 μm (±5 μm) from 100 ppm to 500 ppm (*El* = 9.3), which is about half-way from the channel centerline. Beyond that, the deflection of peanut particles follows a nearly linear relationship for PEO concentration up to 3000 ppm (the highest under test). It may be safe to assume that the spherical and peanut particles will eventually both migrate along the channel centerline at even higher PEO concentrations. Under the experimental conditions, the largest separation gap between the two types of particles occurs in 1000 ppm PEO solution (*El* = 18.8).

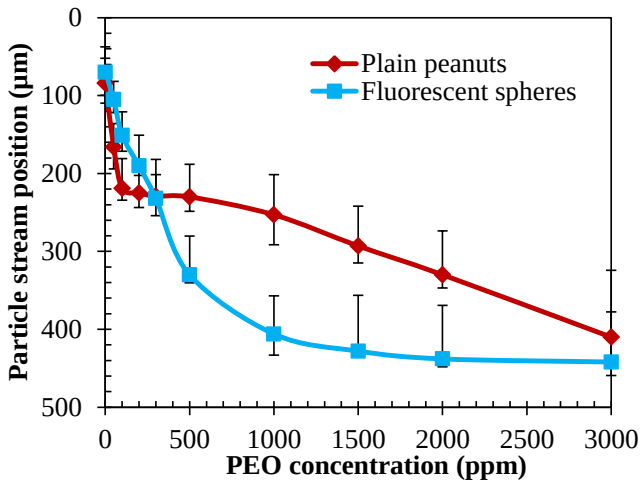

Figure 9 Comparison of the exiting positions of fluorescent spherical and plain peanut-shaped particles at the expansion of the main-branch for different PEO concentrations. All data points (symbols with error bars to encompass the span of each particle stream) were measured directly from the images in Figure 8.

7.3.5 Effects of channel aspect ratio, *AR*

Figure 10 shows the channel aspect ratio effect on the separation of spherical (white) and peanut (black) particles in 1000 ppm PEO solution through microchannels with depths of 100 μm (*AR* = 0.5), 40 μm (*AR* = 1.25), 25 μm (*AR* = 2.0) and 15 μm (*AR*

= 3.3) from left to right. Under the fixed sheath flow rate of 100 µl/h and flow rate ratio of 20, *Re* and *Wi* both increase with *AR* while the latter grows faster, yielding an increasing *El*. In the 100 µm- and 40 µm-deep channels, the equilibrium position of peanut particles (black) is farther away from the wall than that of spherical particles (white) as demonstrated in Figure 10(A). Moreover, part of the spherical particles choose to move near the corner in the 100 µm-deep channel, which is consistent with our recent observation in a similar microchannel.[26] The separation of the two types of particles is, however, weak in both of these low-*AR* channels due to the strong influence of particle dispersion. On the contrary, the deflection of spherical particles (white) surpasses that of peanut particles (black) in both the 25 µm and 15 µm deep channels. This is speculated to be due to the reduced rotational effects of the peanut particles, especially out-of-plane, in shallower microchannels, the consequence of which has been explained above (see Figure 4).

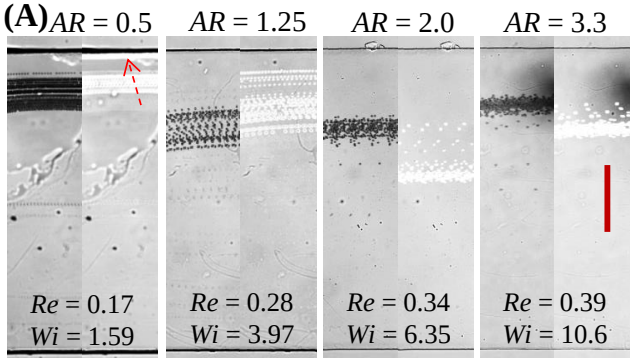

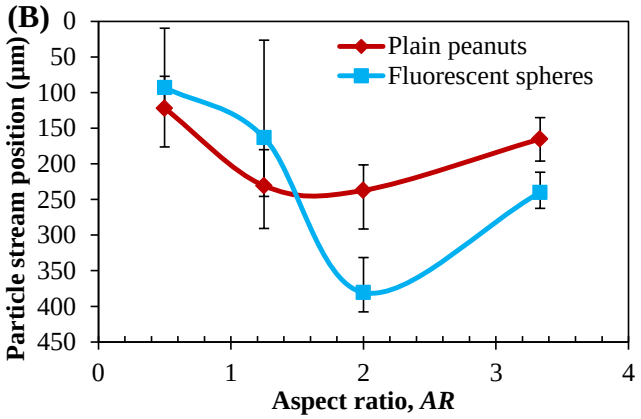

Figure 10 Channel aspect ratio effect on the shape-based separation of fluorescent spherical (white) and plain peanut (black) particles via eiPFF in 1000 ppm PEO solution under a 100 μl/h sheath flow rate with a fixed flow rate ratio of 20: (A) shows the cropped superimposed images at the channel expansion, where the dashed-dotted arrow highlights a secondary equilibrium position at the channel corner for spherical particles in a low-*AR* microchannel; (B) compares the exiting particle positions (symbols with error bars) at the expansion of the main-branch. The scale bar on the right-most image in (A) represents 200 μm.

A similar switch in the particle deflections due to the variation of channel depth has also been observed in our recent study of particle separation by size via eiPFF.[26] The particle separation gets apparently better than in the two deeper microchannels due partially to the significantly reduced particle dispersion. Figure 10(B) compares the exiting positions of the two types of particles at the expansion of microchannels with different *AR*. The two curves indicate that the deflections of spherical and peanut particles become equal in a microchannel with $AR \approx 1.5$ and the best separation is achieved at $AR = 2.0$. The non-monotonic dependence on *AR* for the elasto-inertial deflection of spherical particles is absent from our recently demonstrated inertia-enhanced pinched flow fractionation (iPFF) in water.[48] It seems, however, consistent with the inertially focused spherical particles in straight rectangular microchannels at very

high *Re*, where the equilibrium particle position can leave the channel center and shift towards the wall with the increase of *AR*.[47]

7.4 Conclusions

We have demonstrated a continuous separation of spherical and peanut particles of equal volume via a recently developed eiPFF technique.[26] This separation arises from the shape-dependent elasto-inertial lift-induced particle migration in viscoelastic fluids, which is speculated to correlate with the particle rotation effects. We have also performed a systematic experimental study of the parametric effects on such a label-free separation in terms of five dimensionless numbers, i.e., *Re*, *Wi*, *El*, α and *AR*. It has been found that the separation is significantly affected by the flow rate and works effectively at *Re* of order 1. The separation purity is high for both the peanut and spherical particles even at a relatively small flow rate ratio α. Moreover, the separation has been found to show a strong dependence on both the fluid elasticity, *El*, and the channel aspect ratio, *AR*. These phenomena happen because the two types of particles follow apparently different trends when the PEO concentration or the channel depth is varied. Interestingly, the elasto-inertial deflection of peanut particles can be equal to or greater/smaller than that of spherical particles, depending on the values of *El* and *AR*. A similar correlation with *AR* has also been recently reported by our group for size-based particle separation via eiPFF.[26] To further verify the hypothesis of shape-dependent elasto-inertial lift force, we are currently fabricating ellipsoidal particles of various aspect ratios using the protocol reported earlier[3,17] for additional test of shape-based particle separation via eiPFF.

Acknowledgements

This work was supported in part by NSF under grant CBET-1150670 and by Clemson University through an SGER (Small Grants for Exploratory Research) grant.

Supporting Information. Movies (at both the T-junction and outlet of the microchannel) for the shape-based particle separation in water and 1000 ppm PEO solution, respectively.

References

(1) Jadhao, V.; Thomas, C. K.; de la Cruza, M. O. *Porc. Natl. Acad. Sci. USA* **2014**, *111*, 12673-12678.

(2) Bauman, R. W. *Microbiology: With Diseases by Body System*. Chapters 4 and 11, Benjamin Cummings, 4 edition, **2014**.

(3) Champion, J. A.; Mitragotri, S. *Proc. Natl. Acad. Sci.* **2006**, *103*, 4930-4934.

(4) Martin, S. *Cell Cycle* **2009**, *8*, 3643-3647.

(5) Ebert, E. C.; Nagar, M.; Hagspiel, K. D. *Clinc. Gastroenterol. Hepatol.* **2010**, *8*, 483-489.

(6) Anstey, N. M.; Russell, B.; Yeo, T. W.; Price, R. N. *Trend. Parasitol.* **2009**, *25*, 220-227.

(7) Lenshof, A.; Laurell, T. *Chem. Soc. Rev.* **2010**, *39*, 1203-1217.

(8) Plouffe, B. D.; Murthy, S. K. *Anal. Chem.* **2014**, *86*, 11481-11488.

(9) Shields IV, C. W.; Reyes, C. D.; Lopez, G. P. *Lab Chip*, 2015, **15**, 1230-1249.

(10) Gossett, D. R.; Weaver, W. M.; Mach, A. J.; Hur, S. C.; Tse, H. T.; Lee, W.; Amini, H.; Di Carlo, D. *Anal. Bioanal. Chem.* **2010**, *397*, 3249-3267.

(11) Sugaya, S.; Yamada, M.; Seki, M. *Biomicrofluid.* **2011**, *5*, 24103.

(12) Yamada, M; Seki, M. *Anal. Chem.* **2006**, *78*, 1357-1362.

(13) Valero, A.; Braschler, T.; Rauch, A.; Demierre, N.; Barral, Y.; Renaud, P. *Lab Chip* **2011**, *11*, 1754-60.

(14) Beech, J. P.; Holm, S. H.; Adolfsson, K.; Tegenfeldt, J. O. *Lab Chip* **2012**, *12*, 1048-1051.

(15) Green, J. V.; Radisic, M.; Murthy, S. K. *Anal. Chem.* **2009**, *81*, 9178-9182.

(16) Zeming, K. K.; Ranjan, S.; Zhang, Y. *Nat. Communicat.* **2013**, *4*, article number 1625, doi:10.1038/ncomms2653.

(17) Masaeli, M.; Sollier, E.; Amini, H.; Mao, W.; Camacho, K.; Doshi, N.; Mitragotri, S.; Alexeev, A.; Di Carlo, D. *Phys. Rev. X* **2012**, *2*, 031017.

(18) Hur, S. C.; Choi, S. E.; Kwon, S.; Di Carlo, D. *Appl. Phys. Lett.* **2011**, *99*, 044101.

(19) Zhu, J.; Tzeng, T. J.; Xuan, X. *Electrophoresis* **2010**, *31*, 1382-1388.

(20) Zhu, J.; Xuan, X. *Biomicrofluid.* **2011**, *5*, 024111.

(21) DuBose, J.; Zhu, J.; Patel, S.; Lu, X.; Tupper, N.; Stonaker, J. M.; Xuan, X. *J. Micromech. Microeng.* **2014**, *24*, 115018.

(22) DuBose, J.; Lu, X.; Patel, S.; Qian, S.; Joo, S. W.; Xuan, X. *Biomicrofluid.* **2014**, *8*, 014101.

(23) Voldman, J. *Annu. Rev. Biomed. Eng.* **2006**, *8*, 425-454.

(24) Nam, J.; Lim, H.; Kim, D.; Jung, H.; Shin, S. *Lab Chip* **2012**, *12*, 1347-1354.

(25) Kang, K.; Lee, S. S.; Hyun, K.; Lee, S. J.; Kim, J. M. *Nat. Comm.* **2013**, *4*, Article number: 2567. doi:10.1038/ncomms3567.

(26) Lu, X.; Xuan, X. *Anal. Chem.* **2015**, *87*, 6389-6396.

(27) Yamada, M.; Nakashima, M.; Seki, M. *Anal. Chem.* **2004**, *76*, 5465-5471.

(28) Mortensen, N. A. *Anal. Chem.* **2007**, *79*, 9240-9241.

(29) Rodd, L. E.; Scott, T. P.; Boger, D. V.; Cooper-White, J. J.; McKinley, G. H. *J. Non-Newtonian Fluid Mech.* **2005**, *129*, 1-22.

(30) Maples, R. E. *Petroleum Refinery Process Economics*, **1993**, Pennwell, Publishing, Tulsa.

(31) Graessley, W. W. *Polymer* **1980**, *21*, 258–262.

(32) Tirtaatmadja, V.; Mckinley, G. H.; Cooper-White, J. J. *Phys. Fluid.* **2006**, *19*, 043101.

(33) Rubinstein, M.; Colby, R. H. *Polymer Physics* **2003**, Oxford University Press Inc.

(34) Rodd, L. E.; Cooper-White, J. J.; Boger, D. V.; McKinley, G. H. *J. Non-Newtonian Fluid Mech.* **2007**, *143*, 170-191.

(35) Rodd, L. E.; Lee, D.; Ahn, K. H.; Cooper-White, J. J. *J. Non-Newton. Fluid Mech.* **2010**, *165*, 1189-1203.

(36) Yang, S. Y.; Kim, J. Y.; Lee, S. J.; Lee, S. S.; Kim, J. M. *Lab Chip* **2011**, *11*, 266-273.

(37) Kim, J. Y.; Ahn, S. W.; Lee, S. S.; Kim, J. M. *Lab Chip* **2012**, *12*, 2807-2814.

(38) Lu, X.; Patel, S.; Zhang, M.; Joo, S.; Qian, S.; Ogale, A.; Xuan, X. *Biomicrofluid.* **2014**, 8, 021802.

(39) Liu, C.; Xue, C.; Chen, X.; Shan, L.; Tian, Y.; Hu, G. *Anal. Chem.* **2015**, *87*, 6041-6048.

(40) Jeffery, G. B. *Proc. R. Soc. A* **1922**, *102*, 161-179.

(41) Bartram, E.; Goldsmith, H. L.; Mason, S. G. *Rheol. Acta* **1975**, *14*, 776-782.

(42) Happel, J.; Brenner, H. *Low Reynolds Number Hydrodynamics*, Noordhoff International Publishing, Leyden, Netherlands, **1973**.

(43) Amini, H.; Lee, W.; Di Carlo, D. *Lab Chip* **2014**, *14*, 2739-2761.

(44) Martel, J. M.; Toner, M. *Annu. Rev. Biomed. Eng.* **2014**, *16*, 371-396.

(45) Giudice, F. D.; Romeo, G.; D'Avino, G.; Greco, F.; Netti, P. A.; Maffettone, P. L. *Lab Chip* **2013**, *13*, 4263-4271.

(46) Zhou, J.; Papautsky, I. *Lab Chip* **2013**, *13*, 1121-1132.

(47) Liu, C.; Hu, G.; Jiang, X.; Sun, J. *Lab Chip* **2015**, *15*, 1168-1177.

(48) Lu, X.; Xuan, X. *Anal. Chem.* **2015**, *87*, 4560-4565.

CHAPTER EIGHT

CONTINUOUS SHETH-FREE SEPARATION OF PARTICLES BY SHAPE IN VISCOELASTIC FLUIDS

Abstract

Shape is an important indicator of cell type, cycle and state etc., and can thus serve as a specific marker for label-free bioparticle separation. We demonstrate in this work a shape-based separation of equal-volumed spherical and peanut particles in viscoelastic fluids through straight rectangular microchannels. This continuous sheath-free separation arises from the shape-dependent equilibrium particle position(s) as a result of the flow-induced elasto-inertial lift and shear thinning effects. A continuous transition from single to dual and to triple equilibrium positions is observed for both types of particles with the increase of flow rate. However, the flow rate at which the transition takes place differs with the particle shape. This phenomenon occurs only in microchannels with a large aspect ratio (width/height) and has not been reported before. It is speculated to correlate with the dissimilar dependences of elastic and inertial lift forces on particle size and flow rate as well as the rotational effects of non-spherical particles.

8.1 Introduction

Shape is an important indicator of cell type,[1] cycle[2] and state[3] etc. It provides useful information in, for example, bioparticle identification,[4] cell synchronization[5] and

disease diagnostics[6] etc. Therefore, shape can be a specific marker for label-free bioparticle separation. It may also serve as a new intrinsic marker for fractionation of synthetic micro/nanoparticles with immense potential applications to both academics and industry. However, most of current microfluidic techniques have been developed to separate particles by size.[7-10] Only recently has shape-based particle separation been investigated in a few studies. It can be implemented through hydrodynamic filtration[11] in a complex network of microchannels[12] or through deterministic lateral displacement in high-resolution arrays of posts.[13,14] It has also been demonstrated by the use of dielectrophoresis that can be either electrode-[5] or insulator-based.[15,16] The throughput of this electrical method is, however, very low with the Reynolds number ($Re = \rho V D_h/\eta$ where ρ is the fluid density, V is the average fluid velocity, D_h is the hydraulic diameter, and η is the fluid viscosity) smaller than 0.1. In contrast, differential inertial focusing[17] can separate particles by shape at a high throughput where the Reynolds number must be over 10.[18]

Very recently our group has demonstrated a continuous separation of equal-volumed spherical and peanut-shaped particles[19] via a method we termed elasto-inertial pinched flow fractionation (eiPFF).[20] This method exploits the shape-dependent elasto-inertial lift force in viscoelastic fluids to increase the particle displacement for a high-purity separation at the Reynolds number of order 1. However, a sheath fluid is required to pre-focus the particle mixture which complicates the flow control and dilutes the separated particles. We demonstrate in this work that the flow-induced elasto-inertial lift[21] can direct particles towards shape-dependent equilibrium positions in straight

rectangular microchannels for a continuous sheath-free separation at the Reynolds number of order 1. Such a cross-stream particle migration in viscoelastic fluids[22-26] has been recently demonstrated to focus,[27-38] filtrate[39,40] and separate (by size[41-45] and deformability[46]) particles in microchannels.

8.2 Experiment

We used 4.18 μm-diameter spherical (green fluorescent, Bangs Laboratories, Inc.) and 3.5 μm-diameter/6 μm-length peanut-shaped (plain, Magsphere, Inc.) polystyrene particles to demonstrate the shape-based separation. The peanuts particles have a calculated total volume of 39.84 μm^3, which corresponds to an equivalent spherical diameter of 4.23 μm. The original aqueous suspensions of spherical (1% solid) and peanut-shaped (10% solid) particles were first mixed at a 10:1 ratio and then re-suspended in a polyethylene oxide (PEO) solution to a final concentration of 10^6 particles/mL. Three concentrations of PEO solutions, 500 ppm, 1000 ppm and 2000 ppm, were prepared by dissolving PEO powder (Sigma-Aldrich USA, molecular weight 2×10^6 Da) in water. The particle mixture was also re-suspended in water for a control experiment. A small amount of Tween 20 (0.5% v/v, Fisher Scientific) was added to each prepared particle suspension for the purpose of reducing particle aggregations and adhesions (to channel walls). The rheological properties of the PEO solutions are summarized in Table 1. The process for determining their relaxation times are provided in the Supplementary Information (Appendix C).[47]

Table 1. Rheological properties of the prepared PEO solutions.

Properties (at 20 °C)	PEO solution (c, ppm)		
	500	1000	2000
Zero-shear viscosity η (mPa·s)	1.8	2.3	4.1
Overlap concentration c^* (ppm)	858	858	858
Concentration ratio c/c^*	0.58	1.17	2.33
Zimm relaxation time, λ_{Zimm} (ms)	0.34	0.34	0.34
Effective relaxation time, λ_e (ms)	4.3	6.8	10.6

Four depths of 2 cm long and 50 μm wide straight rectangular microchannels are used in our experiments, which are 15, 25, 40 and 100 μm, respectively. They were fabricated with polydimethylsiloxane (PDMS) by the standard soft lithography method.[20,48] At the end of each channel, a 2 mm long and 900 μm wide expansion was designed to enhance the particle separation and facilitate the visualization. The particle suspension was driven through the microchannel by an infusion syringe pump (KDS-100, KD Scientific). Particle motion was recorded through an inverted microscope (Nikon Eclipse TE2000U, Nikon Instruments) with a CCD camera (Nikon DS-Qi1Mc) at a rate of 15 frames/s. Fluorescent and bright-field lights were used simultaneously to identify fluorescent spherical (appear bright) and plain peanut (appear dark) particles. Images were post-processed in Nikon Imaging Software (NIS-Elements AR 3.22). Superimposed images of fluorescent and plain particles were obtained by stacking a sequence of snapshot images (around 800) with the maximum and minimum intensity projections, respectively. The function of Particle Analysis in ImageJ software package (National Institute of Health) was used to measure the transverse particle positions at the channel outlet (i.e., the channel expansion), which were then used to calculate the probability distribution function (PDF) for each type of particles.

8.3 Results and discussion

Fig. 1 shows the shape-based separation of plain peanut and fluorescent spherical particles in 1000 ppm PEO solution through a 25 μm deep microchannel at a flow rate of 150 μL/h. The two types of particles are uniformly dispersed at the channel inlet in Fig. 1(a1) (Multimedia view), but split to dissimilar streams at the outlet in Fig. 1(a2) (Multimedia view). As viewed from the two superimposed images in Fig. 1(b1,b2), spherical particles are focused to a single band along the channel centerline while peanut particles migrate to two equilibrium positions that are each one quarter of the channel width away from the centerline. Such a continuous shape-based separation can be evaluated by the plot of particle PDF in Fig. 1(c), where over 1500 particles are counted for each type. The separation efficiency (defined as the particle percentage at a preferred outlet) is 95.2% and 95.1% for spherical and peanut particles inside and outside the region with an off-center distance of 130 μm in the expansion, respectively. The corresponding separation purity (defined as the ratio of the targeted to the total collected particles at an outlet) is also greater than 95% for each type of particles.

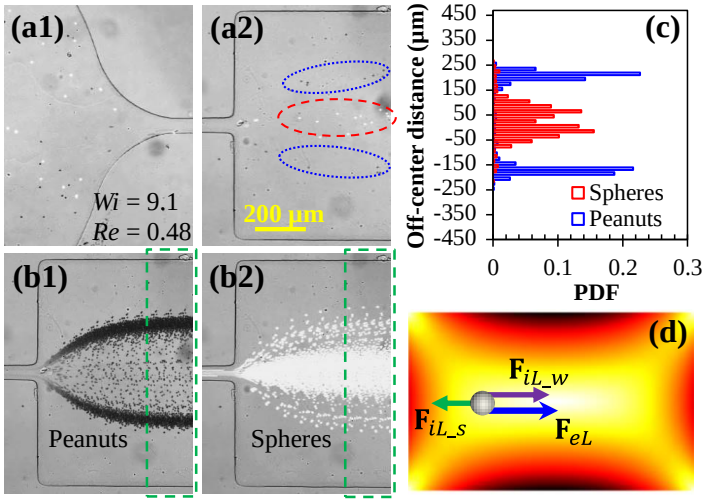

FIG. 1. Demonstration of shape-based separation of plain peanut (dark) and fluorescent spherical (bright) particles in 1000 ppm PEO solution through a 50 μm wide and 25 μm deep straight rectangular microchannel at a flow rate of 150 μL/h: (a1) and (a2) snapshot images at the channel inlet (Multimedia view) and outlet (Multimedia view), respectively, where the broken-line ellipses highlight the separated spherical and peanut particles; (b1) and (b2) superimposed images of peanut and spherical particles at the channel outlet, where the two dashed boxes highlight the regions to be used as cropped images in Figs. 2-4; (c) the plot of particle PDF at the channel outlet; (d) Force analysis of elastic lift, $\mathbf{F}_{eL}$, wall-induced inertial lift, $\mathbf{F}_{iL\_w}$, and shear gradient-induced inertial lift, $\mathbf{F}_{iL\_s}$, on a particle in a viscoelastic fluid flow through a rectangular microchannel, where the background color shows the contour of fluid shear rate (the darker the larger). The flow direction is from left to right in (a1,a2,b1,b2).

We have also done a control experiment of the same peanut and spherical particles in water under identical conditions (see Fig. S1 in the Supplementary Information[47]). Neither type of particles experiences a significant inertial focusing because of the small Reynolds number ($Re = 2\rho Q/\eta(w+h) = 1.11$ where Q is the flow rate, w and h are the channel width and height),[49-51] and hence no inertial separation is observed. The Reynolds number is even smaller in the PEO solution [$Re = 0.48$ as labeled in Fig. 1(a1)] due to the increased viscosity. Therefore, our recently demonstrated shape-dependence of the elastic lift,[19] $\mathbf{F}_{eL}$, is the primary reason for the observed particle separation in Fig. 1. As seen from the schematic in Fig. 1(d), $\mathbf{F}_{eL}$ directs particles towards the low-shear-rate regions, i.e., the centerline and four corners of a rectangular channel[21,29,52], and is characterized by the Weissenberg number ($Wi = \lambda_e\dot{\gamma} = 2\lambda_e Q/w^2 h = 9.1$ where λ_e is the effective relaxation time in Table 1 and $\dot{\gamma}$ is the fluid shear rate). This force competes with the shear gradient-induced inertial lift, $\mathbf{F}_{iL\_s}$, and the wall-induced inertial lift, $\mathbf{F}_{iL\_w}$, which direct a particle to the chanter wall and center, respectively, as illustrated in Fig. 1(d). The elastic and inertial lift forces are each a

positive function of flow rate[21,27,42,53,54] and expressed as follows for particles of (equivalent) spherical diameter *a* (see the Supplementary Information[47] for derivations)

$$\mathbf{F}_{eL} \sim \lambda_e (a/w)^3 Q^3 \quad (1)$$

$$\mathbf{F}_{iL} = \mathbf{F}_{iL\_s} + \mathbf{F}_{iL\_w} \sim \rho (a/w)^4 Q^2 \quad (2)$$

Fig. 2 shows the flow rate effect on the shape-based particle separation in 1000 ppm PEO solution through a 25 μm deep microchannel. As the flow rate increases, *Re* and *Wi* both increase (see the labeled values on the images) while their ratio, i.e., the elasticity number ($El = Wi/Re = \lambda_e \eta (w+h)/\rho w^2 h$), is independent of flow kinematics and remains at 18.8. At 20 μL/h, peanut and spherical particles are both focused to a stream near the channel centerline except that a small percentage of spherical particles travel near the corner (highlighted by the dashed-line arrows in Fig. 2). Consistent with our earlier studies,[19,20] this secondary equilibrium position disappears at higher flow rates and occurs due to the corner-directed elastic lift[21,29,52] under a negligible influence of inertial lift. As the flow rate is increased to 100 μL/h, spherical particles get better focused towards the channel center while peanut particles instead migrate towards the walls and become split into two streams. This differential elasto-inertial focusing yields the shape-based particle separation, which still holds effective at 150 and 200 μL/h. However, two peaks start occurring for spherical particles in the PDF plot. They grow and move away from the channel center when the flow rate is further increased to 300 μL/h. Meanwhile, however, the two streams of peanut particles shift back towards the channel center, leading to a reduced particle separation. Interestingly, at the flow rate

of 300 µL/h (and higher) where *Re* is about 1, an additional equilibrium position appears for each type of particles which eventually breaks down this shape-based separation..

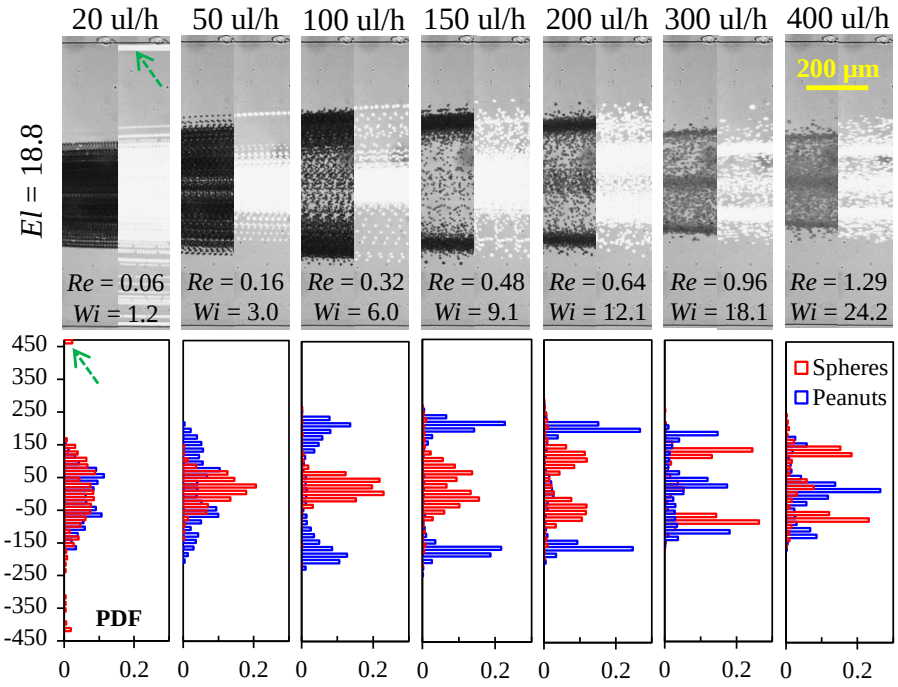

FIG. 2. Flow rate effect (in terms of the Reynolds number, *Re*, and Weissenberg number, *Wi*) on shape-based separation of plain peanut (dark) and fluorescent spherical (bright) particles in 1000 ppm PEO solution through a 50 µm wide and 25 µm deep straight rectangular microchannel: (top row) cropped superimposed particle images at the channel outlet [highlighted by the dashed-line boxes in Fig. 1(b1,b2)]); (bottom row) plots of particle PDF at the channel outlet. The dashed-line arrows highlight a secondary equilibrium position for spherical particles near the channel corner at a flow rate of 20 µL/h.

A similar trend can be identified from Fig. 2 for the elasto-inertial focusing between peanut and spherical particles. With the increase of flow rate (or *Re*), each type of particles experiences first a transition from single equilibrium position at the channel centerline to dual equilibrium positions on the two sides of the centerline, and then to triple equilibrium positions at both the centerline and its two sides. However, the two

transitions for peanut particles both take place at smaller flow rates than for spherical particles, which yields the shape-based separation demonstrated in Fig. 1 and Fig. 2. The exact mechanism behind this phenomenon is currently unclear, which is speculated to correlate with the rotational effects of peanut particles. As demonstrated in our earlier study,[19] the preferentially parallel orientation of peanut particles to the flow direction renders the elastic and inertial lift forces more dependent on their shorter dimension (i.e., 3.5 μm), smaller than the diameter of spherical particles (i.e., 4.18 μm). Hence, the dissimilar dependences of $\mathbf{F}_{eL}$ in Eq. (1) and $\mathbf{F}_{iL}$ in Eq. (2) on particle size and flow rate may lead to the observed phenomenon in Fig. 2.

Fig. 3 shows the PEO concentration effect (in terms of the elasticity number, *El*) on the shape-based particle separation in a 25 μm deep microchannel under a fixed flow rate of 150 μL/h. Due to the increased viscosity, *Re* decreases (from 0.62 to 0.48 and 0.27 for 500, 1000 and 2000 ppm) at higher PEO concentrations indicating a weakened inertial lift. In contrast, *Wi* increases due to the extended relaxation time at higher PEO concentrations. The separation is barely visible in 500 ppm PEO because both peanut and spherical particles are still at the state of single equilibrium position along the channel centerline. It is significantly improved in 1000 ppm PEO due to the enhanced elasto-inertial particle focusing, a consequence of the increased elastic lift and the decreased inertial lift. In 2000 ppm PEO, spherical particles experience an improved focusing towards the single equilibrium position along the channel centerline. However, since the two equilibrium positions of peanut particles both shift towards the centerline, the separation gets diminished in 2000 ppm PEO.

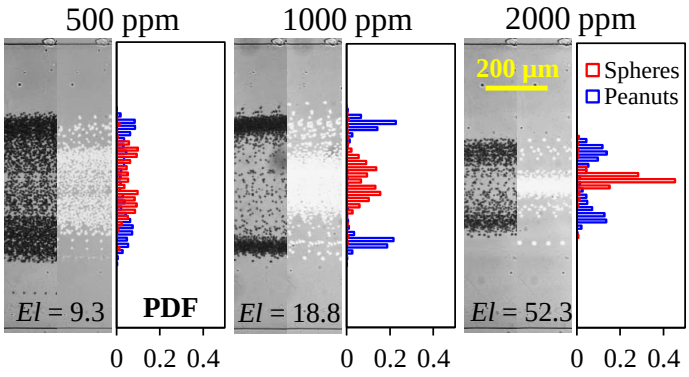

FIG. 3. PEO concentration effect (in terms of the elasticity number, *El*) on shape-based separation of plain peanut (dark) and fluorescent spherical (bright) particles in a 50 μm wide and 25 μm deep straight rectangular microchannel under a flow rate of 150 μL/h: the left and right halves of each panel show the cropped superimposed particle images and the corresponding PDF plots at the channel outlet, respectively.

We have also studied the flow rate effect on the shape-based particle separation in 500 ppm and 2000 ppm PEO solutions (see Fig. S2 in the Supplementary Information[47]). Similar to that in Fig. 2, a continuous transition from single to dual and to triple equilibrium positions is found in both PEO concentrations for peanut and spherical particles. Moreover, the two transitions for peanut particles still happen ahead of spherical ones with the increase of low rate. However, the flow rates at which the transitions take place depend on the PEO concentration due to its effect on $\mathbf{F}_{eL}$ in Eq. (1) via the relaxation time, λ_e. This phenomenon is also believed to be related to the enhanced shear thinning effects at higher PEO concentrations, which has been demonstrated in earlier works[25,26,33,44] to direct particles away from the channel centerline. The best separation in 500 ppm and 2000 ppm PEO (see Fig. S2 in the Supplementary Information[47]) takes place at 200-300 μL/h and 100-150 μL/h, respectively, which seem consistent with the flow rate of 150-200 μL/h in 1000 ppm PEO

(see Fig. 2). Among these three PEO concentrations, 1000 ppm is found to offer the best separation performance in terms of particle PDF.

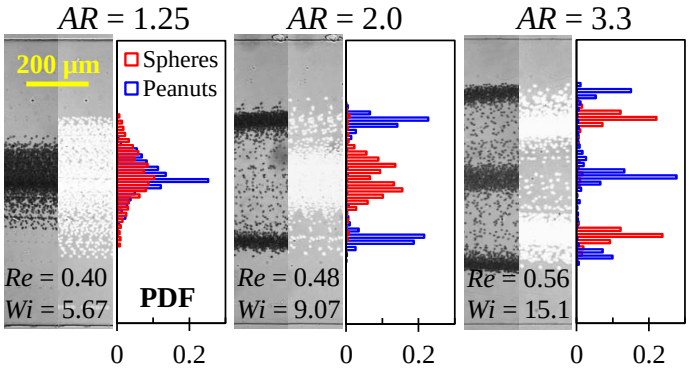

FIG. 4. Channel aspect ratio (*AR*) effect on shape-based separation of plain peanut (dark) and fluorescent spherical (bright) particles in 50 µm wide straight rectangular microchannels under a flow rate of 150 µL/h. The left and right halves of each panel show the cropped superimposed particle images and the corresponding PDF plots at the channel outlet.

Fig. 4 shows the effect of channel aspect ratio, $AR = w/h$, on the shape-based particle separation in 1000 ppm PEO solution through microchannels of 40 µm (*AR* = 1.25), 25 µm (*AR* = 2.0) and 15 µm (*AR* = 3.3) deep, respectively. Under a constant flow rate of 150 µL/h, a larger *AR* corresponds to an increased *Re* and *Wi*. In the nearly square microchannel with *AR* = 1.25 (left panel in Fig. 4), peanut and spherical particles are each focused towards the channel centerline. This single equilibrium particle position remains unvaried with the increase of flow rate (up to 1 mL/h), which seems to be consistent with previous studies in square microchannels (*AR* = 1.0).[34,39,42,44] Since no transition to dual equilibrium positions is observed (see Fig. S3 in the Supplementary Information[47]), shape-based particle separation is unavailable in a nearly square microchannel. This is also true in a 100 µm deep channel with a low *AR* (= 0.5, data not shown). In the 15 µm

deep microchannel with a high *AR* (= 3.3, see the right panel in Fig. 4), peanut particles are focused to three equilibrium positions under a flow rate of 150 μL/h while spherical particles have only two equilibrium positions. In this high *AR* microchannel, a transition from single to dual and to triple equilibrium positions still exists for both types of particles (see Fig. S4 in the Supplementary Information[47]). Moreover, as the transition for peanut particles also happens at a smaller flow rate than for spherical particles, the best separation happens at a flow rate of 50-100 μL/h, which is only one half of that in the 25 μm deep microchannel with *AR* = 2.0.

8.4 Conclusions

In summary, we have demonstrated a continuous sheath-free separation of spherical and peanut-shaped rigid particles of equal volume via the elasto-inertial focusing effect in straight rectangular microchannels. This separation exploits the gap between the flow rates at which the two types of particles switch from single to dual equilibrium positions, respectively. It can only take place in large aspect-ratio microchannels, which is $AR \geq 2$ in our tests, because both types of particles migrate towards the single equilibrium position at the centerline of microchannels with an intermediate or low *AR*. The separation is also found to be strongly dependent on PEO concentration because of its influence on the elastic (via the fluid relaxation time) and inertial (via the fluid viscosity) lifts as well as the shear thinning effects. If necessary, the PEO polymer can be removed by rinsing the separated particle suspension with water or other buffer solutions via centrifugation. Future work will be on the theoretical

understanding and numerical prediction of shape-based particle separation in viscoelastic fluids. Moreover, the effects of other experimental parameters such as channel length and polymer type [e.g., polyvinylpyrrolidone (PVP)[39,46] and polyacrylamide (PAA)[27,43]] will be investigated. In addition, we are developing an apparatus to fabricate spheroidal particles of various aspect ratios using the protocol reported earlier[18] for further tests of shape-based particle separation in viscoelastic fluids.

This work was partially supported by NSF under grant CBET-1150670.

References

[1] S. Mitragotri, and J. Lahann, Nature Mater. **8**, 15 (2009).

[2] S. Martin, Cell Cycle **8**, 3463-3647 (2009).

[3] E. C. Ebert, M. Nagar, and K. D. Hagspiel, Clin. Gastroenterol. Hepatol. **8**, 483-489 (2010).

[4] J. Janca, V. Halabalova, and J. Rzicka, J. Chromatograph. A **1217**, 8062-8071 (2010).

[5] A. Valero, T. Braschler, A. Rauch, N. Demierre, Y. Barral, and P. Renaud, Lab Chip **11**, 1754-60 (2011).

[6] N. M. Anstey, B. Russell, T. W. Yeo, and R. N. Price, Trend. Parasitol. **25**, 220-227 (2009).

[7] A. Karimi, S. Yazai, and A.M. Ardekani, Biomicrofluid. **7**, 021501 (2013).

[8] P. Sajeesh, and A. K. Sen, Microfluid. Nanofluid. **17**, 1-52 (2014).

[9] Z. T. Yu, K. M. Yong, J. Fu, Small **10**, 1687-1703 (2014).

[10] C. W. Shields IV, C. D. Reyes, and G. P. Lopez, Lab Chip **15**, 1230-1249 (2015).

[11] Yamada, M; Seki, M. Anal. Chem. **78**, 1357-1362 (2006).

[12] S. Sugaya, M. Yamada, and M. Seki, Biomicrofluid. **5**, 24103 (2011).

[13] J. P. Beech, S. H. Holm, K. Adolfsson, and J. O. Tegenfeldt, Lab Chip **12**, 1048-1051 (2012).

[14] K. K. Zeming, S. Ranjan, and Y. Zhang, Nat. Communicat. **4**, article number 1625, doi:10.1038/ncomms2653 (2013).

[15] Y. Song, J. Yang, X. Shi, H. Jiang, Y. Wu, R. Peng, Q. Wang, N. Gong, X. Pan, Y. Sun, and d. Li, Sci. China, **55**, 524-530 (2012).

[16] J. DuBose, X. Lu, X., S. Patel, S. Qian, S. W. Joo, and X. Xuan, Biomicrofluid. **8**, 014101 (2014).

[17] S. C. Hur, S. E. Choi, S. Kwon, and D. Di Carlo, Appl. Phys. Lett. **99**, 044101 (2011).

[18] M. Masaeli, E. Sollier, H. Amini, W. Mao, K. Camacho, N. Doshi, S. Mitragotri, A. Alexeev, and D. Di Carlo, Phys. Rev. X **2**, 031017 (2012).

[19] X. Lu, and X. Xuan, Anal. Chem. **87**, 11523–11530 (2015).

[20] X. Lu, and X. Xuan, X. Anal. Chem. **87**, 6389-6396 (2015).

[21] G. D'Avino, and P. L. Maffettone, J. Non-Newton. Fluid Mech. **215**, 80-104 (2015).

[22] A. Karnis, H. L. Goldsmith, and S. G. Mason, S. G., Nature **200**, 159-160 (1963).

[23] B. P. Ho, and L. G. Leal, J. Fluid Mech. **76**, 783-799 (1976).

[24] G. Leal, J. Non-Newton. Fluid Mech. **5**, 33-78 (1979).

[25] P. Y. Huang, J. Feng, H. H. Hu, and D. D. Joseph, J. Fluid Mech. **343**, 73-94 (1997).

[26] P. Y. Huang, and D. D. Joseph, J. Non-Newtonian Fluid Mech. **90**, 159-185 (2000).

[27] A. M. Leshansky, A. Bransky, N. Korin, and U. Dinnar, Phys. Rev. Lett. **98**, 234501 (2007).

[28] G. D'Avino, G. Romeo, M. Villone, F. Greco, F., P. A. Netti, and P. L. Maffettone, Lab Chip **12**, 1638-1645 (2012).

[29] J. Y. Kim, S. W. Ahn, S. S. Lee, and J. M. Kim, Lab Chip **12**, 2807-2814 (2012).

[30] S. Cha, T. Shin, S. S. Lee, W. Shim, G. Lee, S. J. Lee, Y. Kim, and J. M. Kim, Anal. Chem. **84**, 10471-10477 (2012).

[31] D. L. Lee, H. Brenner, J. R. Youn, and Y. S. Song, Sci. Rep. **3**, article number 3258 (2013).

[32] F. D. Giudice, G. Romeo, G. D'Avino, F. Greco, P. A. Netti, and P. L. Maffettone, Lab Chip **13**, 4263-4271 (2013).

[33] K. W. Seo, H. J. Byeon, H. K. Huh, and S. J. Lee, RSC Adv. **4**, 3512-3520 (2014).

[34] E. J. Lim, T. Ober, J. F. Edd, S. P. Desai, D. Neal, K. W. Bong, P. S. Doyle, G. H. McKinley, and M. Toner, Nat. Comm. **5**, Article number: 4120 (2014).

[35] S. Cha, K., Kang, J. B. You, S. G. Im, Y. Kim, and J. M. Kim, Rehol. Acta **53**, 927-933 (2014).

[36] K. W. Seo, Y. R. Ha, and S. J. Lee, Appl. Phys. Lett. **104**, 213702 (2014).

[37] F. D. Giudice, G. D'Avino, F. Greco, P. A. Netti, and P. L. Maffettone, Microfluid. Nanofluid. **19**, 95-104 (2015).

[38] D. Yuan, J. Zhang, S. Yan, C. Pan, G. Alici, N. T. Nguyen, and W. H. Li, Biomicrofluid. **9**, 044108 (2015).

[39] S. Y. Yang, J. Y. Kim, S. J. Lee, S. S. Lee, and J. M. Kim, Lab Chip **11**, 266-273 (2011).

[40] S. W. Ahn, S. S. Lee, S. J. Lee, and J. M. Kim, Chem. Eng. Sci. **126**, 237-243 (2015).

[41] J. Nam, H. Lim, D. Kim, H. Jung, and S. Shin, Lab Chip **12**, 1347-1354 (2012).

[42] K. Kang, S. S. Lee, K. Hyun, S. J. Lee, and J. M. Kim, Nat. Comm. **4**, Article number: 2567 (2013).

[43] H. Lim, J. Nam, and S. Shin, Microfluid. Nanofluid. **17**, 683-692 (2014).

[44] C. Liu, C. Xue, X. Chen, L. Shan, Y. Tian, and G. Hu, Anal. Chem. **87**, 6041–6048 (2015).

[45] J. Nam, B. Namgung, C. T. Lim, J. Bae, H. L. Leo, K. S. Cho, and S. Kim, J. Chromatography A **1406**, 244-250 (2015).

[46] S. Yang, S. S. Lee, S. W. Ahn, K. Kang, W. Shim, G. Lee, K. Hyune, and J. M. Kim, Soft Matt. **8**, 5011-5019 (2012).

[47] See supplementary material at [URL will be inserted by AIP] for the determination of PEO solution properties, control experiment of shape-based particle separation in water, derivation of Eqs. (1) and (2), and flow rate effects on shape-based particle separation in different PEO solutions through microchannels of different aspect ratios.

[48] X. Lu, S. Patel, M. Zhang, S. Joo, S. Qian, A. Ogale, and X. Xuan, Biomicrofluid. **8**, 021802 (2014).

[49] H. Amini, W. Lee, and D. Di Carlo, Lab Chip **14**, 2739-2761 (2014).

[50] J. M. Martel, and M. Toner, M., Annu. Rev. Biomed. Eng. **16**, 371-396 (2014).

[51] J. Zhang, S. Yan, D. Yuan, G. Alici, N. T. Nguyen, M. E. Warkiani, and W. Li, Lab Chip, in press. DOI: 10.1039/C5LC01159K (2015).

[52] K. W. Seo, Y. J. Kang, and S. J. Lee, Phys. Fluid. **26**, 063301 (2014).

[53] E. S. Asmolov, J. Fluid Mech. **381**, 63-87 (1999).

[54] D. Di Carlo, J. F. Edd, K. J. Humphry, H. A. Stone, and M. Toner, Phys. Rev. Lett. **102**, 094503 (2009).

CHAPTER NINE

CONCLUSIONS AND FUTURE WORK

9.1 Conclusions

This dissertation has extensively investigated the particle motions in non-Newtonian fluids in both electric field- and pressure-driven flows through microchannels. The first part focuses on the electrokinetic transport phenomena in viscoelastic fluids though a constricted microchannel. An oscillatory particle motion has been observed in the first experimental investigation of particle electrophoresis, for particles moving in the same direction of fluid electroosmosis. Then the electrokinetic particle focusing in viscoelastic fluids has been studied under the same experimental condition but with particles moving against fluid electroosmosis. Particles are found to have an opposite focusing trend to that in the Newtonian fluid with respect to electric field. The flow visualization study of electrokinetic flow in a viscoelastic fluid has shown that the small particle trajectories, which represent the electroosmotic flow streamlines, are significantly different from those in the Newtonian fluid at the upstream of the microchannel constriction. These phenomena are speculated to be a consequence of the fluid viscoelasticity effects. The second part of this dissertation concentrates on the particle transport in pressure driven flows through straight rectangular microchannels. Both size- and shape-based separations have been demonstrated by both eiPFF and sheath-free techniques in non-Newtonian fluids. These separations are found to be significantly dependent on the dimensionless numbers, i.e., *Re, Wi, El* and *AR*. Moreover, we have systematically studied the elasto-inertial particle focusing in straight rectangular

microchannels. The detailed conclusion and major contribution of each chapter in this dissertation are listed as follows.

1. In chapter 2, an oscillatory particle motion has been observed in the experimental investigation of particle electrophoresis in viscoelastic PEO solutions through a microchannel constriction. In distinct contrast with that in a Newtonian fluid, an oscillatory particle motion is observed in the constriction region. Such a stream-wise particle oscillation continues and remains inside the constriction until a sufficient number of particles are attached to form a chain for them to escape. This oscillatory motion is affected by the electric field magnitude, particle size and PEO concentration. We speculate that the particle oscillation arises from the competition of the viscoelastic force induced in the constriction and the electrokinetic force.
2. In chapter 3, the effects of particle charge on the electrokinetic motion of particles in viscoelastic fluids have been studied under the same experimental conditions as in chapter 2. While particles moving along with the fluid exhibit the bouncing phenomenon, particles that move against the fluid get focused when passing the microchannel constriction. However, this electrokinetic focusing is found to decrease with the increase of the applied DC electric field, which is different from the focusing trend in Newtonian fluids. In addition, particle aggregations are formed inside the constriction at high electric fields. They can then either move forward and exit the constriction in an explosive manner or roll back to the constriction entrance for further accumulations. These observed phenomena are

speculated to be a consequence of the fluid viscoelastic effects. We conclude that the constriction-induced DEP is not a good option for electrokinetic focusing of particles suspended in non-Newtonian fluids.

3. In chapter 4, we have conducted the flow visualization study of electrokinetic flow in viscoelastic fluids as inspired by the electrokinetic particle motions. The particle trajectories which represent the flow streamlines are found to be deflected and asymmetric near the constriction entrance at the upstream in the viscoelastic fluid. The perturbation of particle trajectories grows with the electric field, and extends towards upstream at high electric fields. The numerical result of Oldroyd-B model obtains a smaller flow rate than that of the Newtonian one.
4. In chapter 5, a systematic experimental study has been conducted for continuous particle separation in PEO solutions via eiPFF. It is found that eiPFF offers a much higher particle throughput and a much better separation resolution than the traditional PFF. Two new phenomena have been observed: one is that the particle focusing and separation via eiPFF do not increase monotonically with *El*; and the other is that the channel aspect ratio strongly affects the particle separation. We have also found that the elasto-inertial deflection of small particles can be even greater than that of large ones in a high-*AR* channel when *Re* is less than 1.
5. In chapter 6, we have comprehensively studied the elasto-inertial particle focusing through straight rectangular microchannels in terms of various parameters. Multiple equilibrium particle positions are observed, which are affected by the particle size, flow rate, channel aspect ratio and polymer solution type. In addition,

an interesting trend has been found that the particle size (blockage ratio) plays a less important role on the equilibrium position with the increasing channel aspect ratio. A size-based particle separation has also been achieved without a sheath flow focusing. Further experiments in PAA solutions of varied glycerol concentrations in a near-slit channel have demonstrated that the shear-thinning effect inhibits the elastic lift and deflects particles away from the center. The 2D numerical studies of the particle motion via Oldroyd-B and Giesekus models are qualitatively consistent with our experimental observations of the viscoelastic and shear thinning effects on the elasto-inertial particle focusing.

6. In chapter 7, we have achieved a continuous separation of spherical and peanut-shaped rigid particles of equal volume as inspired by the size-based separation via the eiPFF technique. This separation arises from the shape-dependent elasto-inertial lift induced particle migration in viscoelastic fluids, which is speculated to correlate with the particle rotation effects. It is found that the separation is strongly affected by the flow rate, fluid elasticity, and channel aspect ratio. Interestingly, the elasto-inertial deflection of the peanut particles can be either greater or smaller than that of equally-volumed spherical particles.
7. In chapter 8, we have demonstrated a continuous sheath-free shape-based separation via the elasto-inertial focusing effect in straight rectangular microchannels. This separation can only take place in large aspect-ratio microchannels, which is $AR \geq 2$ in our tests, because both types of particles migrate towards the single equilibrium position at the centerline of microchannels

with an intermediate or low *AR*. The separation is also strongly dependent on PEO concentration because of its influence on the elastic and inertial lift forces.

9.2 Future work

In the first part, the electrokinetic transport phenomena have been studied in viscoelastic fluids though a constricted microchannel. In future work we will continue the parametric study to find out how other critical factors, such as channel aspect ratio and constriction ratio, affect the flow and particle transport. These will help us getting closer to the mechanisms of the phenomena. Intensive future studies of numerical simulation are required to verify and predict the experimental observations. In the second part, the elasto-inertial particle focusing and separation have been studied in non-Newtonian fluids. The future work can be extended to submicron particle manipulation. Meanwhile, a 3D numerical model will be implemented to study the elasto-inertial lift and particle equilibrium position. In addition, to further verify the hypothesis of shape-dependent elasto-inertial lift force, we will work with ellipsoidal particles of various aspect ratios. The numerical prediction of the shape-based particle separation in viscoelastic fluids will also be carried out. Moreover, we will extend the experimental and numerical studies to biological particles in body fluids.

APPENDICES

Appendix A

SUPPORTING INFORMATION FOR CONTINUOUS MICROFLUIDIC PARTICLE SEPARATION VIA ELASTO-INERTIAL PINCHED FLOW FRACTIONATION (eiPFF)

Determination of the fluid properties in Table 1 in the main text

The zero-shear viscosity, η_0, of the glycerol/water-based PEO solutions was calculated using the viscosity blending equation[1] via the reported viscosity values of aqueous PEO[2] and glycerol[3] solutions. The obtained values appear to be consistent with the experimental data reported by Yang et al.,[4] Nam et al.[5] and Rodd et al.[6,7] The overlap concentration, c^*, for PEO solutions was calculated from the expression of Graessley,[8] $c^* = 0.77/[\eta]$ ppm where $[\eta] = 0.072M_w^{0.65} = 897$ ml/g is the intrinsic viscosity given by the Mark-Houwink relation.[2] We noticed that adding glycerol into the aqueous PEO solution had been found by Rodd et al.[6] to decrease the intrinsic viscosity and hence increase the overlap concentration. This effect was, however, estimated to be less than 10% for the solvent we used. Therefore, the prepared non-Newtonian fluids are in the dilute (500 ppm PEO/glycerol solution) or semi-dilute (all others) regime. They all exhibit a mild shear-thinning effect as reported in earlier studies.[4-7] The effective relaxation time of the prepared PEO solutions was estimated from the following empirical formula,[9]

$$\lambda_e = 18\lambda_{Zimm}(c/c^*)^{0.65} \quad (1)$$

where λ_{Zimm} is the relaxation time predicted according to Zimm theory,[10]

$$\lambda_{Zimm} = F\frac{[\eta]M_w\eta_s}{N_A k_B T} \quad (2)$$

In the above $F = 0.463$ is the pre-factor estimated from the Remann Zeta function using a solvent quality exponent 0.55,[2] η_s = 1.8 mPa·s is the solvent (i.e., 21 wt.% glycerol/water) viscosity,[3] N_A is the Avogadro's constant, k_B is the Boltzmann's constant, and T is the absolute temperature.

Clarification of eq 6 in the main text

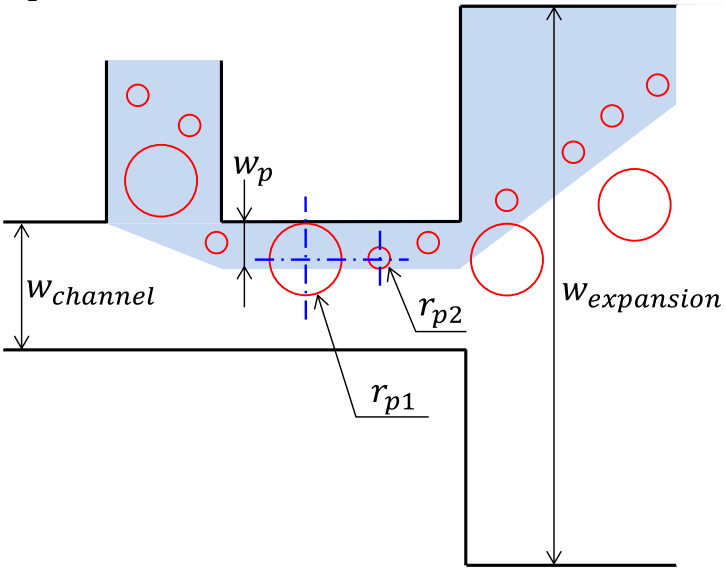

Figure S1. Schematic explanation on how eq 6 in the main text is obtained. The symbols w_p, $w_{channel}$ and $w_{expansion}$ represent the widths of the sheath-fluid focused particle solution, the main-branch, and the channel expansion, respectively. The symbols r_{p1} and r_{p2} are the radii of the two types of particles to be separated via PFF.

The particle separation in traditional PFF arises from the dissimilar center positions for particles of different sizes in a laminar flow.[11] As seen from Figure S1, when the larger particles of radius r_{p1} are aligned by the sheath fluid, their center is r_{p1} away from the sidewall. Since the center of the smaller particles with radius r_{p2} can at most overlap with that of the larger ones for separation via PFF, as indicated by the dashed-dotted line in

Figure S1, the width of the particle solution in the main-branch (highlighted by the background color) should be no more than $r_{p1} + r_{p2}$. This latter value is exactly the $w_{p,max}$ in eq 6 in the main text.

References

(1) R.E. Maples, *Petroleum Refinery Process Economics*, 1993, Pennwell, Publishing, Tulsa.

(2) L. E. Rodd, T. P. Scott, D. V. Boger, J. J. Cooper-White and G. H. McKinley, *J. Non-Newtonian Fluid Mech.*, 2005, **129**, 1-22.

(3) N. S. Cheng, *Indust. Eng. Chem. Res.*, 2008, **47**, 3285-3288.

(4) S. Y. Yang, J. Y. Kim, S. J. Lee, S. S. Lee and J. M. Kim, *Lab Chip*, 2011, **11**, 266-273.

(5) J. Nam, H. Lim, D. Kim, H. Jung and S. Shin, *Lab Chip*, 2012, **12**, 1347-1354.

(6) L. E. Rodd, J. J. Cooper-White, D. V. Boger and G. H. McKinley, *J. Non-Newtonian Fluid Mech.*, 2007, **143**, 170-191.

(7) L. E. Rodd, D. Lee, K. H. Ahn, and J. J. Cooper-White, *J. Non-Newton. Fluid Mech.*, 2010, **165**, 1189-1203.

(8) W. W. Graessley, *Polymer*, 1980, **21**, 258–262.

(9) V. Tirtaatmadja, G. H. Mckinley and J. J. Cooper-White, *Phys. Fluid.*, 2006, **19**, 043101.

(10) M. Rubinstein and R. H. Colby, *Polymer Physics*, 2003, Oxford University Press Inc.

(11) M. Yamada, M. Nakashima and M. Seki, *Anal. Chem.*, 2004, **76**, 5465-5471.

Appendix B

SUPPLEMENTARY MATERIAL FOR PARTICLE FOCUSING IN VISCOELASTIC FLUIDS THROUGH RECTANGULAR STRAIGHT MICROCHANNELS

Rheology of PEO solution

Zimm relaxation times were calculated from Zimm theory (Rubinstein and Colby 2003)

$$\lambda_{Zimm} = F\frac{[\eta]M_w\eta_s}{N_A k_B T} = 0.34ms$$

where $F = \sum_{i=1}^{\infty} i^{-3\nu} = 0.463$ was estimated from Remann Zeta function using a solvent quality exponent, ν = 0.55 (Rodd et al. 2005); the solvent viscosity $\eta_s = 1$ mPa·s; N_A is the Avogadro's constant; k_B is the Boltzmann's constant; the absolute temperature T = 293.15 K. The effective relaxation times of PEO solutions were estimated according to (Tirtaatmadja et al. 2006)

$$\lambda_e = 18\lambda_{Zimm}\left(\frac{c}{c^*}\right)^{0.65} = 6.8ms$$

where the overlap concentration c^* was calculated from (Graessley1980), $c^* = 0.77/[\eta]$ = 858 ppm. The intrinsic viscosity, $[\eta] = 0.072M_w^{0.65}$ = 897 ml/g, was given by the Mark-Houwink relation (Rodd et al. 2005). The dilute PEO solution exhibits non- or a mild shear-thinning effect as reported in earlier work (Cox and Brenner 1968; Rodd et al. 2005; Rodd et al. 2007).

Results of *AR* effect

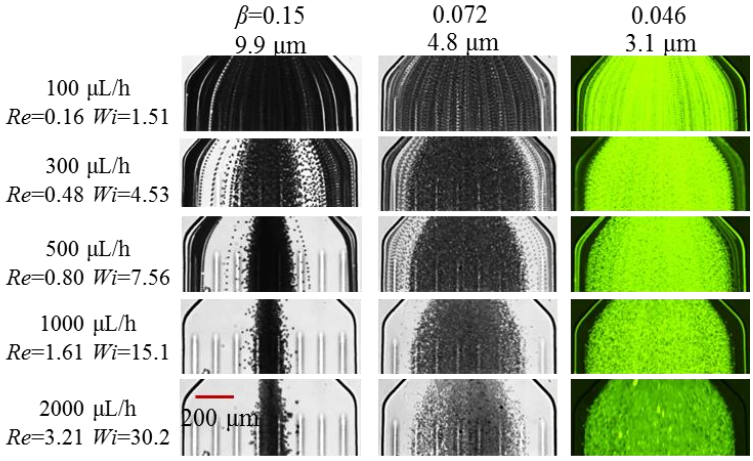

Fig. S1. Focusing patterns of *AR*=0.5 for the 3.1, 4.8, and 9.9 μm particles in the 1000 ppm PEO solution at different flow rate.

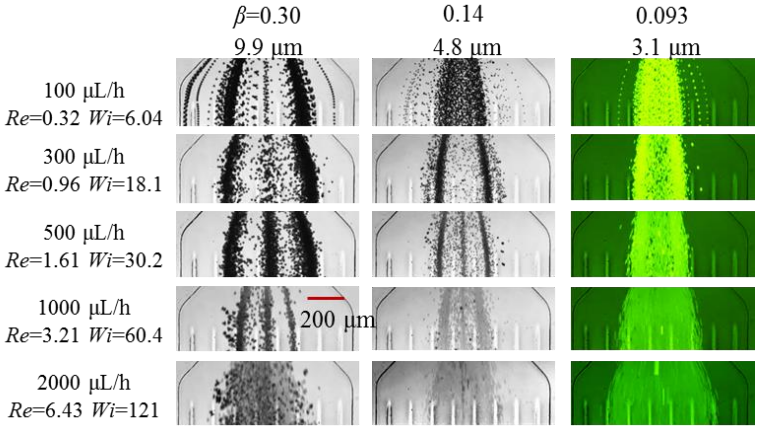

Fig. S2. Focusing patterns of *AR*=2 for the 3.1, 4.8, and 9.9 μm particles in the 1000 ppm PEO solution at different flow rate.

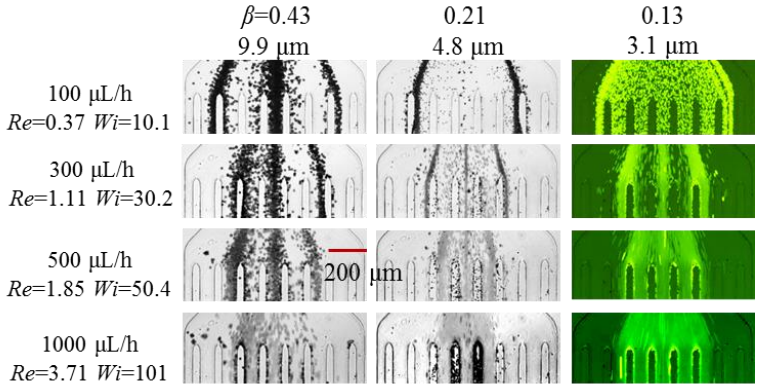

Fig. S3. Focusing patterns of *AR*=3.3 for the 3.1, 4.8, and 9.9 μm particles in the 1000 ppm PEO solution at different flow rate.

Reference

Graessley WW (1980) Polymer chain dimensions and the dependence of viscoelastic properties on concentration, molecular weight and solvent power. Polymer 21(3):258-62

Rodd LE, Scott TP, Boger DV, Cooper-White JJ, McKinley GH (2005) The inertio-elastic planar entry flow of low-viscosity elastic fluids in micro-fabricated geometries. Journal of Non-Newtonian Fluid Mechanics 129(1):1-22

Rubinstein M and Colby RH (2003) Polymer Physics, Oxford University Press Inc

Tirtaatmadja V, McKinley GH, Cooper-White JJ (2006) Drop formation and breakup of low viscosity elastic fluids: Effects of molecular weight and concentration. Physics of Fluids (1994-present) 18(4):043101

Appendix C

SUPPLEMENTARY MATERIAL FOR CONTINUOUS SHETH-FREE SEPARATION OF PARTICLES BY SHAPE IN VISCOELASTIC FLUIDS

1. Determination of the fluid properties in Table 1 in the main text

The zero-shear viscosities, η, of 500 ppm and 1000 ppm PEO solutions were obtained from the experimental measurements of Rodd et al.[1] That of 2000 ppm PEO was calculated using the viscosity blending equation,[2] with the reported experimental values of 1000 ppm and 3000 ppm.[1] The overlap concentration, c^*, of PEO solutions was calculated from the expression of Graessley,[3] $c^* = 0.77/[\eta] = 858$ ppm, where $[\eta] = 0.072M_w^{0.65} = 897$ mL/g is the intrinsic viscosity given by the Mark-Houwink relation with $M_w = 2\times10^6$ Da being the molecular weight of PEO polymser.[1] The Zimm relaxation time of PEO solutions was calculated from Zimm theory[4]

$$\lambda_{Zimm} = F\frac{[\eta]M_w\eta_s}{N_A k_B T} \quad \text{(S1)}$$

where $F = \sum_{i=1}^{\infty} i^{-3\nu} = 0.463$ was estimated from Remann Zeta function using a solvent quality exponent, $\nu = 0.55$,[1] $\eta_s = 1$ mPa·s is the solvent viscosity, N_A is the Avogadro constant, k_B is the Boltzmann constant, and $T = 293.15$ K is the fluid temperature. The effective relaxation times of PEO solutions were then estimated according to the following forumla[5]

$$\lambda_e = 18\lambda_{Zimm}(c/c^*)^{0.65} \quad \text{(S2)}$$

2. Control experiment of shape-based particle separation in water

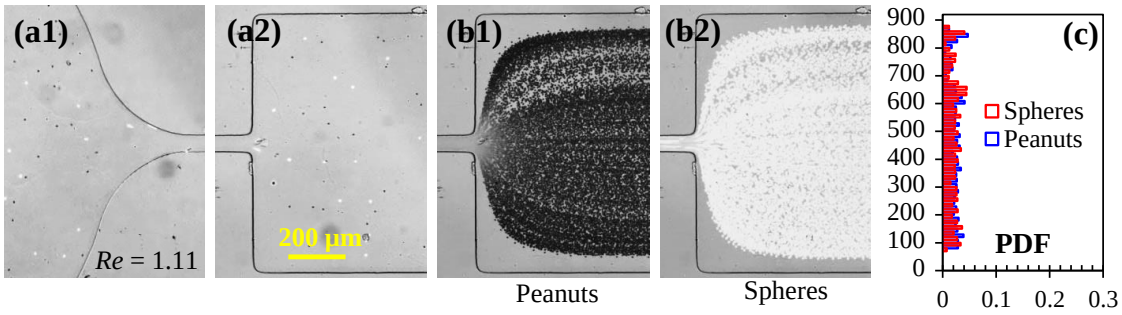

FIG. S1. Demonstration of shape-based separation of fluorescent spherical (bright) and plain peanut-shaped (dark) particles in water through a 25 μm-deep microchannel at a flow rate of 150 μl/h: (a1) and (a2) snapshot images at the channel inlet and outlet, respectively; (b1) and (b2) superimposed images of peanut and spherical particles, respectively, at the channel outlet; (c) the plot of particle PDF at the channel outlet. The flow direction is from left to right.

3. Derivations of Eq. (1) and Eq. (2) in the main text

Assuming an Oldroyd-B model for the constitutive equation, the elastic lift force, $\mathbf{F}_{eL}$, experienced by a particle in a viscoelastic fluid is given by,[6,7]

$$\mathbf{F}_{eL} \sim a^3 \nabla \mathbf{N}_1 \sim a^3 Wi \dot{\gamma}^2 \tag{S1}$$

where $\mathbf{N}_1$ is the first normal stress difference and $\dot{\gamma} = 2V/w$ is the fluid shear rate with V being the average fluid velocity. Substituting the definition of Wi in the main text into Eq. (S1) yields

$$\mathbf{F}_{eL} \sim a^3 \lambda_e \dot{\gamma}^3 = a^3 \lambda_e \left(\frac{2V}{w}\right)^3 = a^3 \lambda_e \left(\frac{2Q}{w^2 h}\right)^3 = 8 \left(\frac{a}{w}\right)^3 \lambda_e \frac{Q^3}{(wh)^3} \sim \lambda_e (a/w)^3 Q^3 \tag{S2}$$

The total inertial lift force, $\mathbf{F}_{iL}$, scales as[8]

$$\mathbf{F}_{iL} \sim \rho V^2 a^4 / w^2 = \rho \left(\frac{Q}{wh}\right)^2 a^4 / w^2 = \rho \frac{Q^2}{h^2} (a/w)^4 \sim \rho (a/w)^4 Q^2 \tag{S3}$$

4. Flow rate effects on shape-based particle separation in different PEO solutions

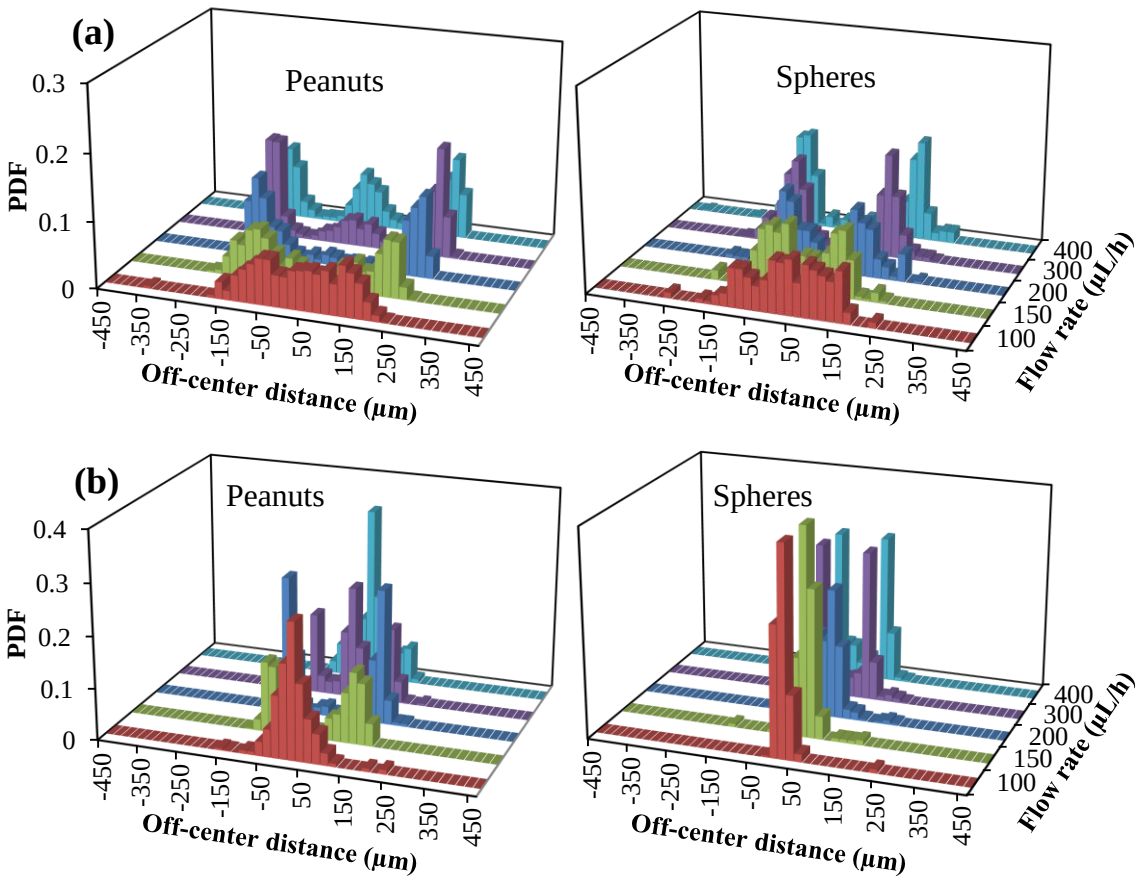

FIG. S2. PDF plots for the flow effects on shape-based particle separation in 500 ppm (a) and 2000 ppm (b) PEO solutions through a 50 μm wide, 25 μm deep straight rectangular microchannel.

5. Flow rate effects on shape-based particle separation in microchannels of different *AR*

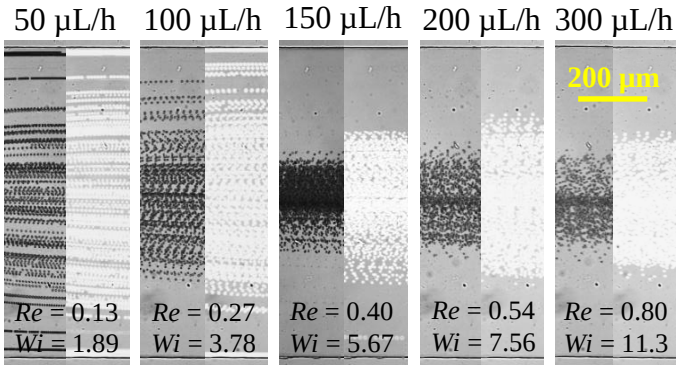

FIG. S3. Cropped superimposed particle images at the channel outlet for the flow rate effect on shape-based separation of plain peanut (dark) and fluorescent spherical (bright)

particles in 1000 ppm PEO solution through a 50 μm wide and 40 μm deep (i.e., *AR* = 1.25) straight rectangular microchannel. The scale bar represents 200 μm.

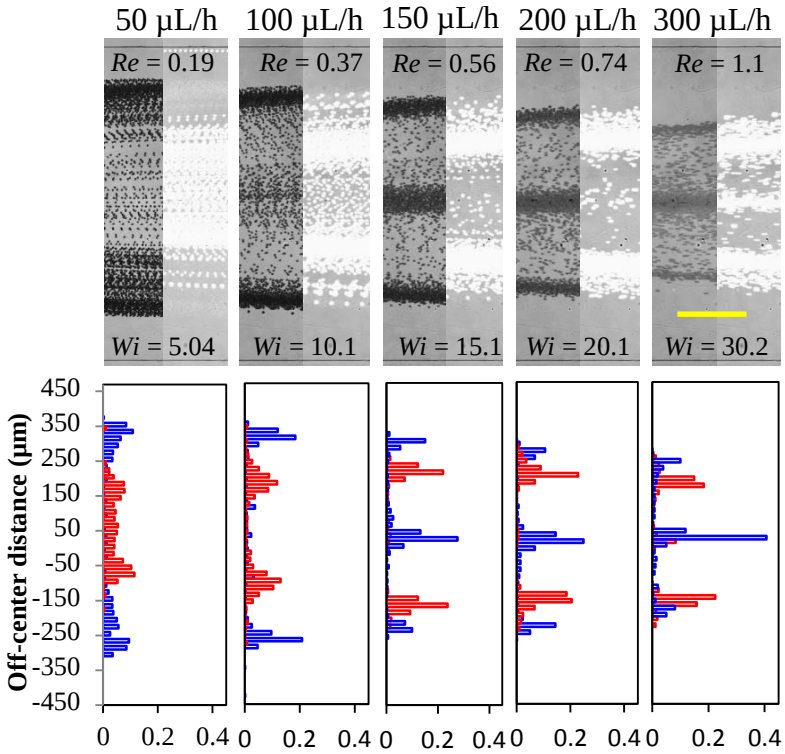

FIG. S4. Flow rate effect (in terms of the Reynolds number, *Re*, and Weissenberg number, *Wi*) on shape-based separation of plain peanut (dark) and fluorescent spherical (bright) particles in 1000 ppm PEO solution through a 50 μm wide and 15 μm deep (i.e., *AR* = 3.3) straight rectangular microchannel: (top row) cropped superimposed particle images at the channel outlet; (bottom row) plots of particle PDF at the channel outlet. The scale bar represents 200 μm.

References

[1] L. E. Rodd, T. P. Scott, D. V. Boger, J. J. Cooper-White, and G. H. McKinley, J. Non-Newtonian Fluid Mech. **129**, 1-22 (2005).

[2] R.E. Maples, Petroleum Refinery Process Economics, 1993, Pennwell Books, Tulsa, Okla.

[3] W. W. Graessley, Polymer **21**, 258-262 (1980).

[4] M. Rubinstein, and R. H. Colby, Polymer Physics, Oxford University Press Inc. (2003).

[5] V. Tirtaatmadja, G. H. Mckinley, and J. J. Cooper-White, Phys. Fluid. **19**, 043101 (2006).

[6] A. M. Leshansky, A. Bransky, N. Korin, and U. Dinnar, Phys. Rev. Lett. **98**, 234501 (2007).

[7] S. Y. Yang, J. Y. Kim, S. J. Lee, S. S. Lee, and J. M. Kim, Lab Chip **11**, 266-273 (2011).

[8] E. S. Asmolov, J. Fluid Mech. **381**, 63-87 (1999).